Hung. J. Ind. & Chem. *2012*, Vol. 40(2) pp. 65–119

Table of Contents

MATERIALS FROM CHARACTERIZATION TO INDUSTRIAL APPLICATION – RENEWABLE FEEDSTOCK AND WASTE RECYCLING

A NEW RESEARCH PROJECT AT THE UNIVERSITY OF PANNONIA

The industrial mass production generates an ever growing volume of volume of waste production and discarded goods that have a significant impact on the environment. The costs of disposing these wastes are high. In the same time, the demand of industry for raw materials is increasing rapidly and certain raw materials become more and more expensive as their availability becomes limited. Waste recycling and waste prevention are possible solutions for these problems. The implementation of these approaches requires new chemical processes. Due to the variability of composition of wastes as raw materials, the development of these technologies is a large challenge for chemical engineering, too. The sustainability of our society and the environment, however, depends largely on the success of these R&D activities. The development of greener processes are investment into the future. In order to achieve these goals, the University of Pannonia together with the College of Dunaujváros applied for a TÁMOP-4.2.2.A-11/1/KONV grant called for the funding of implementation of basic research projects with international cooperation in the framework of the Social Renewal Operational Program (TÁMOP) of the New Széchenyi Plan. The goal of the project entitled "Materials from characterization to industrial application – renewable feedstock and waste recycling" was to start an R&D activity in order to establish new tools and procedures that support the integrated development of products and technologies. The guiding principle and concept of the project is the development of green processes and technologies considering simultaneously the interests of industries of strategic importance and the different aspects of sustainable development. The research activities taking place in the project cover different levels of time and space from molecular modeling to design of technological procedures. The control and supervision of these activities require the application of an integrated multilevel approach that manages the whole project effectively.

Further information on the project can be found at the project's website (http://mkweb.uni-pannon.hu/hulladek/) and in the relevant papers of Hungarian Journal of Industry and Chemistry.

HUNGARIAN JOURNAL
OF INDUSTRIAL CHEMISTRY
VESZPRÉM
Vol. 40 (2) pp. 65–67 (2012)

COMPARATIVE STUDY ON ELECTRODIALYSIS SYSTEMS FOR GALACTURONIC ACID RECOVERY

K. BÉLAFI-BAKÓ✉, E. MOLNÁR, Z. CSANÁDI, N. NEMESTÓTHY

University of Pannonia, Research Institute on Bioengineering, Membrane Technology and Energetics,
10 Egyetem Str., 8200 Veszprém, HUNGARY
✉E-mail: bako@almos.uni-pannon.hu

Electrodialysis (ED) is an electromembrane separation process suitable for recovery of organic acids. In this work galacturonic acid (GA) obtained by enzymatic hydrolysis of pectins from various sources was separated by a laboratory scale, two-step ED stack and a scaled-up, complex ED system. The experimental results from the two systems were compared.

Keywords: electrodialysis, pectin, galacturonic acid

Introduction

Galacturonic acid is the monomer of pectin, a polysaccharide [1] often occurred in agro-wastes, like sugar beet pulp, apple pomace, press cakes of fruits... etc. Pectin can be hydrolyzed by enzymes and the process results a galacturonate (Gat) solution. Since it is an acidic (charged) compound, its recovery and separation can be carried out by electrodialysis (ED). Electrodialysis is an electro membrane process, where charged components move in the direction of the oppositely charged electrode under electrical potential difference [2, 3].

ED has already been applied to separate various organic acids like citric acid, lactic acid, acetic acid, propionic adic, gluconic acid, maleic acid [4–8]. In case of pectin hydrolysates ED can be used for recovery and desalination of galacturonate ions (the counter ion is usually Na). A laboratory scale, two step ED stack and a Fumatech FT-ED-4-100-10 scaled-up complex module were applied in our laboratory to recover GA ([9 ,10]. In this work the stacks are compared from the aspects of yield, operation parameters, energy requirement and average current efficiency.

Material and methods

Galacturonic acid (GA) applied in the model solutions was purchased from Sigma-Aldrich, while sodium sulphate from Spectrum (Hungary). Cation- (Fumasep FKB), anion-selective (Fumasep FAB) and bipolar (BP) membranes were purchased from Fumatech.

Hydrolysis of pectin solutions from sugar beet pulp and citrus was carried out by pectinase enzymes (Pectinex 100L enzyme preparation) in a shaking incubator. The process was followed by acid titration (0.5 M NaOH).

The laboratory scale ED set up consisted of two stacks (one conventional and the other contains bipolar membrane) was constructed in our workshop. The first stack was an symmetric ED cell (described in [9]), with 0.0225 m^2 membrane surface area. Here the galacturonate ions from the hydrolysate moved toward the anode and passed through the anion selective membrane, while sodium ions are transported in the other way. Thus a concentrate stream containing mainly Na-galacturonate was formed.

Then its desalination was carried out in the second ED cell, where 2 cation selective and a bipolar membrane were built in *(Figure 1)* altogether with 0.0135 m^2 membrane surface area. Separation of sodium and galacturonate ions was possible: galacturonate anions remained in the feed solution forming an acid solution, while Na ions passed through the cation selective membrane into the alkali solution forming NaOH.

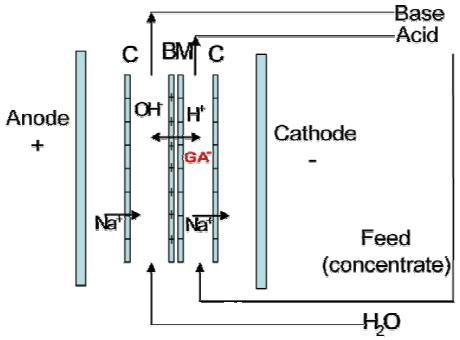

Figure 1: Set-up of the second laboratory scale ED module

The scaled-up complex module containing cation, anion selective and bipolar membranes was described in [10], its membrane surface area was 0.31 m^2.

Both ED stacks were operated by recirculation, using Na_2SO_4 solution (electrode solution). The experiments were followed by measuring the concentration of GA (DNS test [11]) in various streams, conductivity, pH, electric current and voltage, the data were collected by a data acquisition device (National Instruments USB-6008/6009) and recorded by the program LabVIEW.

The important stack and operation parameters for the laboratory scale stacks and the scaled-up complex ED module were summarized in *Tables 1* and *2*, respectively.

Table 1: Parameters of the two-step ED system for galacturonic acid recovery and desalination

Features of the modules	Conventional asymmetric ED	Combined with BP membrane
Membranes	3 cation selective, 2 anion selective	2 cation selective, 1 bipolar
Membrane surface area	0.0225 m^2	0.0135 m^2
Volumes of solutions	feed (diluate): 100 ml, concentrate: 150 ml	feed (acid): 100 ml, alkali: 150 ml
Recirculation rate	32 ml/min	32 ml/min
Electrode solution	200 ml 0.5 mol/l Na_2SO_4	200 ml 0.5 mol/l Na_2SO_4
Recirculation rate	60 ml/min	60 ml/min
Applied voltage	5 V	5 V
Processes	galacturonate anions and Na cations pass through the membranes to accumulate in the concentrate	galacturonate anions remain, BP provides H^+, acid formation Na cations pass through the membranes, form alkali solution
Final results	concentrate rich in Na-galacturonate	formation of galacturonic acid and NaOH solutions

Table 2: Parameters of the scaled-up complex ED system

Features of the module	Scaled-up complex module
Membranes	10 anion selective, 11 cation selective, 10 bipolar
Membrane surface area	0.31 m^2
Volumes of solutions	feed (diluate): 400 ml, acid: 400 ml, alkali: 450 ml
Recirculation rate	380 ml/min
Electrode solution	500 ml 0.1 mol/l Na_2SO_4
Recirculation rate	500 ml/min
Applied voltage	36 V
Processes	both galacturonic anions and Na cations pass through the membrane, formation of acid and alkali solutions
Final results	recovery and desalination of galacturonic acid in one step

Results

Pectin hydrolysates from sugar beet pulp and citrus were studied by using the two ED systems. The experimental results are compared in *Table 3*.

From the table it can be seen, that higher initial concentration feed was applied in case of the two-step laboratory module, since in the second step we had to use the result of the first step: the Na-galacturonate solution (recovered from the hydrolysate). It was desalinated in the BP module. In the scaled-up complex system the separation process (recovery and desalination) was achieved in one single step. Though the energy consumptions were much higher in the scaled-up system and the current efficiencies were lower (than in the laboratory scale stack), but larger amount of product solutions (pure galacturonic acid) were manufactured. If the product acid obtained were related to the energy consumption, we found that – in case of ED separation of sugar beet pectin hydrolysate – 1 Wh energy resulted in 0.09 g and 0.13 g GA production by the two-step, laboratory and the scaled-up, complex system, respectively. The scaled-up system worked with higher effectiveness, moreover it should be taken into account that its operation can be further optimised, and the energy consumption might be reduced even more.

Table 3: Comparison of the two ED systems

Hydrolysate		Two-step laboratory ED system		Scaled-up complex ED system
		asymmetric ED	BP module	
from sugar beet pulp pectin	feed volume feed conc. yield current eff. energy final result	100 ml 36.5g/l 63% 56% 9.2 Wh 150 ml 15.4 g/l Na-Gat solution	100 ml 15.4 g/l desalination – 4.6 Wh 100 ml 12.1 g/l desalinated GA solution	400 ml 15 g/l 65% 41% 31 Wh 400 ml 9.8 g/l desalinated GA solution
from citrus pectin	feed volume feed conc. yield current eff. energy final results	100 ml 48.9 g/l 78% 63% 8.9 Wh 150 ml 25.4 g/l Na-Gat solution	no data	400 ml 39 g/l 86% 54% 39 Wh 400 ml 33.5 g/l desalinated GA solution

The yield, current effectiveness values are better for citrus pectin hydrolysate than for sugar beet pulp pectin hydrolysate, which may be explained by the higher purity of the citrus pectin preparation.

As a summary, we concluded that electrodialysis is a suitable method for recovery, desalination and purification of galacturonic acid from hydrolysates of various pectins. The complex module was able to separate the product in one step and it seems that the scaled-up system worked more efficiently: higher yield was achieved by less energy consumption. Therefore the complex ED system is suggested to apply for further experiments, aiming to study the possibilities of industrial applications.

Acknowledgement

This work was partly supported by the TÁMOP-4.2.1/B-09/1/KONV-201-0003 and TÁMOP-4.2.2/B-10/1-2010-0025.

REFERENCES

1. Z. I., KERTÉSZ: The pectic substances, Interscience Publishers, New York (1951)
2. H. STRATHMANN: Ion-exchange membrane separation processes, Elsevier, Amsterdam (2004)
3. S. BESZDES, ZS. LÁSZLÓ, G. SZABÓ, C. HODÚR: Enhancing of biodegradability of sewage sludge by microwave irradiation, Hungarian Journal Industrial Chemistry, 36 (2008), pp. 11–16
4. S. NOVALIC, J. OKWOR, K. D. KULBE: The characteristics of citric acid separation using electrodialysis with bipolar membranes, Desalination, 105 (1996), pp. 277–283
5. M. CYTKO, K. ISHI, K. KAWAI: Continuous glucose fermentation for lactic acid production: recovery of acid by electrodialysis, Chemie Ingenieur Technik, 59 (1987), pp. 952–954
6. N. YOSHIYUKI, I. MASAYOSHI, H. MOTOYOSHI: Acetic acid production by an electrodialysis fermentation method with a computerized control system. Applied Environmental Microbiology, 54 (1988), pp. 137–142
7. S. NOVALIC, T. KONGBANGKERD, K. D. KULBE: Recovery of organic acids with high molecular weight using a combined electrodialytic process, Journal of Membrane Science, 166 (2000), pp. 99–104
8. K. BÉLAFI-BAKÓ, N. NEMESTÓTHY, L. GUBICZA: Study on application of membrane techniques in bioconversion of fumaric acid to L-malic acid, Desalination, 162 (2004), pp. 301–306
9. E. MOLNÁR, M. ESZTERLE, K. KISS, N. NEMESTÓTHY, J. FEKETE, K. BÉLAFI-BAKÓ: Utilisation of electrodialysis for galacturonic acid recovery, Desalination, 241 (2009), pp. 81–85
10. E. MOLNÁR, N. NEMESTÓTHY, K. BÉLAFI-BAKÓ: Utilisation of bipolar electrodialysis for recovery of galacturonic acid, Desalination, 250 (2010), pp. 1128–1131
11. G. L. MILLER: Use of dinitro-salicylic acid reagent for determination of reducing sugar, Analytical Chemistry, 31 (1959), pp. 426–428

HUNGARIAN JOURNAL
OF INDUSTRIAL CHEMISTRY
VESZPRÉM
Vol. 40 (2) pp. 69–75 (2012)

EFFECT OF A NEW TYPE OF COUPLING AGENT ON THE MECHANICAL PROPERTIES OF VARIOUS MULTI-WALLED CARBON NANOTUBE/RUBBER COMPOSITES

CS. VARGA[1]✉, B. TÓTH[1], P. GERGÓ[1], L. BARTHA[1]

[1]University of Pannonia, Institutional Department of MOL Hydrocarbon and Coal Processing,
10 Egyetem Str., 8200 Veszprém, HUNGARY
✉E-mail: vcsilla@almos.uni-pannon.hu

In our experimental work application of carbon nanotubes in rubbers have been investigated. The effects of the type of the rubber matrix, the concentration of the carbon nanotubes and the effects of a coupling agent on the mechanical properties of the composites have been studied. The strength of the rubber matrix had great influence on the strengthening behaviour of the carbon nanotubes. By application of surface treated carbon nanotubes the strength of the composites made from a rubber matrix having the tensile strength under 10 MPa could be improved by 35%. However, the composites from the rubber with higher tensile strength contained treated carbon nanotubes afforded balanced performance against fatigue stresses probably due to the effect of the coupling agent and the homogenous distribution of the carbon nanotubes.

Introduction

Rubbers reinforced with carbon black (CB) are used for numerous industrial applications, such as vibration-resistant structures, electromagnetic interface (EMI) shielding materials, antistatic devices, etc. [1–4]. CB improves the mechanical properties (modulus and strength) of the rubber due to the interactions among the fillers and the fillers and the other components of the rubber. The CB particles were proven to form aggregates because of the strong bonding effects to each other. A part of the rubber is encapsulated in those aggregates because of the branched structures of the latter one and is shielded from macroscopic deformations [1]. Small domain size is required for effective reinforcement. On the one hand only branched structures small enough (< 50 nm) can be trapped and thereby achieved a strongly bonded system, and on the other hand only the adequately small domains have high surface activity [1, 2].

In the last two decades researches focused on to substitute CB with another fillers (eg. caolin, sepiolite, SiO_2, zinc-disorbate, titania) also having reinforcing effects [4–6] and also on to reduce the particle size of the CB to improve their dispersion in the rubber matrix [2]. In the former step modification of the surface of the fillers had to be also solved because they are incompatible with the most organic matrices, therefore, coupling agents were being used [5, 7]. The fillers for substitution of CB like SiO_2 have been spread in the recent years especially due to the higher demand for non-black applications [7–11].

Several solutions have been developed in the CB/rubber research area: as two step grinding technology, application of dispersants or coupling agents, pre-treatment of the carbon surface or chemical modification of the elastomer chains, moreover distribution of the CB in a latex solution instead of solid mixing [2]. Not much significant improvements were achieved by the first three solutions. In case of the latter one the modification of the CB surface represented the largest difficulty in order to disperse them homogeneously in the water solution of latex [4, 12].

Application of CB has been still significant because besides it can increase the strength of the vulcanized rubber; it also has a positive effect on the optical and electrical properties, and reduces production cost [3]. Application of carbon nanotubes (CNT) may represent a breakthrough in rubber matrices either but only small quantities have been introduced because of their relatively high price. Furthermore, by dispersion of the CNT arisen the same problems like the CB due to the high surface charge [13, 14].

A lot of papers were published about CNT/epoxy and CNT/thermoplastic composites but only a very few about CNT/elastomers [4, 8, 15–18]. The most exciting challenge in the area of CNT containing composites was to solve the proportional dispersion of the CNT because absence of a well-homogenized morphology the distinguished mechanical improvements of the reinforcement can not be achieved in elastomers either. E.g. Das and co-workers [19] used untreated and modified multi-walled carbon nanotubes (MWCNT) in a blend of styrene-butadiene rubber (SBR) and butadiene rubber (BR) with 50/50 ratio. Hydroxyl-groups were enacted to the surface of the modified MWCNT (Nanocyl®-3153), and bis(triethoxy-silylpropyl)tetrasulfone was applied as the coupling agent for bonding to the rubber. Composites were manufactured by a two-roller mill and a stabilized non-ionic surfactant/ethanol solution was

used for MWCNT-treating. The coupling agent was applied in 2.5% related to the mass of the rubber. Strength of composites containing 5% MWCNT could be enhanced from 1MPa to 4.5 MPa. The new process with the ethanol solution was more effective then other traditional methods in the given concentration range. Similar properties were obtained by MWCNTs having hydroxyl-groups. Application of a silane type coupling agent did not significantly affect the mechanical properties.

Our research has been directed to the application of MWCNT in rubbers. The MWCNT has the same favourable effect in the point of view of the mechanical properties [20–22] as CB, and moreover by introduction of a proper coupling agent strong interaction can be established between the MWCNTs and the rubber. As MWCNTs have excellent mechanical properties they should have better strengthening effect than CB has. If mechanical properties of rubber composites can be improved to a large extent enough then the cost reduction can become less important.

For the surface treatment of MWCNT an olefin-maleic-anhydride copolymer based coupling agent has been applied [24]. Not only the possible effects of the coupling agent but also effects of the mechanical properties of the initial rubber matrix as raw material have also been investigated in MWCNT/rubber composites.

2. Experimental

2.1. Materials

Multi-walled carbon nanotubes (MWCNT) were produced at 700°C by chemical vapor deposition (CVD) process over Fe-Co bimetallic catalyst at the Institutional Department of Chemical Engineering (Institute of Chemical and Process Engineering, University of Pannonia). Purity of MWCNT was higher than 90 wt%, the diameter was between 10 nm and 20 nm, the average length was above 30 μm. Natural rubber (NR) and styrene-butadiene rubber (SBR) based (R-I and R-II) and nitrile-butadiene rubber (NBR) (ACN content: 45%, Mooney viscosity, 100°C: 60) based blends (R-III) were used as matrix material.

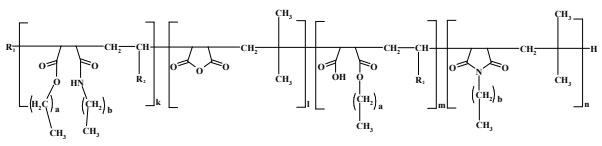

Figure 1: Structure of the ester-amide-imide derivative of the experimental olefin-maleic-anhydride copolymer (R1: alkyl group with length of the olefinic monomer (C16-C18); R2: alkyl group with R1-2 carbon number; a: 3-40, b: 3-32; k: 0,2-2; l: 1-7; m: 1-7 and n: 0,3-2)

The coupling agent was produced at the Institutional Department of MOL Hydrocarbon and Coal Processing (Institute of Chemical and Process Engineering, University of Pannonia) that was an ester-amide derivative of an experimental olefin-maleic-anhydride copolymer *(Figure 1)*.

2.2. Preparation of composites

Compounds were prepared by a milling process. A two-roller mill was applied also for mixing the carbon nanotubes into the basic mixture of rubber. Sheets of the mixtures were compression moulded at 180°C for 5 minutes vulcanization time. Dog-bone samples for mechanical testing were cut from the sheets. Compositions of the samples were given in *Table 1*.

Table 1: Composition of the different MWCNT/rubber composites

sample	rubber matrix type	MWCNT content, wt%	coupling agent, wt%
C-1	R-I	0	-
C-2	R-I	1.0	-
C-3	R-I	1.0	0.2
C-4	R-II	0	-
C-5	R-II	1.0	-
C-6	R-II	1.0	0.2
C-7	R-III	0	-
C-8	R-III	1.0	-
C-9	R-III	1.0	0.2
C-10	R-III	1.5	-
C-11	R-III	2.4	-
C-12	R-III	2.4	0.5

Effects of the coupling agent were also studied by application with an experimental treating method developed for surface treating of MWCNTs for PP [24]. Surface of MWCNT was covered by the coupling agent from the hydrocarbon solution of the additive with stirring the mixture for 1 hour at 60°C then the solvent was distilled out. Treated MWCNTs were then dried at 110°C for 2 hours and were mixed into the basic mixture of rubber by a two-roller mill.

R-I and R-II matrices were NR and SBR based blends with lower and medium mechanical strength, R-III matrix was an NBR based one with high mechanical strength. Thus effects of the type of the rubber were also studied on the properties of the composites. MWCNTs were applied in untreated and in treated form in order to investigate the influence of the coupling agent either.

2.3. Measurement of tensile properties

To determine the tensile and fatigue tensile properties (mainly stress, modulus and extension) (MSZ EN ISO 527-1-4:1999) an INSTRON 3345 universal tensile

testing machine was used. The temperature in the laboratory was 23°C and the relative humidity was 50% during the mechanical tests which were carried out at 90 mm/min crosshead-speed both in case of tensile and fatigue tensile tests.

Structural information about the developed coupling agent was obtained by infrared technique with a TENSOR 27 type FTIR[1], illumination: SiC Globar light, detector: RT-DLaTGS type) in the 400-4000 cm^{-1} wavenumber range.

Scanning Electron Microscopy (SEM) was used to study the structure of fractured faces of the specimens and to follow the possible interaction between the reinforcements and the matrices. The applied apparatus was a Phillips XL30 ESEM instrument.

3. Results and discussion

Discussion of the results was divided into three parts. On the first hand effects of the type of the rubber matrix were detailed then on the second hand effects of the MWCNT concentration and finally the effects of the coupling agent were demonstrated.

3.1. Effect of the change in the rubber matrix on the tensile properties

In the present work effects of multi-walled carbon nanotubes (MWCNT) in three rubber matrices (signed as R-I, R-II, R-III) with different tensile strengths were investigated. Different effects were measured for the rubber matrices *(Figure 2)*. Introduction of MWCNTs into the rubber either in treated or in untreated form resulted in both increase and in decrease of the tensile strengths.

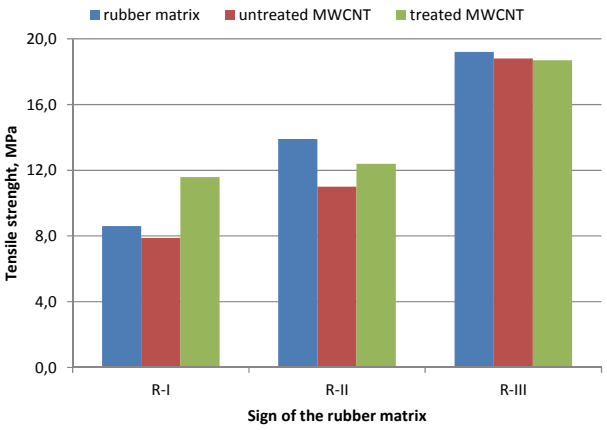

Figure 2: Effects of type of the rubber matrix on tensile properties (1wt% MWCNT-content)

Different effects were measured for the samples where treated MWCNTs were incorporated. Tensile strength enhanced from 8.6 MPa to 11.6 MPa meaning a 35% increase for the R-I matrix. Meanwhile in the case of R-II signed rubber the tensile strength reduced by 26% in the presence of untreated MWCNT. Application of the coupling agent improved the tensile strength by 12% but tensile strength of the original matrix could not be achieved. Tensile strengths of the MWCNT containing composites did not differ to that of the R-III matrix having the highest tensile strength (19.2 MPa).

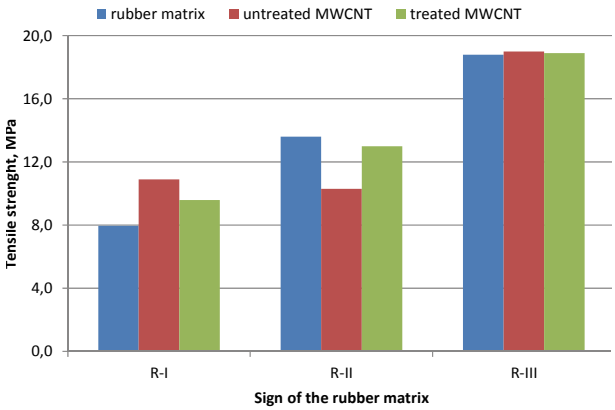

Figure 3: Effects of type of the rubber matrix on fatigue tensile properties (1 wt% MWCNT, fatigue conditions: 100 cycles and 10 N)

Resistance of the samples against fatigue tensile stresses of 100 cycles and 10 N as loading force were also studied *(Figure 3)*. Comparing the results of the fatigue tensile tests to those of the static tensile tests two important outcomes could be stated. First of all MWCNTs in the rubber blends could either improve or deteriorate the mechanical properties depending on the type of the rubber matrices. On the second hand composites made from basic mixture of R-II showed different behaviour than the others. Fatigue tensile strength was found to have been deteriorated by 6.5% if the MWCNT was incorporated in untreated form. The opposite behaviour was experienced by MWCNTs treated by the coupling agent since a 5% increase was measured. Standard deviation (SD) was calculated to be 0.8 MPa for unteated and 1.0 MPa for surface treated MWCNT containing samples.

Elongation at break was also represented for both types of tensile tests *(Figures 4, 5)*.

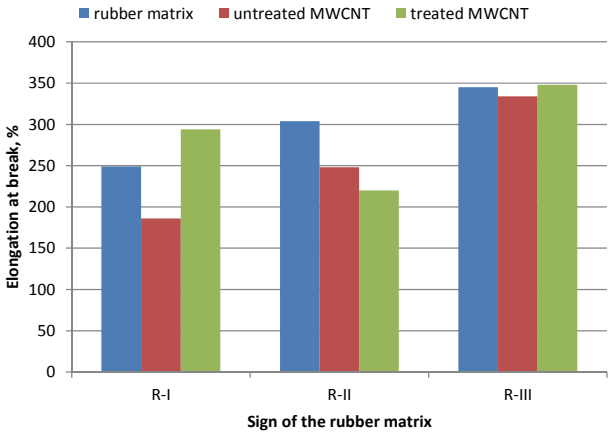

Figure 4: Effects of type of the rubber matrix on elongation at break (1 wt% MWCNT content)

Considerations for the elongation at break were established similar to the tensile strength. Type of the rubber was determinative in the evolution of the elongation at break *(Fig. 4)* either. Reinforcing rubber R-I with MWCNTs the value of 250% of elongation at break significantly decreased due to the pristine MWCNTs. Changing the reinforcement to surface treated MWCNTs an 18% improvement could be measured as the property increased to 290%. MWCNTs even in coupling agent treated form deteriorated the elongation at break of R-II rubber.

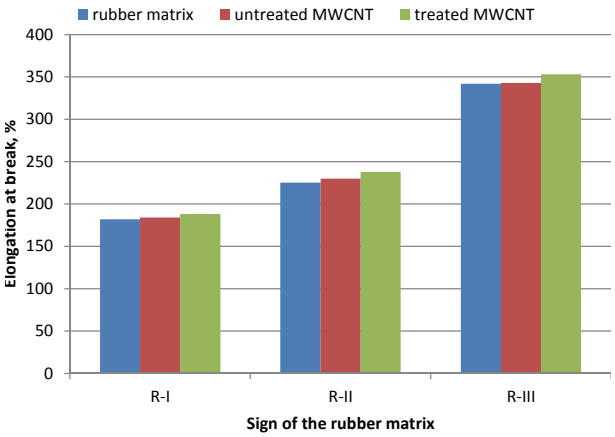

Figure 5: Effects of type of the rubber matrix on elongation at break for fatigue tensile tests (fatigue conditions: 100 cycles and 10 N, 1 wt% MWCNT)

Elongation at break did not change if the matrix with the highest elongation was reinforced with MWCNTS either in untreated or in surface treated form.

Regarding to the results for elongation at break after the fatigue tensile tests a more balanced picture could be drawn. Approximately a 20% decrease was measured for R-I and R-II matrices in the elongation at breaks for fatigue tensile testing compared to static tensile testing. But MWCNT containing composites had the same values for elongation at break both for R-I and for R-II based samples even for fatigue tensile tests. There were not any significant effects of the coupling agent on the elongation at break of all the rubber matrices.

3.2. Effect of carbon nanotube concentration

In that chapter changes in tensile strength, tensile modulus and elongation at break of R-III based composites was discussed in function of the concentration of the MWCNT.

Lower tensile strength was measured for R-III matrix after fatigue tensile tests *(Figure 6)*. Regarding to the static tensile strength approximately 1.5 wt% MWCNT was required for a slight increase.

The fatigue tensile results were represented for the same fatigue load (10 N) with two different cycles: 100 and 1500 cycles *(Fig. 6)*. Resistance of the rubber (R-III) deteriorated with the duration of the fatigue test. The same trends were observed for carbon nanotube containing samples either. 2.4 wt% MWCNT was needed to exceed the tensile strength of R-III after long time fatigue stresses. With lower concentration of MWCNTs in the rubber there was no difference among the property at the same fatigue conditions.

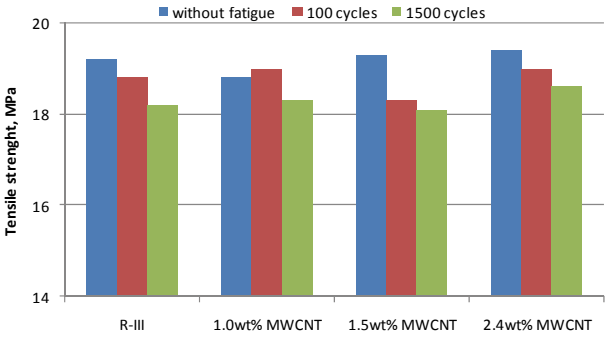

Figure 6: Effects of carbon nanotube concentration on the fatigue tensile strength (fatigue load: 10 N for both 100 cycles and 1500 cycles)

Figure 7 represented the effects of filler concentration on the tensile modulus. On the first hand, values of modulus by the static tensile test increased with the MWCNT content. The modulus of the samples containing 1 wt% MWCNT have been enhanced by 13% related to the reference. The same extent of improvement was measured for the other two MWCNT/rubber composites.

Fig. 7 showed the results for fatigue tensile test either. Depending on the duration of the fatigue tests positive changes were getting lower with increasing MWCNT contents. In that case moduli for the fatigue conditions were compared to the results of the simple tensile test. All the reinforced samples performed higher tensile modulus than that of the rubber matrix, so toughness of the composites enhanced by incorporation of MWCNTs. The modulus of the sample with 2.4 wt% MWCNT depended the less on the duration of fatigue stresses. That phenomenon could be related to orientation of the MWCNTs into the direction of the periodic stresses based on previous experiments with carbon fibres.

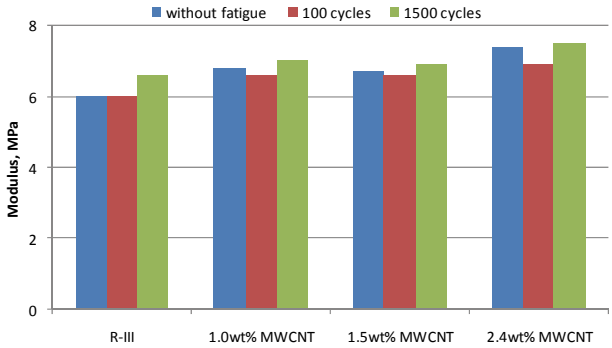

Figure 7: Effects of carbon nanotube concentration on fatigue tensile modulus (fatigue load 10N)

Figure 8 reperesented changes in the elongation at break in the function of the MWCNT content. Elasticity of the samples had been expected to decrease with the MWCNT content. Thus, a reduction in elongation at

break was observed above 1 wt% MWCNTs in the rubber. Not a significant change was calculated for 1 wt% MWCNT/rubber samples. Samples containing 2.4 wt% MWCNT had a value of 300% for elongation at break meanwhile the same property was 345% for the basic rubber.

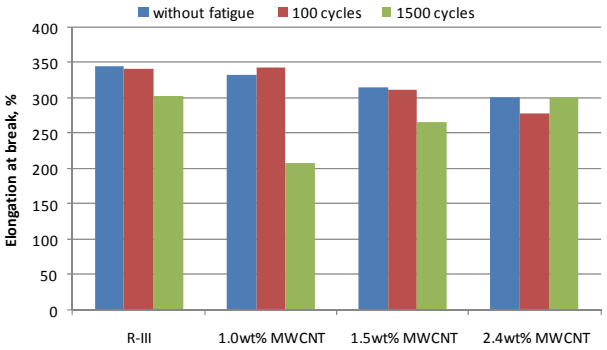

Figure 8: Effects of carbon nanotube concentration on fatigue elongation at break (fatigue load 10 N)

3.3. Effect of surface treatment

In that part of the paper effects of surface treatment were discussed on tensile and fatigue tensile properties. In Figures either results of the unreinforced rubber matrix with composition R-III or results of the composites containing 2.44 wt% MWCNT reinforcement were demonstrated. During the fatigue tensile tests a fatigue force of 10 N was applied with different duration times (100 and 1500 cycles).

Figure 9 represented the effects of untreated and coupling agent treated MWCNTs on tensile strength and fatigue tensile strength of the unfilled rubber. Changes for simple tensile test could be not significant both for untreated and treated MWCNT/rubber samples containing the same concentration of MWCNT. Change was calculated to be below 5%.

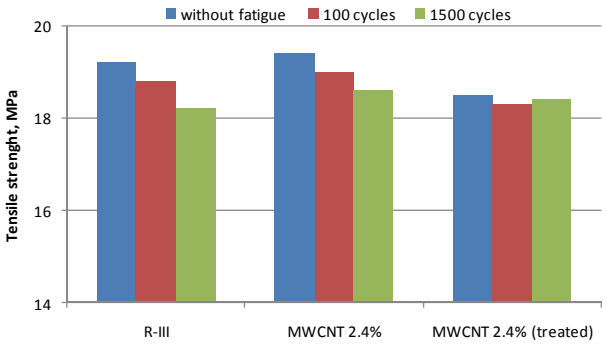

Figure 9: Effects of surface treatment on fatigue tensile properties (fatigue load: 10 N)

The same trend was observed for the fatigue tensile tests. As *Fig. 9* clearly showed, values of fatigue tensile strength slightly decreased for the rubber matrix and the pristine MWCNT/rubber composites with the increasing number of fatigue cycles. However, the composite containing surface treated MWCNTs afforded more balanced performance even for a long period of fatigue stress (1500 cycles) in the given range of concentration and the coupling agent has a higher stabilizing effect in the composite.

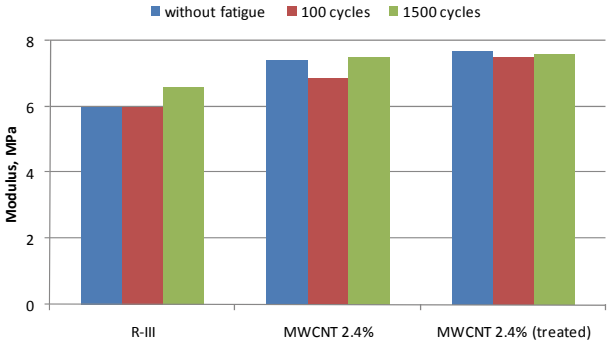

Figure 10: Effects of surface treatment on fatigue tensile properties of the composites (fatigue load: 10 N)

In *Figure 10* the effects of the surface treated MWCNTs were demonstrated on the tensile moduli in function of number of fatigue cycles. Due to application of MWCNTs in the rubber matrix the values of modulus enhanced compared to the rubber since the aforementioned reinforcing material can increase toughness of plastics, elastomers and rubbers.

Resistance against fatigue stresses were also showed in *Fig. 10*. The values of modulus have been increased both for untreated and treated MWCNT containing samples compared to the initial rubber matrix independently from duration of the fatigue stress. Almost the same moduli were determined for both MWCNT/rubber composites at the same level of fatigue conditions. Surface treatment was concluded not to have significant effects on tensile modulus but more balanced behaviour was experienced for treated MWCNT/rubber samples.

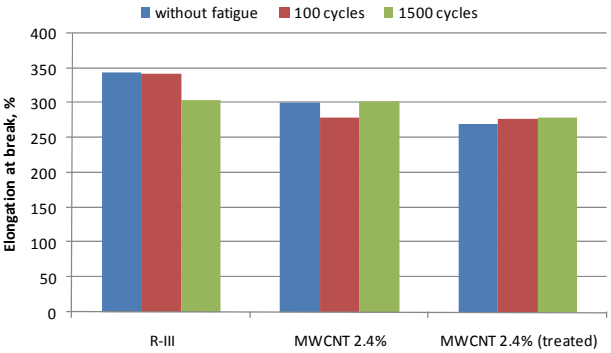

Figure 11: Effects of surface treatment on fatigue tensile properties of the composites (fatigue load: 10 N)

Figure 11 demonstrated the effects of both forms of MWCNTs on the elongation at break for distinct fatigue duration. Values of elongation at break for MWCNT/ rubber composites were measured to be below the value of the rubber matrix. The trends were the same both for simple and for fatigue tensile tests.

Results were observed to be more balanced for coupling agent treated MWCNT reinforced rubber in that point of view too. Although elongation at break for the original rubber matrix was the highest among all the

samples regarding the tensile test but after a longer fatigue tensile test significant (13%) deterioration was obtained and the value of the treated MWCNT/rubber was less sensitive against fatigue stresses.

3.4. SEM

Homogeneity of the samples based on R-I rubber was studied on the SEM graphs of the broken surface of the composites *(Figure 12–14)*.

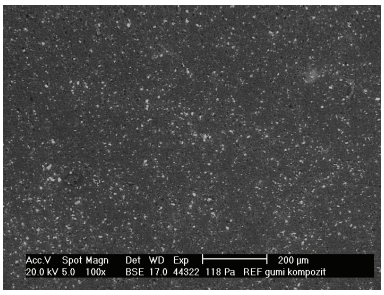

Figure 12: SEM graph of the broken surface of the original rubber matrix

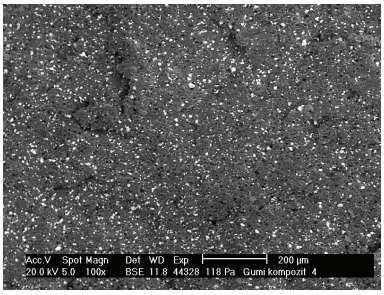

Figure 13: SEM graph of the broken surface of the pristine CNT containing rubber composite

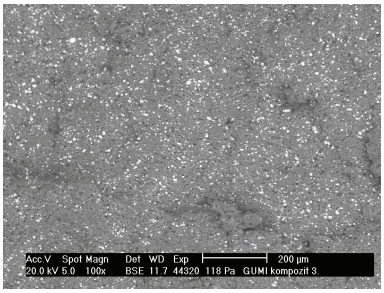

Figure 14: SEM graph of the broken surface of the coupling agent treated CNT containing rubber composite

Components of the rubber formula were clearly remarked (white spots) on SEM graph of all the samples. Difference was observed between the carbon nanotube containing samples. Composites with untreated CNTs showed a less smooth surface after tensile test than samples with surface treated reinforcements. Narrower and more homogeneous particle size distribution was experienced on the surface of coupling agent treated carbon nanotube/rubber samples indicating higher degree of compatibility of the components which could probably result the improvement of the mechanical properties.

Conclusion

Our research has been directed to the application of MWCNT in rubbers in which effects of an olefin-maleic-anhydride based coupling agent was also studied. The results were summarized as follows:

- Application of carbon nanotubes in a rubber matrix could both enhance and deteriorate the mechanical properties of the composites depending on the types and strength of the original rubber mixture.
- Difference in the behaviour in MWCNT containing composites could be experienced during the fatigue tensile test, which could be important especially for rubber products.
- At least 2.4 wt% MWCNT was required to achieve better performance during long time fatigue than the rubber matrix with the highest tensile strength (R-III).

Acknowledgement

We acknowledge the financial support of the work by the Hungarian State and the European Union under the TÁMOP-4.2.2/B-10/1-2010-0025 project. Authors are also grateful to the project of Baross Gábor Program (REG_KD_09_2-2009-0026) for the financial support.

REFERENCES

1. B. OMNES, S. THUILLIER, P. PILVIN, Y. GROHENS, S. GILLET: Compos Part A, 39 (2008), pp. 1141–1149
2. X. HE, Z. PENG, N. YU, J. HAN, C. WU: Compos Sci Technol, 68 (2008), pp. 3027–3032
3. Z. H. LI, J. ZHANG, S. J. CHEN: eXPRESS Polym Lett, 2 (2008), pp. 695–704
4. K. TSUCHIYA, A. SAKAI, T. NAGAOKA, K. UCHIDA, T. FURUKAWA, H. JAJIMA: Compos Sci Technol, 71 (2011), pp. 1098–1104
5. S. PRAVEEN, P. K. CHATTOPADHYAY, P. ALBERT, V. G. DALVI, B. C. CHAKRABORTY, S. CHATTOPADHYAY: Compos, Part A, 40 (2009), pp. 309–316
6. B. C. GUO, F. CHEN, W. W. CHEN, Y. D. LEI, D. M. JIA: eXPRESS Polym Lett, 9 (2010), pp. 529–538
7. B. T. POH: C.C. NG, Eur Polym J, 34 (1998), pp. 975–979
8. A. DAS, R. N. MAHALING, K. W. STÖCKELHUBER, G. HEINRICH: Compos Sci Technol, 71 (2010), pp. 276–281
9. E. PLANES, L. CHAZEU, G. VIGIER, T. STUHLDNEIER: Compos Sci Technol, 70 (2010), pp. 1530–1536
10. S. J. AHMADI, C. G'SELL, Y. HUANG, N. REN, A. MOHADDESPOUR, Compos Sci Technol, 69 (2009), pp. 2566–2572

11. K. G. GATOS, K. KAMEO, J. KARGER-KOCSIS: eXPRESS Polym Lett, 1 (2007), pp. 27–31
12. P. VERGE, S. PEETENBROCK, L. BANNAUD, P. DUBOIS: Compos Sci Technol, 70 (2010), pp. 1453–1459
13. H. H. LE, X. T. HOANG, A. DAS, U. GOHS, K.-W. STOECKELHUBER, R. BOLDT, G. HEINRICH, R. ADHIKARI, H.-J. RADUSCH: Carbon, 50 (2012), pp. 4543–4556
14. S. N. LAWANDY, S. F. HALIM, N. A. DARWISH: eXPRESS Polym Lett, 3 (2009), pp. 152–158
15. J. W. CHUNG, S. J. HAN, S-Y. KWAK: Eur Polim Journal, 45 (2009), pp. 79–87
16. S. POOMPRADUB, Y. IKEDA, Y. KOKUBO, T. SHINO: Eur Polim Journal, 44 (2009), pp. 4157–4164
17. J. CARRETERO-GONZÁLEZ, J. L. VALENTÍN, M. ARROYO, K, SAALWACHTER, M. A. LOPEZ-MANCHADO: Eur Polim Journal, 44 (2009), pp. 3493–3500
18. F. AVALOS, J. C. ORTIZ, R. ZITZUMBO, M. A. LÓPEZ-MANCHADO, R. VERDEJO, M. ARROYO: Eur Polim Journal, 44 (2009), pp. 3108–3115
19. A. DAS, K. W. STÖCKELHUBER, R. JURK, M. SAPHIANNIKOVA, J. FRITZSCHE, H. LORENZ, M. KLÜPPEL, G. HEINRICH: Polymer, 49 (2008), pp. 5276–5283
20. L. BOKOBZA: eXPRESS Polym Lett, 3 (2012), pp. 213–223
21. K. SUBRAMANIAM, A. DAS, G. HEINRICH: Compos Sci Technol, 71 (2011), pp. 1441–1449
22. M. MOTAMEDI, M. ESKANDARI, M YEGANEH: Materials and Design, 34 (2012), pp. 603–608
23. A. SZENTES, CS. VARGA, G. HORVÁTH, L. BARTHA, Z. KÓNYA, H. HASPEL, J. SZÉL, Á. KUKOVECZ: eXPRESS Polym Lett, 52 (2012), pp. 494–502
24. CS. VARGA, N. MISKOLCZI, L. BARTHA, G. LIPÓCZI, L. FALUSSY: Műanyag és Gumi, 45 (2008), pp. 148–152

HUNGARIAN JOURNAL
OF INDUSTRY AND CHEMISTRY
VESZPRÉM
Vol. 40 (2) pp. 77–82 (2012)

APPLICATION OF THE REMOTE EARTH POTENTIAL IN CATHODIC PROTECTION MEASUREMENTS

Z. LUKACS

Indexon Ltd., 8 Veres acs Str., 6725 Szeged, HUNGARY
E-mail: lukacs.zoltan@indexon.hu

The conventional potential measurements and evaluation methods of cathodic protection diagnostics do not give reliable results in some practically important cases: in systems where the whole amount of cathodic protection current cannot be interrupted for any reason or the equalizing currents affect the protection to a significant level or interference with other cathodic protection systems is encountered. The paper discusses a model and its practical application dealing with these difficult cases. The test measurement evaluation results justify the theoretical model. On the basis of the theory a very simple measurement method is proposed for the determination of the coating defects IR-free potentials.

Keywords: cathodic protection, IR-free potential, pipeline corrosion, coating defect

1. Introduction

The cathodic protection is a widely used, robust and reliable method of corrosion protection of underground pipelines, tank bottoms and underwater parts of immersed structures, e.g. ships and drilling platforms. In the past eight decades a lot of experience has been accumulated concerning the applicability and limitations of cathodic protection.

In the most widespread type of cathodic protection, the impressed current systems, the structure to be protected is connected to the negative output of a DC current source („CP station") and the positive output is connected to a so-called earthing anode which serves for the closing of the electrical circuit (see a typical arrangement for a cathodically protected pipeline in *Figure 1*). The output of the DC source is variable and, in modern devices, can be regulated, either for constant potential or for constant current.

If no cathodic protection is applied to a structure corroding in water or soil and no net current is flowing through the structure, then the sum of the anodic (corrosion) and cathodic currents is zero. The ultimate criterion of the effectiveness of cathodic protection is the level of suppression of the anodic current. This can be achieved with the cathodic polarization of the structure. The decrease of the anodic current cannot be measured directly. However, if the applied potential is sufficiently negative (cathodic) then the anodic current (and the corrosion rate) is suppressed, with increasing cathodic polarization theoretically beyond any limit; practically a decrease of 1–2 orders of magnitude can be implemented, which is satisfactory for the practical requirements in most cases.

In conclusion, the negative polarization of the structure results in the suppression of the anodic current (this was the goal) and in the increase of the cathodic current, which is an unavoidable consequence of the potential shift, sometimes with unfavourable side effects.

During the past decades a lot of empirical experience has been accumulated concerning the optimal operation conditions of cathodic protection. It has been assumed for a long time that cathodic protection has the best performance in typical applications in soils if the electrode potential of the structure is more negative than -850 mV, measured against a saturated copper/copper sulphate electrode [1] (its standard potential at 25°C is -320 mV; all potential data will be given against this type of reference electrode unless specified otherwise). The lower limit of the potential varies for different applications but it is typically assumed to be between 1100 and 1300 mV[1].

The electrode potential, as discussed above, is the potential that can be measured with a reference electrode placed to the direct vicinity of the electrode, i.e. which does not include any component from the ohmic potential drop through the electrolyte[2]. This potential, called as IR-free potential, is a central concept in cathodic protection.

[1] At more negative potential the excessive rate of cathodic current may have adverse effects on the structure or on the coating.

[2] There is another source of the ohmic potential drop, namely, the drop in the electric conductor, which can also be significantly high in the case of pipelines, but this source will not be dealt here; in this paper the ohmic drop is understood as the ohmic potential drop through the electrolyte between the anode and the cathode.

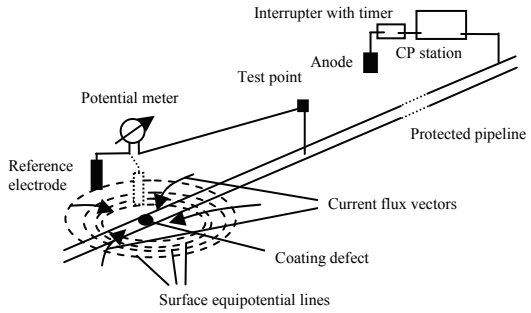

Figure 1: Schematic arrangement of cathodic protection and potential measurement circuitry

The determination of the exact value of the IR-free potential is practically impossible in case of buried structures and with conventional methods. This paper is dealing with the mathematical properties of the electric field of the cathodic protection system and provides a simple method to give a good approximation of the IR-free potential, with significant practical advantages that are facilitated by making use of the remote earth potential. The discussion below is dealing specifically with the case of coated, buried and cathodically protected steel pipelines. However, the situation with tanks bottoms and other buried structures is quite similar. For offshore and underwater structures the theory also applies but the application technology is slightly different – these cases will be dealt with in separate communications.

2. Discussion

2.1. Review of the conventional ways of determination of the IR-free potential

In the first times of application of cathodic protection the cathodic protection was assumed as effective if the polarized potential was more negative to the open-circuit potential.

It was realized very soon that the measured potential value was dependent on the location where the reference electrode was placed (owing to the location-dependent ohmic potential drop) and the need of a criterion of effectiveness was also recognized. The determination of the IR-free potential was carried out by the switching off the current source. This technique is routinely used in the laboratory electrochemical measurements, too.

The determination of the ohmic drop compensated corrosion potential of a cathodically protected structure has an enormous literature. A short but concise general overview on the topic was given by Bushmann and Rizzo [2]. In the standard practice of cathodic protection nowadays the determination of the IR-free potential is carried out by periodically switching the current source off and on. Typically a pattern of 2–4 seconds switched on and 0.5–1 second switched off is implemented (the time values may also vary in a wider range). The potential measurements are carried out after a delay of at least 0.1 second, in order to eliminate the effect of the inductive transients (these appear in case of long pipelines and large currents only). The potentials measured with CP stations turned on and off are generally named as ON potential and OFF potential respectively.

Under field conditions in many cases it is nearly impossible or at least very cumbersome, expensive and time-consuming to switch all the CP stations that are effective in a certain area. If some of the current sources remain switched on while measuring the OFF potential that results in a major bias in assessing the IR-free potential. This bias may be up to a few hundreds of millivolts in extreme cases, and often leads to erroneous conclusions with respect to the level of protection of structures, sometimes with serious consequences. In spite of these obvious deficiencies, in the industrial practice in most cases the measured OFF potentials are identified with the IR-free potentials.

Another source of the uncertainties in assessing the IR-free potential via the OFF potentials is the ohmic potential drop generated by the equalizing currents flowing between the more and less polarized parts of the structure. Stray current sources can also falsify the conventional IR-free potential determinations via the measured OFF potentials.

Nowadays typically GPS-driven, high precision clock operated interrupters are applied in CP measurements, which facilitate an increased measurement precision and reliability. Some manufacturers also provide CP stations with built-in interrupters and remote control options.

2.2. An alternative way of calculation of the IR-free potential from measurement data

In spite of the enormous progress in measurement technique and the apparent inadequacy of the determination of the IR-free potential via the OFF-potential, no much progress has been achieved in the theory and in the evaluation of the measurement data.

Let us assume a cathodic protection system with an anode and a single coating defect at some part of the protected structure. The potential profile as a function of the distance between the coating defect and the anode is shown in *Figure 2*. The potential field of the coating defect is defined as the domain where the potential is more negative than the remote earth potential and the potential gradients are directed towards the coating defect.

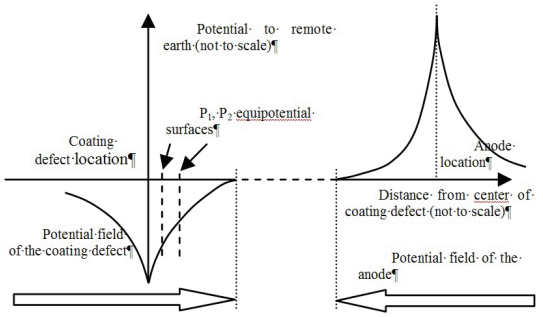

Figure 2: Potential relations in the area of the anode and the coating defect

Let us mark two points in the potential field of the coating defect as P_1 and P_2. These two points determine two equipotential surfaces that surround the coating defect. Also, these equipotential surfaces mark a domain of the space with a definite and constant (i.e. independent from the current flux) electrical resistance. Let R_1 and R_2 be the ohmic resistance between the coating defect and the points P_1 and P_2 respectively.

Further on, let us assume that some perturbation is applied to the CP system, i.e. the current is interrupted (completely or partially – it is indifferent from the point of the model). From Ohm's Law it follows that

$$R_x = \frac{E_x^{OFF} - E_0}{I^{OFF}},\ R_x = \frac{E_x^{ON} - E_x^{OFF}}{I^{ON} - I^{OFF}}, \quad (1a, b)$$

where x=1.2 refers to any of the two surfaces and the *ON* and *OFF* superscripts refer to the potential or current in the respective states. E_0 is the IR-free potential of the coating defect[3].

Expressing R_x and rearranging the equation, the IR-free potential can be expressed as:

$$E_0 = E_x^{OFF} + \left(E_x^{OFF} - E_x^{ON}\right)\frac{I^{OFF}}{I^{ON} - I^{OFF}}. \quad (2)$$

If I_{OFF}=0, i.e. all the current is switched, then *Eq. 2* is simplified to E_0=E^{OFF}, that is, the measured OFF potential is equal to the IR-free potential. However, if I_{OFF}≠0 then the determination of E_O from *Eq. 2* is impossible, because the current values are indeterminable. Let I^{OFF} and I^{ON} be expressed from the rearrangement of *Eq. 1a* (for the determination of I^{ON} the *OFF* superscripts have to be changed to *ON*, but this is allowed because the equation is valid also in the ON state of the system). From Ohm's Law it is obtained that

$$I^{OFF} = \frac{E_1^{OFF} - E_2^{OFF}}{R_{1,2}}, \quad (3a)$$

$$I^{ON} = \frac{E_1^{ON} - E_2^{ON}}{R_{1,2}}, \quad (3b)$$

where $R^{1,2}$ is the resistance between the two distinct equipotential surfaces. Substituting *Eq. 3a* and *Eq. 3b* into *Eq. 2* it follows that

$$E_0 = E_x^{OFF} + \left(E_x^{OFF} - E_x^{ON}\right)\frac{E_1^{OFF} - E_2^{OFF}}{\left(E_1^{ON} - E_2^{ON}\right) - \left(E_1^{OFF} - E_2^{OFF}\right)}, \quad (4)$$

where x=1.2.

[3] Throughout in this paper it is assumed that the polarization resistance is negligible to the ohmic resistance of the soil between the coating defect and the point of the reference electrode. In most practical cases of buried structures in soil this assumption is valid. Effects of the transient decay of the charge/discharge of the electrochemical double layer and other transients related to the inductivity of the pipelines will be dealt with in a separate paper.

By means of *Eq. 4* the IR-free potential is obtained from measurable potential data also in the case if the current, flowing to the coating defect, is interrupted only partially or perturbated in any other way.

Let us introduce the following notation:

$$\rho = \frac{E_1^{OFF} - E_2^{OFF}}{(E_1^{ON} - E_2^{ON}) - (E_1^{OFF} - E_2^{OFF})}, \quad (5)$$

and note that ρ is the quotient of the "not switched" and "switched" currents, flowing to the coating defect, and thus is invariant within the potential field of a certain coating defect. ρ is named foreign current ratio hence because it denotes the ratio of the foreign (i.e. not switched) and switched current.

Using *Eq. 5*, *Eq. 4* can be rewritten as

$$E_0 = E^{OFF} + (E^{OFF} - E^{ON})\rho, \quad (6)$$

where the x subscripts are no more needed because the equation is valid for potentials measured at any point in the potential field of the coating defect.

By means of this calculation the value of the IR-free potential, which is not directly measurable if any current is flowing in the OFF state, can be determined by means of measurable potential data.

An equation formally analogous to *Eq. 6* had earlier been reported by Baeckmann and Schwenk [3], but the evaluation presented in their work is started from a quite different approach and also their conclusions are very different. The practical implementation of their measurement method is published in [4].

An important consequence of *Eq. 6* is that E_0 and ρ are linearly dependent if E^{OFF} and E^{ON} are substituted with the constant values of the remote earth potentials:

$$E_0 = E_\infty^{OFF} + (E_\infty^{OFF} - E_\infty^{ON})\rho, \quad (7)$$

Taking into consideration that for the determination of ρ it is not necessary to connect to the structure with a measurement cable because it is calculated from the differences of potentials at two different places in the ON and OFF state (cf. *Eq. 5* and *Fig. 1*), *Eq. 7* provides a simple and fast method to determine the IR-free potential of coating defects where there is no test post in the vicinity. This method is a powerful alternative of the widely used CIPS (Close Interval Potential Survey) or intensive surveys [4]: the coating defect IR-free potentials are practically calculated from potential gradient data and the remote earth potentials recorded with a static data logger. Further, by fitting the data received on different coating defects in a cathodic protection system using *Eq. 7*, it is possible to provide data quality control facility: those data which are not fitting on the linear relationship and deviate over a threshold value are to be discarded. *This is a unique feature in the practice of cathodic protection.*

2.3. A practically important case: more coating defects in a system

The calculation in Section 2.2 is strictly valid if the cathodic protection system includes one anode and one coating defect. Obviously, real systems are more complicated. Further difficulty is that in real systems the potential of the coating defects is varying; small coating defects with less ohmic potential drop[4] can be polarized to a more negative potential than the larger coating defects. This potential difference between the coating defects generates equalizing currents superimposed on the cathodic protection current and, consequently, on changing of the shape of the cathodic protection current vector space, the shape of the equipotential surfaces will be also changed. Therefore the resistance between two equipotential surfaces, denoted as $R_{1,2}$ above, will not be the same quantity for the ON and the OFF state in *Eq. 3a* and *Eq. 3b*.

This problem can be diminished by selecting the optimal measurement points for which the equipotential surfaces have the possible smallest distortion caused by the equalizing currents of vicinal coating defects. Obviously, the closer the measurement point is to the coating defect the less the shape of the equipotential surface varies on changing of the equalizing current flowing to/from the vicinal coating defect. On the other hand, the remote earth potential is also invariant to the local changes in the vicinity of any coating defect. In conclusion the point nearest to the coating defect (where the measured potential has an extreme as a function of the surface coordinates) and the remote earth potential are to be chosen to maximize the precision of the determination of the IR-free potential.

3. Experimental verification

3.1. Conditions

In order to verify the above conclusions, a test measurement was conducted on a pipeline. The pipeline was a DN 300 gas transfer line with polyethylene coating which was known to be in a bad condition. The measurement was a modified CIPS carried out with a CPM 401 universal cathodic protection diagnostic measurement system. Unlike conventional CIPS measurements, here the two reference electrodes of the mobile data logger measured different potentials: one reference electrode (electrode No. 2) was measuring the potential above the pipeline and the other electrode (electrode No. 1) was measuring the potential some 3 m apart from the pipeline (cf. *Fig. 1*). In this way the potential gradient, perpendicular to the axis of the pipeline, was determined both for the ON and OFF states from the data of the mobile data logger. The switching time was 3 second ON and 1 second OFF, the delay time after the switching was 0.1 second and the sampling time was also 0.1 second. The remote potentials were measured with a static data logger.

3.2. Results

The ON and OFF potential data for the two mobile reference electrodes and the remote potentials are shown in function of the distance in *Figure 3*, which also includes the IR-free potentials calculated for the localized coating defects determined by means *Eq. 4* and *Eq. 7*.

The IR-free potential as a function of the foreign current ratio (both determined from the data of the mobile data logger, based on *Eq. 4* and *Eq. 5*) are shown in *Figure 4*, with the best fitting line. As follows from *Eq. 7*, the slope of this linear relationship gives the difference of the remote earth ON and OFF potentials and the intercept gives the remote earth OFF potential. The obtained data, compared to the average of the experimentally measured ones are included in *Table 1*.

The "calibration curve" of the IR-free potentials obtained from *Eq. 4* and from *Eq. 7*, using the remote earth potential data and the foreign current ratio obtained from the mobile logger data are shown in *Figure 5* (the line is the y=x calibration line) and the numerical values, with the absolute value of the differences are shown in *Table 2*.

3.3. Evaluation

In *Fig. 3* six well developed coating defects are localized. The coating defects at 24 and 40 meters are very large, most likely they are more or less continuous series of coating defects of different sizes and positions. They are assumed to be "open" coating defects, where the damaged coating does not cover the exposed pipe area and the larger the coating defect the more positive the IR-free potential. The coating defect at 68 meter is presumably a blistering, because the apparent size is very small but the IR-free potential is very positive which is the sign of high ohmic potential drop due to the "coverage" by the damaged coating. The coating defects at 95, 125 and 130 meters are decreasing in apparent size but shifting to positive direction in IR-free potential and from this tendency it is assumed that their "coverage" is increasing. In conclusion, coating defects of different sizes and types are detected on the selected relatively short pipe section.

[4] A smaller coating defect has a higher resistance. However, the resistance of a coating defect decreases (approximately) linearly with the diameter of the coating defect, while the electrode surface increases with second order. Therefore a larger coating defect will always give larger ohmic potential drop in case of a similar geometry.

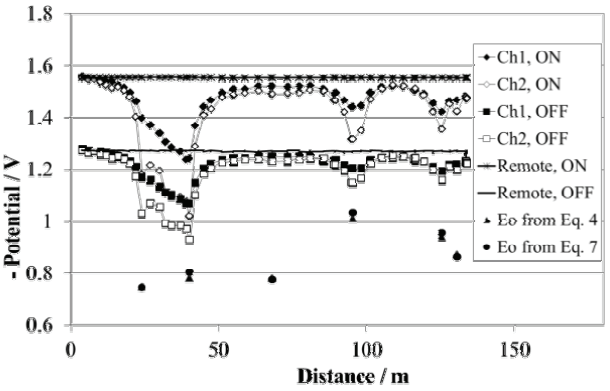

Figure 3: Measured and calculated potential data of the test measurement vs. distance

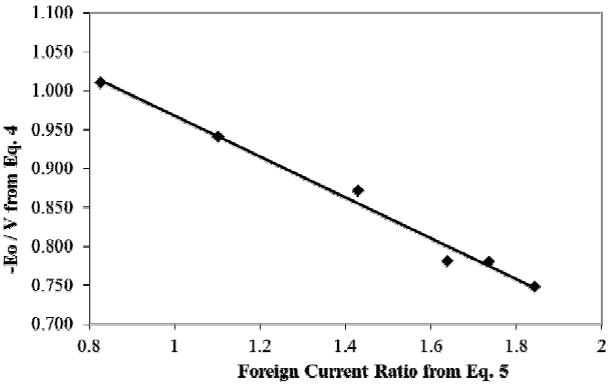

Figure 4: IR-free potential data, calculated via *Eq. 4*, vs. Foreign Current Ratio

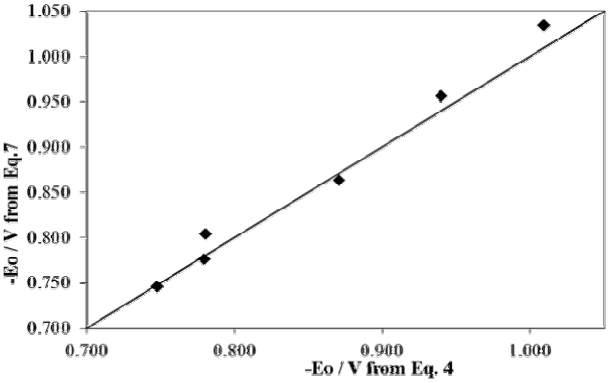

Figure 5: Calibration of IR-free potential data calculated via *Eq. 7* vs. IR-free potential data calculated via *Eq. 7*

Fig. 4 justifies the assumptions of *Eq. 7*. The linear relationship between the foreign current ratio and the IR-free potential has a "double nine" (0.993) correlation coefficient. This data has to be qualified considering the extreme differences in type and size among the coating defects. This relatively good result has to be considered also in the light of the fact that the first two defects are actually a series of defects, which decreases the applicability of the theory of the equipotential surfaces. In short, these circumstances can be considered as a near-worst-case scenario.

According to *Eq. 7*, the remote potentials can be determined from the IR-free potential vs. foreign current ratio plot. From *Tab. 1* a moderate difference of a few tens of millivolts is concluded which justifies the theoretical expectations.

Table 1: Comparison of measured and calculated values of remote earth potentials

Parameter	Measured /V	Calculated from *Eq. 7*/V	Absolute value of difference/V
Slope $\left(E_{\infty}^{OFF} - E_{\infty}^{ON}\right)$	0.284	0.262	0.022
Intercept $\left(E_{\infty}^{OFF}\right)$	-1.269	-1.229	0.04

Table 2: Values of IR-free potential at the coating defects, calculated from *Eq. 4* and *Eq. 7*

Distance/m	Calculated from *Eq. 4*/V	Calculated from *Eq. 7*/V	Absolute value of difference/V
24	0.748	0.746	0.002
40	0.780	0.804	0.023
68	0.780	0.776	0.004
95	1.010	1.034	0.025
126	0.940	0.956	0.016
131	0.871	0.863	0.008
Average			0.013

From *Eq. 7* it is also concluded that the IR-free potential of a coating defect can be determined from the potential differences measured with the two reference electrodes of the mobile data logger (i.e. it is not necessary to apply a contact to the pipeline (cf. *Fig. 1*)). In *Tab. 2* it is shown that the error of the determination of the IR-free potentials using *Eq. 7*, compared to the data using *Eq. 4*, are an average of 13 mV which is far below the practically required precision limit.

Summary

It has been shown that based on the concept of the equipotential surfaces and Ohm's Law a linear formula can be provided for the determination of the IR-free potential.

The precision of the formula is the highest if the points used for the determination of the foreign current ratio are the points nearest to the coating defect (i.e. where the measured potential data have an extreme) and the remote earth.

The theory also provides the value of the foreign current ratio.

It was pointed out that the foreign current ratio and the IR-free potential are in a linear relationship where the coefficients of the linear relationship are related to the remote earth ON and OFF potentials. This relationship establishes the connection between the "global" remote

and the locally, above the pipeline measured potentials. Also this relationship provides an alternative method for the assessment of the IR-free potential, which does not require a measuring cable to be pulled alongside the pipeline.

All these theoretical results were confirmed with a test measurement made on a section of pipeline with coating defects of different size and type. The evaluation of the test measurements justified the theoretical assumptions and proved that the determination of the IR-free potential, based on the measurement of the over-the-line potential gradients and the remote ON and OFF potential, is applicable and accurate enough for the practical requirements.

REFERENCES

1. R. J. KUHN: Bureau of Standards, 73B75 (1928)
2. J. B. BUSHMANN, F. E. RIZO: Materials Performance, July, 1978
3. W. VON BAECKMANN, W. SCHWENK AND W. PRINZ (editors): Handbook of Cathodic Protection, Gulf Professional Publishing (1997), pp. 88–96
4. W. VON BAECKMANN, H. HILDEBRAND ET AL.: Werkstoffe und Korrosion, 34 (1983), 230–235

HUNGARIAN JOURNAL
OF INDUSTRIAL CHEMISTRY
VESZPRÉM
Vol. 40 (2) pp. 83–86 (2012)

STUDY ON ANALYSIS OF ANTIBIOTIC COMPOUNDS FROM ENTHOMOPATHOGENIC BACTERIA BY FT-IR

D. VOZIK[1], J. MADARÁSZ[2], Z. CSANÁDI[1]✉, A. FODOR[3,4], K. DUBLECZ[4], K. BÉLAFI-BAKÓ[1]

[1]University of Pannonia, Faculty of Engineering, Research Institute on Bioengineering, Membrane Technology and Energetics, 10 Egyetem Str., 8200 Veszprém, HUNGARY
[2]University of Pannonia, Faculty of Engineering, Department of Organic Chemistry, 10 Egyetem Str., 8200 Veszprém, HUNGARY
[3]University of Pannonia, Georgikon Faculty, Institute of Plant Protection, 16 Deák F. Str., 8360 Keszthely, HUNGARY
[4]University of Pannonia, Georgikon Faculty, Department of Animal Sciences, CEPO Group, 16 Deák F. Str., 8360 Keszthely, HUNGARY
✉E-mail: csanadi@almos.uni-pannon.hu

Entomopathogenic bacteria produce antibiotic molecules effective against plant, animal and human plant pathogenic bacteria. They produce broad-spectrum antibiotics, which can be applied in several different fields where suppression of microbes is needed. These antibiotic molecules have different chemical structure such as peptides. Analysis and identification of these molecules provide useful ways in the research and development of drugs and agrochemicals.

Keywords: entomopathogenic bacteria, antimicrobial activity, peptides, analysis

Introduction

Insect pathogenic or entomopathogenic nematodes (EPN) and their symbiotic entomopathogenic bacteria (EPB) can be used as microbial control agents against agricultural insect pests [1]. These nematodes of *Heterorhabditis* and *Steinernema* species are symbiotically associated with the members of the bacteria family *Enterobacteriaceae* as *Photorhabdus* and *Xenorhabdus* species, respectively [2–3]. The EPB have several special functions in this symbiotic relationship. One of them is the production ability of broad-spectrum antibiotics, which keep monoxenic conditions in insect cadavers in soil [4].

Antibacterial resistance is increasing worldwide. The compounds produced by EPN symbiotic bacteria have showed a wide range of bioactivities of medicinal and agricultural interest, such as antibiotic, antimycotic and insecticidal effects [5]. These antimicrobial peptides have been successfully applied in pharmaceutics, plant disease control and many other fields [6]. Antimicrobial peptides have many beneficial characteristics, such as broad-spectrum antibiotic activity, thermal stability, and low molecular weight, and most significantly, compared with most antibiotics, they are not easy to lead to the development of resistance in the target [7]. These compounds were reported as showing in vitro activity against Gram-positive bacteria, including for example the multi-drug resistant strain of *Staphylococcus aureus*. They have diverse chemical structures including peptides as well [5].

Analytical study of these molecules can be achieved in different ways. Edman degradation, developed by Pehr Edman [8], is a method of sequencing amino acids in a peptide. In this method, the amino-terminal residue is labeled and cleaved from the peptide without disrupting the peptide bonds between other amino acid residues. A major drawback to this technique is that the peptides being sequenced in this manner cannot have more than 50 to 60 residues (and in practice, under 30). The peptide length is limited due to the cyclical derivatization not always going to completion. The infrared spectrum of a protein provides a wealth of information on structure and environment of the protein backbone and the amino acid side chains [9]. This makes infrared spectroscopy an extremely useful tool for the investigation of protein structure. The absorption of a side chain in a protein may deviate significantly from their absorption in solution or in crystal. The special environment provided by a protein is able to modulate the electron density and the polarity of bonds, thus changing the vibrational frequency and the absorption coefficient. Therefore, the band positions given in reviews should be regarded only as guidelines for interpretation of spectra [10].

In this study, we aimed the isolation and analysis of some peptide-type antibiotic compounds from two EPB strains.

Material and methods

Antibacterial peptide-producing entomopathogenic bacteria were *Xenorhabdus budapestensis* (EMA) and *Xenorhabdus szentirmaii* (EMC). They were cultured in Luria Broth (LB and LBA) liquid and solid media as previously described [11].

Cell-free culture media (CFCM) were prepared as follows: aliquots of the stock culture were added separately into 900 mL sterile medium. The flasks were incubated in a shaker at 200 rpm and 30ºC for 24 h and centrifuged at 13 000 rpm (10 000 g for 30'). After centrifugation the supernatant was filtrated through Express Plus filter (0.22 µm) (Merck Millipore).

Purification of antimicrobial compounds: 1000 mL of CFCM was mixed with activated Amberlite XAD polymeric adsorbent in a 1:20 ratio and incubated for 24 h. The resin-CFCM mixture was filtered through Millipore Express Plus filter of 0.22 µm pore-size and washed subsequently with 200 ml of distilled water, 200-200 ml of 25 V/V%, 50 V/V% and 80 V/V% methanol (MeOH), removing all inactive compounds by this way. After this the resin was washed with 200 ml cc. MeOH:HCl (99:1) and 200 ml i-propanol (*i*PrOH) to eluate biologically active compounds. These samples were evaporated by vacuum distillation and resulted samples with MeOH and *i*PrOH, respectively.

For the analysis of the purified antimicrobial compounds a Thermo Nicolet AVATAR FT-IR-330 FT-IR apparatus was used to determine FT-IR spectra and a Hitachi U-2910 UV-Vis spectrophotometer was used to form the UV spectra. Solid samples were prepared for the IR: some quantity of samples were ground with purified KBr and this mixtures were pressed in a mechanical press to form a transparent pellet through which the beam of the spectrometer can pass. Resolution: 2.000 cm^{-1}, Scans: 16.

Results and discussion

The most precise method for the protein and peptide identification after their separation by high-performance liquid chromatography (HPLC) is mass spectrometry [12]. However, this method is quite expensive. Absorbance at low wavelength (<220 nm) detects peptide bonds and amino acid residues with detection limits between nanomoles and picomoles. Peptides having aromatic residues (phenylalanine (Phe), tyrosine (Tyr), and trypthophan (Trp)) can be detected at 254 or/and 280 nm. For this reason we made a UV spectra of the purified antibiotic activity compounds. Results of these measurements are shown in *Table 1*.

Table 1: UV absorbance (nm) of the antibiotic compounds

EMA		EMC	
*i*PrOH	MeOH	*i*PrOH	MeOH
201	203	200	202
213	218	-	217

IR spectra were made with the above described method. Results of these measurements are shown in *Figures 1–4*.

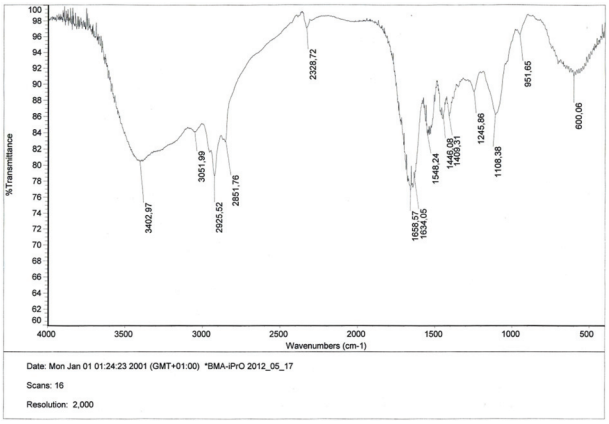

Figure 1: Antibiotic compounds purified with iPrOH from EMA

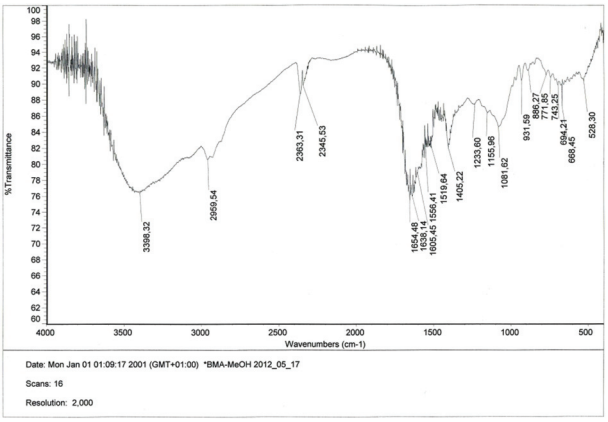

Figure 2: Antibiotic compounds purified with MeOH from EMA

In the case of amino acids only two side chain moieties absorb in spectral regions that are free from overlapping absorption by other groups and thus allow the spectroscopists an unambiguous assignment without further experiments. These are the SH group of cysteine (2550–2600 cm^{-1}) and the carbonyl group of protonated carboxyl groups (1710–1790 cm^{-1}). These groups were obtained in none of the IR spectra.

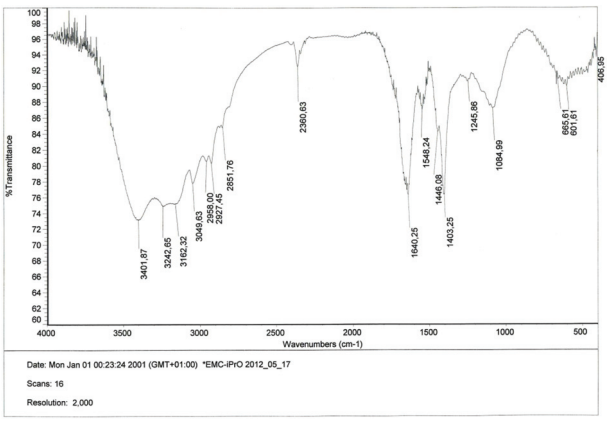

Figure 3: Antibiotic compounds purified with iPrOH form EMC

All other side chain absorption overlap with the absorption of other side chains or of the polypeptide backbone and further experiments are needed to assign an absorption band to a specific side chain moiety.

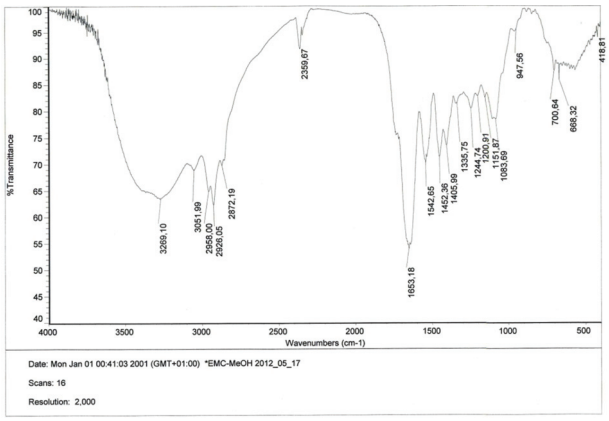

Figure 4: Antibiotic compounds purified with MeOH from EMC

The ν(C=O) vibration of glutamine side chains near 1680 cm^{-1} is a relative strong infrared absorber, the bands are sensitive to H-bonding and the band position is lower the stronger the H-bond is *(Table 2, 3)*.

The ν(C=O) vibration of the deprotonated carboxylate group of the glutamate shows two strong bands near 1400 and 1570 cm^{-1} for symmetric and antisymmetric stretching vibration, respectively *(Tab. 2, 3)*.

The ν(CN) vibration of histidine is a useful band near 1100 cm^{-1} *(Tab. 2, 3)*.

Tyrosine is a relatively strong infrared absorber due to its polar character. The most intense bands originate from ν(CC), the ν(C-O) and the δ(COH) mode near 1517, at 1235–1270 and at 1169–1260 cm^{-1} *(Tab. 2, 3)*.

Table 2: The IR spectra of EMA antibiotic compounds with different eluents

Band position in cm^{-1}		Assignment
*i*PrOH	MeOH	
1659	1654	glutamine (ν(CO) in proteins 1659–1696 cm^{-1})
1634	1638	histidine (ν(C=C) in proteins 1617 cm^{-1})
-	1605	tyrosine (ν(CC) ring in proteins 1615 cm^{-1})
1548	1556	glutamine ($\nu_{as}(COO^-)$ in proteins 1553–1575 cm^{-1})
-	1520	tyrosine (ν(CC) ring, δ(CH) in proteins 1516–1518 cm^{-1})
1446	-	lysine ($\delta(CH_2)$ in proteins 1445 cm^{-1})
1409	1405	glutamine ($\nu_s(COO^-)$ in proteins 1397–1424 cm^{-1})
1246	1234	tyrosine (δ(COH) in proteins 1228–1250 cm^{-1})
1108	1082	histidine (ν(CN), δ(CH) in proteins 1094–1114 cm^{-1})

While the $\delta_{as}(CH_3)$, the $\delta(CH_2)$ and the $\delta_s(CH_3)$ vibration near 1465, 1450 and 1375 cm^{-1} are relatively good group frequencies, the δ(CH) and $\gamma(CH_2)$ vibrations are often coupled to other modes *(Tab. 2, 3)*. The only tryptophan bands with considerable infrared intensity seem to be those at 1334 and 1455 cm^{-1} *(Tab. 2, 3)*.

Table 3: The IR spectra of EMC antibiotic compounds with different eluents

Band position in cm^{-1}		Assignment
*i*PrOH	MeOH	
-	1653	glutamine (ν(CO) in proteins 1659–1696 cm^{-1})
1640	-	histidine (ν(C=C) in proteins 1617 cm^{-1})
1548	1542	glutamine ($\nu_{as}(COO^-)$ in proteins 1553–1575 cm^{-1})
1446	1452	tryptophane (ν(CHb)[a], ν(CCb)[a], ν(CN) in proteins 1455 cm^{-1}) / lysine ($\delta(CH_2)$ in proteins 1445 cm^{-1})
1403	1406	glutamine ($\nu_s(COO^-)$ in proteins 1397–1424 cm^{-1}
-	1336	tryptophane (ν(CCp)[a], ν(CN) in proteins 1334 cm^{-1})/ lysine ($\gamma(CH_2)$, $\gamma(CH_2)$ in proteins 1345 cm^{-1}
1246	1245	tyrosine (δ(COH) in proteins 1228–1250 cm^{-1}
	1201	tryptophane (ν(CC) 1203 cm^{-1}
	1152	proline ($\gamma(CH_2)$, 1168 cm^{-1}
1085	1084	histidine (ν(CN), δ(CH) in proteins 1094–1114 cm^{-1})

"b" and "p" indicate vibrations of the benzene or pyrole moieties, respectively.

Acknowledgement

This work was partly supported by CEPO, the Austrian-Hungarian Cooperation Project for Poultry Excellence Centre, working within the frame of ERFA between 2007–2013 and TÁMOP-4.2.2/B-10/1-2010-0025.

REFERENCES

1. G. C. SMART: Entomopathogenic nematodes for the biological control of insects, Journal of Nematology, 27 (1995), pp. 529–534
2. G. M. THOMAS, G. O. POINAR: *Xenorhabdus* gen. nov., a genus of entornopathogenic, nematophilic bacteria of the family *Enterobacteriaceae*, International Journal of Systematic Bacteriology, 29 (1979), pp. 352–360

3. N. E. BOEMARE, R. J. AKHURST, R. G. MOURANT: DNA relatedness between *Xenorhabdus* spp. (*Enterobacteriaceae*), symbiotic bacteria of entomopathogenic nematodes, and a proposal to transfer *Xenorhabdus luminescens* to a new genus, *Photorhabdus* gen. nov.. International Journal of Systematic Bacteriology, 43 (1993), pp. 249–255
4. R. J. AKHURST: Antibiotic activity of *Xenorhabdus* species, bacteria symbiotically associated with insect pathogenic nematodes of the families *Heterorhabditidae* and *Steinernematidae*, Journal of General Microbiology, 128 (1982), pp. 3061–3065
5. J. M. WEBSTER, G. CHEN, K. HU, J. LI: Bacterial metabolites, In: Entomopathogenic Nematology, CABI Publishing, USA (2002), pp. 99–115
6. Y. J. GORDON, E. G. ROMANOWSKI, A. M. MCDERMOTT: A review of antimicrobial peptides and their therapeutic potential as anti-infective drugs, Current Eye Research, 30 (2005), pp. 505–515
7. Y. XIAO, F. MENG, D. QIU, X. YANG: Two novel antimicrobial peptides purified from the symbiotic bacteria *Xenorhabdus budapestensis* NMC-10, Peptides, 35 (2012), pp. 253–260
8. P. EDMAN, E. HÖGFELDT, L. G. SILLÉN, P. O. KINELL: Method for determination of the amino acid sequence in peptides, Acta Chemica Scandinavica, 4 (1950), pp. 283–293
9. A. BARTH: The infrared absorption of amino acid side chains, Progress in Biophysics & Molecular Biology, 74 (2000), pp. 141–173
10. B. HERNANDEZ-LEDESMA, L. AMIGO, M. RAMOS, I. RECIO: Application of high-performance liquid chromatography-tandem mass spectrometry to the identification of biologically active peptides produced by milk fermentation and simulated gastrointestinal digestion, Journal of Chromatography A., 1049 (2004), pp. 107–114
11. E. M. MOTITU: Evaluating antibacterial potential of entomopathogenic bacterium strains on agriculturally important plant pathogenic bacteria. Master Thesis, University of Pannonia, Georgikon Faculty, Institute of Plant Protection, Keszthely, Hungary (2011)
12. T. HERRAIZ: Sample preparation and reversed phase-high performance liquid chromatography analysis of food-derived peptides, Analytica Chimica Acta, 352 (1997), pp. 119–139

HUNGARIAN JOURNAL
OF INDUSTRIAL CHEMISTRY
VESZPRÉM
Vol. 40 (2) pp. 87–91 (2012)

BIOCATALYTIC HYDROGEN SULPHIDE REMOVAL FROM GASEOUS STREAMS

G. TÓTH ✉, É. LÖVITUSZ, N. NEMESTÓTHY, K. BÉLAFI-BAKÓ

University of Pannonia, Research Institute on Bioengineering, Membrane Technologies and Energetics,
10 Egyetem Str., 8200 Veszprém, HUNGARY
✉E-mail: tothgabor2@gmail.com

Hydrogen sulphide is one of the most important substances responsible for unpleasant odour emissions in gas phase. It is often formed in higher concentration beyond other sulphur containing volatile compounds like methane thiol (MT), dimethyl sulphide (DMS) and dimethyl disulphide (DMDS). Removal of hydrogen sulphide is usually carried out by physical-chemical methods (e.g. adsorption), but nowadays some bio-processes may be considered as promising alternatives. Certain sulphur oxidising thiobacteria can be successfully applied for hydrogen sulphide conversion from gaseous streams like biogas. Various strains have been applied so far for degradation of hydrogen sulphide, they belong mostly to the group of Thiobacillus, which are autotrophic microorganisms. These autotrophic bacteria have the drawback in application that they grow slower than the heterotrophic ones and it is more difficult to control their growth. A number of chemotrophs are suitable for the biodegradation of H_2S. These bacteria grow and produce new cell material by using inorganic carbon (CO_2) as a carbon source and chemical energy from the oxidation of reduced inorganic compounds such as H_2S.The objective of the work described here was to study the ability of elimination of hydrogen sulphide by two chemotrophic microorganisms (*Thiomonas intermedia, Thiobacillus thioparus*) in a batch bioreactor. The other aim was the study of the immobilization of these bacteria to different supports.

Keywords: hydrogen sulphide, chemotrophic, biological oxidation *Thiomonas intermedia*, *Thiobacillus thioparus*, batch reactor, support

Introduction

Volatile sulphuric compounds like methane thiol (MT), dimethyl sulphide (DMS), dimethyl disulphide (DMDS) are harmful, corrosive components, and present in various gas streams, e.g. biogas [1, 2], among them hydrogen sulphide can be found in relatively high concentration.

The concentration of hydrogen sulphide varies between 0,1 és 2% and depends on the quality of feed substance [3]. Utilisation of biogas is mainly hindered by its hydrogen sulphide content, therefore its removal is essential. The current technologies based on chemical removal are quite expensive, thus usage of biogas in power plants is not supported [4].

Yet, in most cases physico-chemical methods are used. Recently biological processes received some attention due to their effectiveness and low operational and maintenance costs [2], [4]. Biological removal of hydrogen sulphide can be carried out by autotrophic and heterotrophic ways. From the operation point of view heterotrophic strains are more beneficial, but mos chemoautotrophic bacteria seem suitable for degradation of the compound. These bacteria can live using inorganic carbon (e.g. CO2) as carbon source, while energy is obtained by oxidation of reduced compounds (e.g. H_2S) [5].

The aim of this work was to study a suspended batch bioreactor, where chemoautotrophic aerob bacteria (*Thiomonas intermedia, Thiobacillus thioparus*) are able to use carbon dioxide present as carbon source, while hydrogen sulphide is converted into sulphur powder or oxidised sulphur compounds. The investigations were conducted in liquid phase by using free and immobilised cells.

Materials and methods

Microorganisms

Thiomonas intermedia is an aerobic, chemoautotrophic bacterium, purchased in lyophilised state from the National Collection of Agricultural and Industrial Microorganisms (NCAIM Budapest, Hungary). For its growing Thiomonas intermedia broth elaborated by DSMZ (Deutsche Sammlung von Mikroorganismen und Zellkulturen GmbH, Germany) was used [6]. Its composition is (g/L): NH_4Cl 0.1, KH_2PO_4 3.0, $MgCl_2$*6 H_2O 0.1, $CaCl_2$ 0.1, $Na_2S_2O_3$*5 H_2O 5.0, yeast extract 1.0, 1000 ml distilled water. During the growing period pH was adjusted to 5.5–6.0, then it was incubated at 33°C temperature and 120 rpm.

The other, also chemoautotrophic aerobic bacterium is *Thiobacillus thioparus*, which was purchased from DSMZ (Germany) strain collection. Its growing parameters are the same as given in *Thiomonas intermedia*. The features of microorganisms are summarized in *Table 1*.

Table 1: The features of *Thiomonas intermedia* és a *Thiobacillus thioparus*

	Thiobacillus thioparus	*Thiomonas intermedia*
optimal pH	5–9	5–7.5
optimal temperature [°C]	33–35	30–35
cell type	Gram negative	Gram negative
Shape, size	rod, 0.9–1.8 µm	-
Trophity	obligate chemoautotrophic	facultative chemoautotroph
Energy source	Thiosulphate, sulphide	Thiosulphate, sulphide
Oxygen demand	aerob	aerob
Source	[7]	[8]

Analysis

To follow the concentration of hydrogen sulphide in the liquid phase a photometric method was applied. The principle of the measurement is that the sulphide in acidic environment gives a colourful reaction with N,N-dimethyl-p-phenilene diamin resulting in methylene blue, which can be measured by photometer in 670 nm after 20 min reaction time, using 5 cm cuvette (HachLange DR 3800) [9]. The advantages of the method are that easily applicable, having good reproducibility and the measuring range is wide: between 0.1 and 1.2 mg S^{2-}/L.

The composition of the gas phase was determined by Dräger X-am 7000, which is a mobile electrochemical device, able to detect hydrogen sulphide and carbon dioxide.

The experiments were carried out in 250 ml, jacketed, thermostated reactor *(Figure 1)*, where the total volume of the liquid phase was 200 ml. Its composition was: 10% inoculum, 5%, water containing 2500 mg/L hydrogen sulphide and 85% broth. The optical density of the samples were measured by a photometer (HachLange DR 3800), in 620 nm. The biochemical reactions in the reactor resulted in a decrease of sulphide content in the liquid phase.

The water vapour in the gas phase disturbs the optimal operation of the gas analysis equipment, therefore the vapour had to be condensed before. Samples were taken every half an hour during the exponential growing period of the bacterium, otherwise it was taken every hour, and dissolved sulphide concentration and optical density were determined.

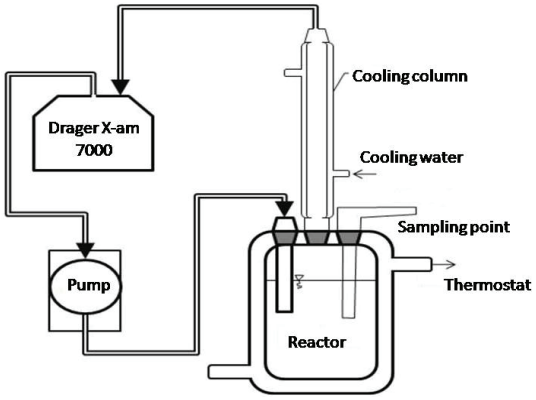

Figure 1: Set-up of the batch reactor

Immobilization

The strains were immobilised in three types of supports and the process was checked in a serial of measurements. MAVICELL-B cellulose beads, alginate beads and granulated activated carbon were used in the experiments.

MAVICELL-B *(Table 2)* is cellulose beads, widely used for immobilization of various microbes, having large adsorption surface area, thus a highly suitable support, moreover it can withstand to the corrosive effect of hydrogen sulphide. The cells can be bound on the surface of the support by adsorption.

Table 2: Features of MAVICELL-B

Feature	
Regenerated cellulose content	45–55%
Ash	35–40%
Particle size	2–3.5 mm
Aggregate thickness	250–300 g/dm^3
water uptake at 25ºC	150–200%
Special pore volume	1.5–2 cm^3/g
Special pore surface area	8–10 m^2/g
Swelling	
increase in diameter	1.5 fold
increase in volume	3 fold

The other support used was alginate beads, widely used in biotechnology for immobilization of cells and enzyme, *(Figure 2)* by the so called entrapment technique. During jellification small hollows are formed in alginate where biocatalysts (enzymes and cells) can be entrapped. The structure of the gel is compatible with the biocatalysts, thus no chemical modification is needed [10].

Finally the granulated activated carbon (GAC) support was purchased from Airwatec s.a. (Belgium).

Figure 2: Alginate beads containing cells

Due to its high surface area it seems also a promising support material for immobilisation of microorganisms. The features are listed in *Table 3*.

Table 3: Features of activated carbon

Parameter	Value
Total surface area (BET) (m^2/g)	1080
pH	7.0
Water content (%)	1,1
Ash content (%)	8.6
Granules Diameter (mm)	1.0

During the experiments immobilised strains were kept in two vessels (for the two strains) and a blind one was used as a control, for all the three types of immobilization. Samples were taken from all vessels regularly, and sulphide contents were determined. Then fresh broth was given to the strains.

In the end of the experiments the amount of immobilised cells (on the surface of MAVICELL and activated carbon particles, as well as in the alginate beads) – or more precisely the protein content – was measured by the modified Folin-method.

Results

Firstly 24 h long batch fermentations were carried out by free *Thiomonas intermedia* and *Thiobacillus thioparus* microbes. The results are shown in *Figure* ***3*** and *Figure* ***4***.

As it can be seen from *Figure* ***3*** and *Figure* ***4*** after a 8–12 h lag phase bacteria started to grow, the exponential growing period was found from around 10th h till 15-16th h, then a the rate of growing was slower. All the four parameters measured confirmed that the maximal growing rate of both bacteria was at the 12–13th h of the fermentations.

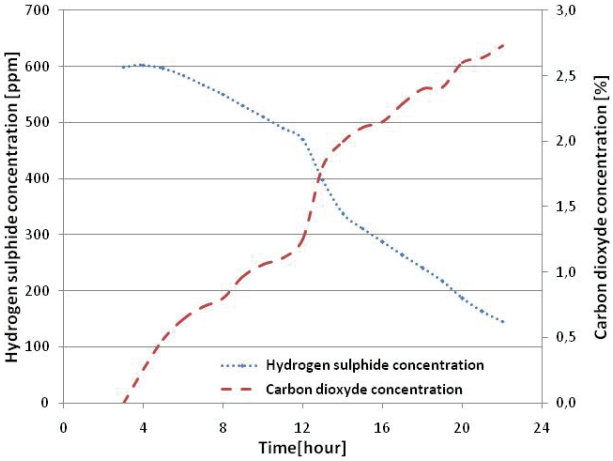

a

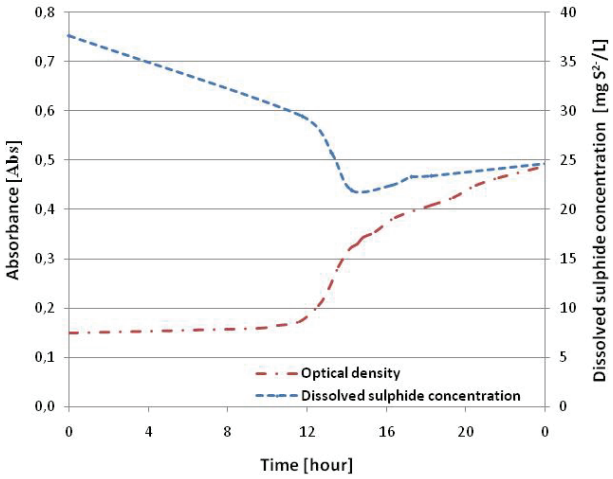

b

Figure 3: Concentration of hydrogen sulphide and carbon dioxide (a), dissolved sulphide and optical density of *Thiomonas intermedia* (b) as a function of time

Moreover it can be established that both *Thiomonas intermedia* and *Thiobacillus thioparus* reduced the concentration of hydrogen sulphide in the reaction mixture, i.e. they mostly obtained energy from degradation of hydrogen sulphide (dissolved sulphide) during the metabolisms.

In both *Figures 3/b* and *4/b* dissolved sulphide concentration as a function of time shows some discrepancy, which is difficult to explain. We think that the analytical method (by photometer) may be disturbed by some nutrient compound present in the liquid phase, therefore another method should be found in future. Another reason of the strange behaviour might be that certain metabolic products were formed during the fermentation which resulted it in the second half of the experiments.

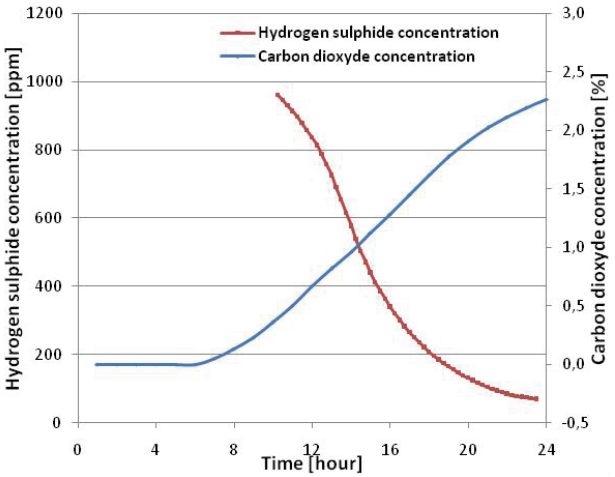

a

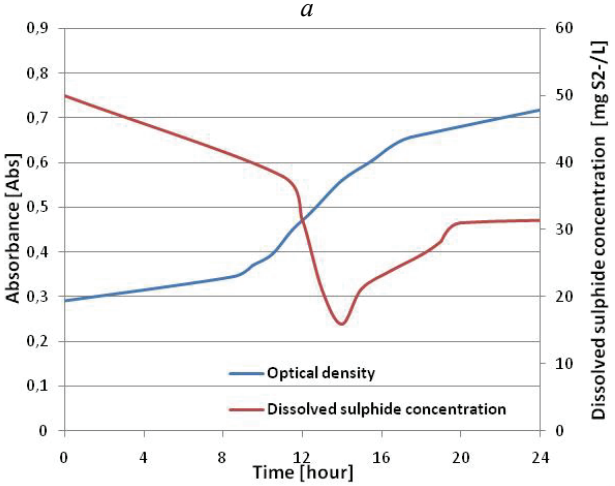

b

Figure 4: Concentration of hydrogen sulphide and carbon dioxide (a), dissolved sulphide and optical density of *Thiobacillus thioparus* (b) as a function of time

Operational stability in the liquid phase

The bacteria were immobilised in three different support: MAVICELL-B cellulose beads, alginate beads and granulated activated carbon. To check their work they were kept in reaction mixtures, containing nutrients and hydrogen sulphide, and samples were taken regularly. *Figure 5* presents the experimental results: the variation of hydrogen sulphide concentration [mg S^{2-}/L] compared to the control (bind) one as a function of reaction time in cases of MAVICELL-B cellulose beads *(Fig. 5/a)*, alginate beads *(5/b)* and granulated activated carbon *(5/c)*.

It can be observed that a decrease in hydrogen sulphide concentration compared to the blind was measured, due to the activity of the bacteria immobilised on the support.

To check this phenomenon protein content of the supports (measured in the end of the experiments by washing out the microbes from the surface of the support, or – in case of alginate – destroying the gel structure) was determined. The results are summarized in *Table 4*.

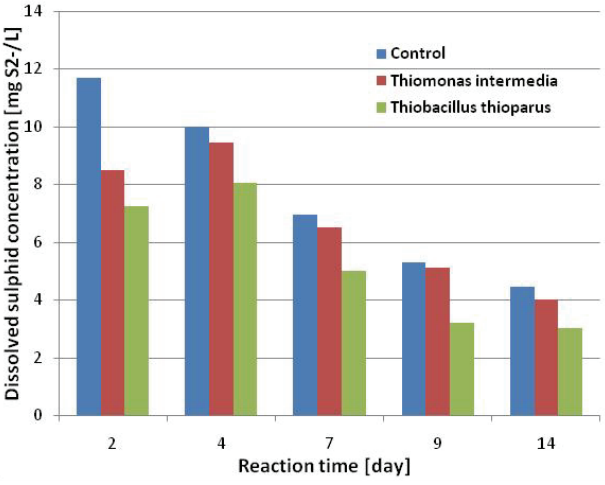

a

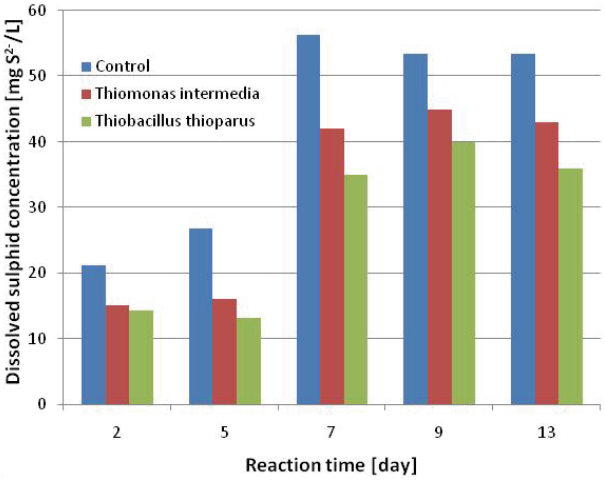

b

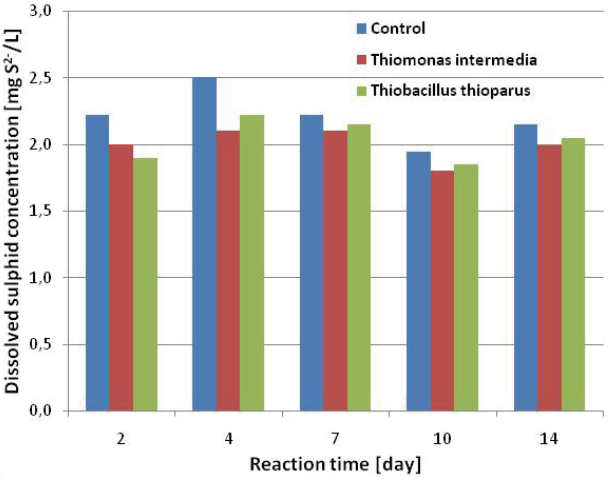

c

Figure 5: Operational stability of bacteria immobilised in MAVICELL-B (a), Ca-alginate (b) and activated carbon granulates (c)

From the *Table 4* it can be seen that the protein measurement confirmed our experimental results: considerable amount of microbes were immobilised on all of the supports. Since bacteria were entrapped in

alginate (not only adsorbed on the surface), much higher protein content was found in that case.

Table 4: The amount of protein (microbes) measured in the various support

	Mavicell-B	Ca-alginate	GAC
Thiomonas intermedia [mg DM/g carrier]	0.12	6.3	0.15
Thiobacillus thioparus [mg DM/g carrier]	1.83	7.1	2.05

It can be stated that the bioconversion processes can be followed by measuring the hydrogen sulphide concentration in the liquid phase, but the photometric determination of the total sulphide content can not be applied here. Based on the protein determination it is obvious that the microbes were able to immobilise in the supports and worked properly to reduce hydrogen sulphide concentration in the liquid phase.

Evaluation

As a summary it can be stated that our experiments proved: the two microbes investigated are suitable for the biological degradation, removal of hydrogen sulphide. However, the analytical method to follow the bioconversions should be improved and we should continue the experiments in gas phase. Based on the successful immobilisation and measurements in liquid phase, the bioreactor system should be redesigned to be able to operate in gas phase and to determine exactly the ability and effectiveness of the bacteria.

Acknowledgement

The research work was partly supported by the „Social Renewal Operational Programme" (New Széchenyi Plan) in the frame of TÁMOP-4.2.2.A-11/1/KONV-2012-0038 project, entitled „Complex multidisciplinary investigation of the effects of human activity and the related social conflicts on a sensitive geographical area pertaining to a shallow lake (the water body of Lake Balaton and its southern catchment area). The project is supported by the European Union and co-financed by the European social Fund.

REFERENCES

1. K. S. Cho, M. Hirai and M. Shoda: Degradation of hydrogen sulfide by *Xanthomonas* sp. strain DY44 isolated from peat, Appl. Environ. Microbiol., 58 (1992), pp. 1183–1189
2. E. Szentgyörgyi, N. Nemestóthy, K. Bélafi-Bakó: Application of membranes in biogas production, Desalination and Water Treatment, 14 (2010), pp. 112–115
3. G. Lastella, C. Testa, G. Cornacchia, M. Notornicola, F. Voltasio, V. K. Sharma: Anaerobic digestion of semi-solid organic waste: Biogas production and its purification, Energy Conversion and Management, 43 (2002), pp. 63–75
4. G. Tchobanoglous, F. L. Burton, H. D. Stensel: Wastewater Engineering. Treatment and Reuse, 4th edition McGraw-Hill Companies, New York (2003), Cap. 14., 1505–1532
5. M. L. Prescott, P. J. Harley, A. D. Klein: Microbiology, 5th edition. McGraw-Hill Companies, New York (2003)
6. www.dsmz.de
7. L. Vlasceanu, R. Popa, K. B. Kinkle: Characterization of *Thiobacillus thioparus* LV43 and its distribution in a chemoautotrophically based groundwater ecosystem, Applied and Environmental Microbiology 63(8) (1997), pp.3123–3127
8. S. K. Panda,V. Jyoti, B. Bhadra, K. C. Nayak, S. Shivaji, F. A. Rainey, S. K. Das: *Thiomonas bhubaneswarensis* sp. nov., an obligately mixotrophic, moderately thermophilic, thiosulfate-oxidizing bacterium Int. J. Syst. Evol. Microbiol., 59 (2009), pp. 2171–2175
9. J. D. Cline: Spectrophotometric Deter-mination of Hydrogen Sulfide in Natural Waters, Department of Oceanography, University of Washington Seattle, 14 (1969), pp. 454–458
10. L. Boross, Cs. Sisak, B. Szajáni: Szilárd fázisú biokatalizátorok – Előállításuk, tulajdonságaik és gyakorlati alkalmazásuk, Akadémiai Kiadó, Budapest (2008), pp. 53–54

HUNGARIAN JOURNAL
OF INDUSTRIAL CHEMISTRY
VESZPRÉM
Vol. 40 (2) pp. 93–99 (2012)

OPTIMAL DESIGN OF HIGH-TEMPERATURE THERMAL ENERGY STORE FILLED WITH CERAMIC BALLS

T. BORBÉLY[1]✉

[1]University of Pannonia, Institute of Mechanical Engineering, 10 Egyetem Street, H-8201 Veszprém, HUNGARY
✉E-mail: borbelyt@almos.vein.hu

The momentary amount of the available solar energy and the demand usually are not equal during the usage of solar energy for heating and electric power supply. So it is necessary to store the heat energy. This article shows optimal design of a new construction, sensible heat store filled with solid heat storage material. The planned heat store has cascade system formed a spiral flow-path layout. This is a conceptual model, worked out in case of packed bed with ceramic balls. The aim of the special layout is to realize better overall efficiency than regular sensible heat stores have. The new construction would like to get higher overall efficiency by long flow-way, powerful thermal stratification and spiral flow-path layout which can ensure lower heat loss. The article shows the calculation method of the simulation of the charge and discharge and the calculation method of the overall efficiency using the results of the simulations. The geometric sizes and operating parameters of the thermal energy store with the best overall efficiency were calculated using genetic algorithm (GA). The results of the calculation tasks show that a thermal energy store with long flow-way, with cascade system formed spiral flow-path layout has higher overall efficiency than an one-duct, short flow-way thermal energy store which has equal mass of solid heat storage material as the long flow-way one, mentioned before.

Keywords: solar energy, heat storage, solid charge, sensible heat, optimization

Introduction

The possible thermal energy storing methods are: sensible heat storage, latent heat storage, sorption heat storage and chemical energy storage [1–8].

The simplest way is the storage of sensible heat, by heating a heat storage material without phase changing. The energy density of the sensible heat storage will be high if the specific heat and the density of the heat storage material are great as well [9].

Out of the materials which can be found in the environment in large quantity, the water has the greatest volumetric heat capacity (~4.18 MJ/m^{3}K), but water can be applied at atmospheric pressure up to 100ºC only. The heat transport media of the concentrated solar power systems can be used as heat storage liquids as well. The melt of the solar salt (60% $NaNO_3$ + 40% KNO_3) is used out of these materials in concentrated solar power plants as heat storage material (operating temperature range 260–550ºC, volumetric heat capacity ~2.84 MJ/m^{3}K [11]). It is not flammable, not toxic, and not too expensive.

The volumetric heat capacity of some solid materials (magnesite, corundum) – because of their higher density – come near to the volumetric heat capacity of the water with much higher upper temperature limits (magnesite 3.77 MJ/m^{3}K, corundum 3.3 MJ/m^{3}K, cast iron 4.1 MJ/m^{3}K [10]).

Screened pebble stone, cracked stone (1.5–2.5 MJ/m^{3}K), concrete (0.8–1.8 MJ/m^{3}K), wet soil (3.56 MJ/m^{3}K) [10] are used as sensible heat storage materials, because they are inexpensive.

The sensible heat stores are typical regenerative heat-exchangers. These are instationary thermal state heat-exchangers. The regenerators are long ago applied, great heat capacity heat stores with solid fill and with short charge-discharge cycle time (10–7200 s).

My aims were to study the possible interior structure of the long-term heat stores, the charge-discharge process, to calculate the optimal geometric sizes and operating parameters of those.

Comparison of short (L/D<10) and long (10<L/D) heat stores

The temperature-place function of the heat transport medium is similar to the temperature-place function of the solid heat storage material at a moment (the temperature of the heat transport medium t_f is higher at charge, lower at discharge than the t_s temperature of the solid heat storage material), so it is enough to show the temperature-place functions of the solid heat storage material.

Charge

The hot heat transport medium gives a part of its heat content to the solid heat storage material by flowing

through the heat store, which is cold at the beginning of the charge period.

In case of short heat store the outlet temperature of the heat transport medium and the solid heat storage material are increasing soon after the beginning of the charging *(Figure* 1*)*, in case of long heat store they start to increase only at the end of the charge period *(Figure 2)*.

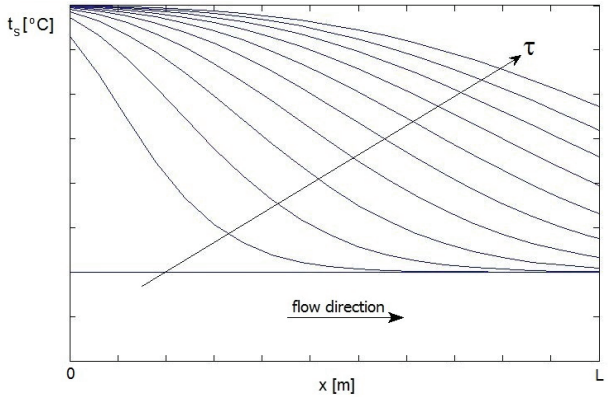

Figure 1: The temperature-place functions of the solid heat storage material during charge, in case of short heat store

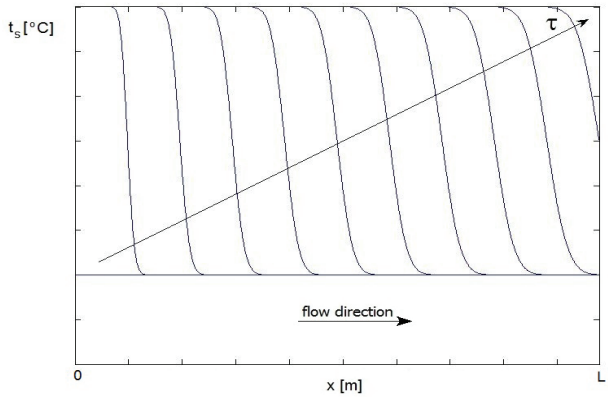

Figure 2: The temperature-place functions of the solid heat storage material during charge, in case of long heat store

Discharge

In the discharge period the cold heat transport medium flows through the hot heat store in opposite flow direction of the charge.

In case of short heat store the outlet temperatures of the heat transport medium and the solid heat storage material are decreasing soon after the beginning of the discharging *(Figure 3)*, in case of long heat store they start to decrease only at the end of the discharge period *(Figure 4)*.

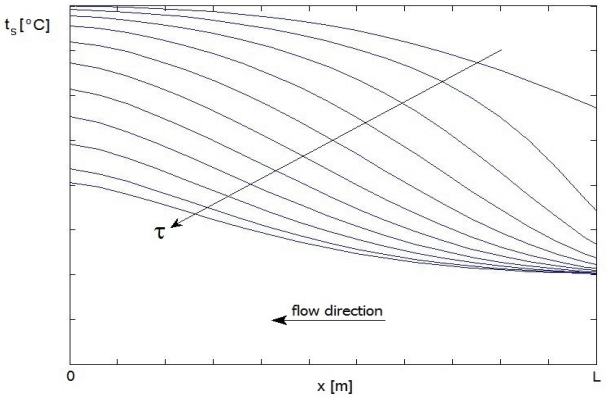

Figure 3: The temperature-place functions of the solid heat storage material during discharge, in case of short heat store

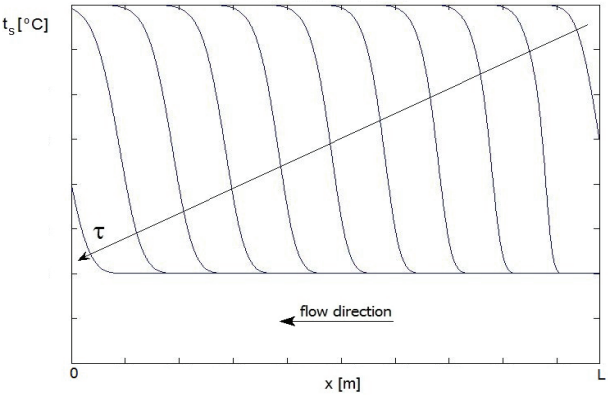

Figure 4: The temperature-place functions of the solid heat storage material during discharge, in case of long heat store

Basic idea of the cascade system heat store

During the charging and discharging of the long heat store the thermocline zone is located only in a part of the length of the heat store. It is plausible solution to divide to sections the heat store and allow knocking-off the sections from the flow-path of the heat transport medium. Let's call these sections as ducts. In case of the cascade system heat store the heat transport medium must flow through only the ducts where the thermocline zone is going along. The transport power demand of the heat transport medium can be reduced by this solution.

The heat-loss of the heat store into the environment will be small if the heat store has small specific surface. From the prismatic bodies the cylinder with H/D=1 ratio has the smallest specific surface, followed by the regular n-sided prism with H/S=1 ratio (assuming that the heat-loss flux is approximately equal in all sides of the body).

The higher heat-loss of the long heat store (because of its greater specific surface) can be reduced by using cascade system of the ducts formed a spiral flow-path layout *(see later on Figure 5)*.

Out of the regular n-sided prisms the six-sided can be built from cylinders with the best space utilization.

The geometry and operating of the heat store filled with ball particles

The ducts of the heat store filled with ball particles are cylinders made of metal sheet with outer thermal insulation *(Fig. 5)*. The metal shell holds the bed of the particles, and the heat transport medium. The thermal insulation supports the thermal stratification in radial direction. To choose cylindrical shape for the ducts is necessary – because of the pressure of the packed bed of bulk particles.

The outer geometry of the heat store is regular hexagonal prism with $H/S_t \approx 1$ ratio and cascade system of the ducts formed a spiral flow-path layout.

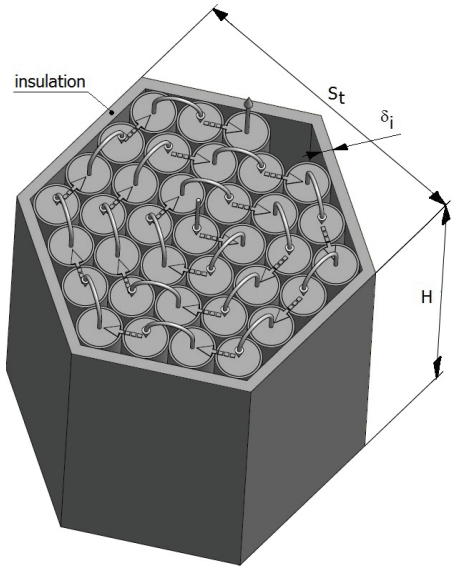

Figure 5: The construction layout of the heat store filled with ball particles and arrangement in the cascade system with spiral connection
S_t – side distance of the heat store, H – bed height of a duct, δ_i – thickness of the outer thermal insulation

The number of ducts N_j is an odd one in case of full filling, but leaving out the last duct we get an even number, so it is possible to lock out or join in the heat transport medium flow into any duct-pairs (duct-pair means a pair of ducts, one downwards and another upwards). This way the place of the last duct could be used e.g. for service purpose.

The hot heat transport medium is put in at the top of the middle duct at the beginning of charge and it flows downwards, it turns in the return band flows into the next duct (the lower connecting of the ducts is signed with dashed arrow) and flows trough that upwards. The heat transport medium coming out from the second duct can be led to the next pair of ducts. The heat transport medium must flow through only the ducts where the thermocline zone is going along. In the discharge period the cold heat transport medium flows through the hot heat store opposite to the flow-direction of the charge (from outside to middle).

The main sizes of a duct of the heat store can be seen in *Figure 6*.

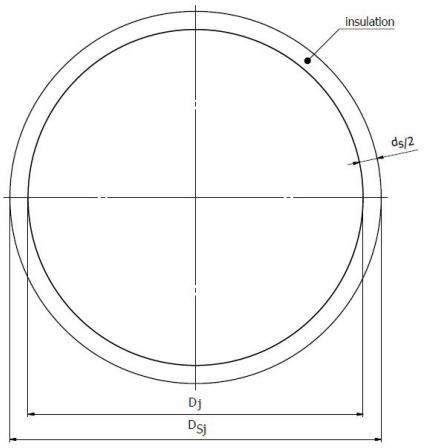

Figure 6: Top view of a duct
D_{Sj} – outside diameter of the insulated duct, D_j – inside diameter of the duct, d_s – whole thickness of the thermal insulation between two ducts

Basic differential equations of the heat transport in the heat store filled with ball particles

K. A. R. Ismail, and R. Stuginsky Jr. [126] have reported an excellent comparative analysis of several models for description of the heat transfer in the heat transport medium and the solid heat storage material.

For both media I have chosen a bit simpler model than the general, one-dimensional model. The heat-loss boundary condition is not included in the differential equations, because it takes effect only at the outer ducts, the effect of it will be calculated separately from the calculation of the temperature-place functions.

The differential equation for the description of the heat transfer in the heat transport medium is

$$\varepsilon\ \rho_f\ c_f\left(\frac{\partial t_f}{\partial \tau} + w_f\ \frac{\partial t_f}{\partial x}\right) = \alpha_f\ a_p (t_s - t_f)\,, \qquad (1)$$

where:

t_f – temperature of the flowing heat transport medium,
t_s – temperature of the solid heat storage material,
ρ_f – density of the heat transport medium,
c_f – specific heat of the heat transport medium,
w_f –average velocity of the heat transport medium in the flow-channels,
a_p – superficial particle area per unit bed volume,
α_f – heat transfer coefficient between the flowing heat transport medium and the solid heat storage material,
ε –void fraction of the bed.

The superficial ball particle area per unit bed volume a_p is

$$a_p = \frac{6}{d_b}(1-\varepsilon)\,, \qquad (2)$$

where: d_b – diameter of the ball particle.

The differential equation of the heat transfer in the heat transport medium was discretized by applying explicit forward difference scheme in time and upwind difference scheme in space [13, 14].

The differential equation for the description of the heat transfer in the solid heat storage material is

$$(1-\varepsilon)\ \rho_s\ c_s \frac{\partial t_s}{\partial \tau} = \lambda_{seffx} \frac{\partial^2 t_s}{\partial x^2} + \alpha_f\ a_p (t_f - t_s)\,, \quad (3)$$

where:

ρ_s – density of the solid heat storage material,

c_s – specific heat of the solid heat storage material,

λ_{seffx} – effective axial thermal conductivity of the solid heat storage material.

The effective axial thermal conductivity of the solid heat storage material λ_{seffx} is

$$\lambda_{seffx} \frac{1}{\frac{\varepsilon}{\lambda_f} + \frac{(1-\varepsilon)}{\lambda_s}}\,, \quad (4)$$

where:

λ_f – thermal conductivity of the heat transport medium,

λ_s – thermal conductivity of the solid heat storage material.

The differential equation of the heat transfer in the solid heat storage material was discretized by applying explicit forward difference scheme in time and centred difference scheme in space (FTCS) [13, 14].

The heat transfer coefficient between the flowing heat transport medium and the solid heat storage material was calculated according to [15].

The design variable

It is practical to choose the diameter of the ball particle d_b for optimization design variable: $x_1=d_b$. The flow velocity of the heat transport medium w_f has the greatest influence on the charging of the heat store, but it depends on the void fraction ε only (at given inside diameter of the duct D_j). In case of the bed filled with uniform ball particles the void fraction ε is independent from the diameter of the particle d_b.

Definition of the restrictions

Geometric restrictions

The lower limit of the diameter of the ball particle d_b is restricted by the manufacturing technology and the pressure drop, and the upper limit is also restricted by the minimal way-length of the heat transfer in the heat storage material.

Limits for x_1 design variable are

$$0.01\ \text{m} \le x_1 \le 0.1\ \text{m}\,. \quad (5)$$

For the minimal specific surface the best value of the geometric ratio could be

$$\frac{H}{S_t} \approx 1\,. \quad (6)$$

Pressure drop restriction

The pressure drop of the heat transport medium flowing through the packed bed in case of incompressible medium, according to [16] is

$$\Delta p' = L \left[150 \frac{(1-\varepsilon)^2}{\varepsilon^2} \frac{\rho_f\ \nu_f}{{d_b}^2} w_f + 1{,}75 \frac{1-\varepsilon}{\varepsilon} \frac{\rho_f}{d_b} {w_f}^2 \right], \quad (7)$$

where:

ν_f – kinematic viscosity of the heat transport medium.

The pressure drop of the heat transport medium must be restricted in order not to be necessary to install pressure resistant shell, not to get high transport work demand, can be negligible the compressibility of the gas and may be sufficient to use ventilator instead of blower or compressor in case of gas heat transport medium.

The upper pressure drop limit for L=2H flow-way length according to the previous requirements is

$$\Delta p'_{2H} \le 10000\ \text{Pa} = 0.1\ \text{bar}\,. \quad (8)$$

Composition of the objective function

The objective function is the overall efficiency of the heat storage, which is suitable to compare the variants of the heat stores. The optimal sizes and operating parameters could be got from the maximum-point of the objective function.

In the calculation of the overall efficiency I relate the part of the extractable heat quantity which can be used for heating and electric power production to the sensible heat storage capacity of the heat store as it is here:

$$\eta_o = \frac{Q_{hid} - Q_l - Q_{tr}}{Q_{cap}}\,, \quad (9)$$

where:

Q_{hid} – extractable heat quantity from the heat store during a charge-discharge cycle without heat-loss,

Q_l – heat-loss to the environment through the boundary surfaces during a charge-discharge cycle,

Q_{tr} – heat-equivalent of the transport work demand during a charge-discharge cycle,

Q_{cap} – sensible heat storage capacity of the heat store between the inlet and outlet temperature of the heat transport medium at the charge.

The optimal value of the design variable can be searched by optimization using the calculation of the

temperature-place functions during the whole length of the charge-discharge cycle.

The heat quantity Q_{hid}

The heat quantity Q_{hid} is the difference between the heat-content of the heat store after charge and after discharge without heat-loss.

It is necessary to know the temperature-place functions of the heat store at the end of the charge and at the end of the discharge.

The heat quantity Q_{hid} is

$$Q_{hid} = \int_0^{N_j H} c_s \rho_s (1-\varepsilon) \frac{D_j^2 \pi}{4} \left(t_s(x,\tau_c) - t_s(x,\tau_c+\tau_d)\right) dx \,, \quad (10)$$

where:

τ_c – term of charge,

τ_d – term of discharge.

The final temperature-place function of the charge of the heat store is the initial condition of the discharge. In the discharge period the heat transport medium flows through the heat store in opposite flow direction of the charge.

The heat quantity Q_l

The heat quantity Q_l is the heat-loss into the environment through the boundary surfaces during a charge-discharge cycle is

$$Q_l = Q_{lr} + Q_{ls} + Q_{lb} \,, \quad (11)$$

where:

Q_{lr} – heat-loss to the environment through the roof surface,

Q_{ls} – heat-loss to the environment through the side surfaces,

Q_{lb} – heat-loss to the environment through the bottom and the ambient ground.

The calculation of the heat-loss has taken into account the temperature of the heat store changing in place and time.

The heat quantity Q_{tr}

The heat quantity Q_{tr} is the heat-equivalent of the transport work demand during a charge-discharge cycle. The heat quantity Q_{tr} is approximated

$$Q_{tr} = \frac{(N_{j2Hc}\ \tau_c + N_{j2Hd}\ \tau_d)\dot{m}_f\ \rho_f\ \Delta p'_{2H}}{\eta_{oh}} \,, \quad (12)$$

where:

N_{j2Hc} – average number of duct-pairs which are simultaneously used during the charge,

N_{j2Hd} – average number of duct-pairs which are simultaneously used during the discharge,

$\dot{m}_f$ – mass flow rate of the heat transport medium,

$\Delta p'_{2H}$ – pressure drop of the heat transport medium on L=2H flow-way length,

η_{oh} – overall efficiency of the electric power production in a heat power station.

The heat quantity Q_{cap}

The heat quantity Q_{cap} is the sensible heat storage capacity of the heat store between the inlet and outlet temperature of the heat transport medium at the charge:

$$Q_{cap} = \dot{Q}_f\ \tau_c = \dot{m}_f\ c_f(t_{f,ci} - t_{f,co})\ \tau_c = m_s\ c_s(t_{s,ce} - t_{s,cs}) \,, \quad (13)$$

where:

$\dot{Q}_f$ – heat current during the charge,

$t_{f,ci}$ – inlet temperature of the heat transport medium at charge,

$t_{f,co}$ – outlet temperature of the heat transport medium at charge,

m_s – mass of the heat storage material,

$t_{s,cs}$ – (homogeneous) temperature of the solid heat storage material at the start of the charging,

$t_{s,ce}$ – (homogeneous) temperature of the solid heat storage material at the end of the charging.

Basic data of the optimization task

I have made the calculations during the optimization with the following main data:

τ_c=63 day=1512 h=5 443 200 s, $\dot{Q}_f$ =2 MW, $t_{f,ci}$=400°C, $t_{s,cs}$=100 °C, d_s=0.2 m.

τ_d=58 day=1392 h=5 011 200 s.

The solid heat storage material is magnesite, its physical properties are at $t_{s,mid}$ [10]:

$t_{s,mid}=(t_{s,cs}+t_{s,ce})/2=(100°C+400°C)/2=250°C$

λ_s=23.26 W/mK, ρ_s=3500 kg/m^3, c_s=1077.5 J/kgK.

The required mass of the heat storage material for an ideal heat store: m_s=33 678 t, ε=0.3.

The heat transport medium is nearly ambient pressure air, its physical properties are at $t_{f,mid}$ [10]:

$t_{f,mid}=(t_{f,ci}+t_{f,co})/2=(400°C+100°C)/2=250°C$

λ_f=0.0425 W/mK, ρ_f=0.6715 kg/m^3, c_f=1038.5 J/kgK, $\nu_f=4.1525\cdot10^{-5}$ m^2/s.

The final temperature-place function of the charge of the heat store is the initial condition of the discharge.

The mass flow rate of the heat transport medium is constant during the charge-discharge process.

The inlet temperature of the heat transport medium during discharge is: $t_{f,di}$=100°C.

Data of the outer thermal insulation: λ_i=0.0468 W/mK, δ_i=1 m.

η_{oh}=0.3.

I have applied the genetic optimization algorithm of the Matlab software in order to find the optimal geometric sizes and operating parameters of the thermal energy store with the best overall efficiency.

Optimal sizes and operating parameters of the thermal energy store with the best overall efficiency

The optimization process has been executed with number of ducts N_j=1, 6, 18. The results are summarized in *Table 1* and *Figure 7*.

Table 1: Optimal sizes and overall efficiencies with several number of ducts

N_j [-]	1	6	18
x_1 [m]	0.045	0.1	0.1
H [m]	27.5	29.6	28.8
L [m]	27.5	177.6	518.4
D_{Sj} [m]	25.5	10.1	6.0
S_t [m]	27.5	29.6	28.8
d_b [mm]	45	100	100
w_f [m/s]	0.064	0.412	1.203
Q_{cap} [PJ]	10.89	10.89	10.89
Q_{hid} [PJ]	8.45	9.38	9.98
Q_l [PJ]	0.92	1.11	1.01
Q_{tr} [PJ]	0.01	0.25	2.87
η_o [-]	0.6908	0.7363	0.5601

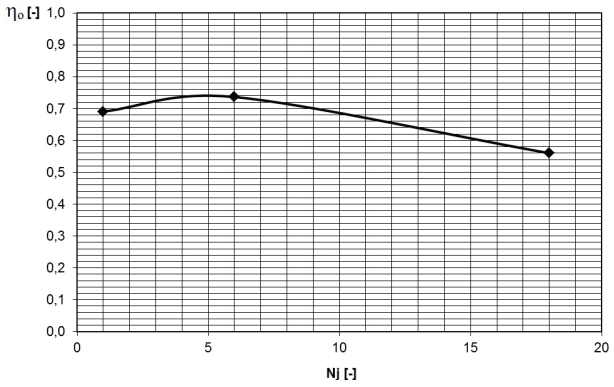

Figure 7: The optimal overall efficiency against the number of ducts

Main results

The best overall efficiency can be reached with six ducts. It is better than the overall efficiency of one-duct type and eighteen-duct type. The expected significant increasing of the overall efficiency was ruined by the increasing transport work demand of the heat transport medium and the increasing heat-loss.

The advantage of the six-duct type against the one-duct type is the smaller inside diameter of a duct D_j. It is easier to distribute the stream of the heat transport medium along a smaller flowing cross-section than along a larger one.

The overall efficiency decreases with increasing of the number of ducts, the main reason of it is the powerful increasing of the transport work demand.

In case of liquid heat transport medium the transport work demand would be much smaller, so better overall efficiency could be reached with greater number of ducts. The upper limit of the overall efficiency would be restricted by the heat-loss.

The void fraction of a packed bed, filled with uniform balls, in case of exact space-filling ε=0.26 is, in practice $\varepsilon \approx 0.3$ is! The void fraction of the volume of the heat store would have to fill with heat transport liquid.

This large liquid volume brings up the idea of the establishment of a heat store with liquid heat storage medium, built from cylindrical tanks, in cascade system formed a spiral flow-path layout. The thermal stratification of the heat store with liquid heat storage material would be sharper, the overall efficiency would be higher than with solid heat storage material.

Conclusions

I have worked out the constructional and the mathematical model of the long flow-way, sensible heat store with cascade system. The temperature-place functions and the overall efficiency can be calculated by using the mathematical model.

I have used genetic optimization algorithm in order to find the optimal variant of the thermal energy store with the best overall efficiency.

The chargeable and the dischargeable heat quantity of the multi-duct, long flow-way heat store is more than of the one-duct, short flow-way thermal energy store with equal mass of solid heat storage material. The temperature level of the outgoing heat transport medium is more advantageous in case of the multi-duct heat store than in case of the one-duct type during the whole charge-discharge cycle.

The heat-loss can be reduced by using heat store with small specific surface and by allowing charge from middle to outside and discharge from outside to middle.

The transport power demand of the heat transport medium can be reduced by making the flow of the transport medium only through the ducts where the thermocline zone is going along.

According to the results of the optimization higher overall efficiency can be reached in case of six-duct type heat store than in case of one-duct type, filled with ceramic balls.

The overall efficiency decreases with increasing of the number of ducts – because of the strong increasing of the transport work demand.

Acknowledgements

This work was supported by the research project TÁMOP-4.1.1.C-12/1/KONV-2012-0017.

REFERENCES

1. P. MUTHUKUMAR: Thermal energy storage systems for solar thermal power plants: Methods and Materials, Indo-Spain joint work on Renewable Energy, Sevilla, Spain (2011), p. 34
2. R. DUNN: *A Global Review of Concentrated Solar Power Storage*, Proceedings of Solar 2010, 48th AuSES Conference, Canberra, Australia (2010), p. 10
3. A. H. ABEDIN, M. A. ROSEN: A critical review of thermochemical energy storage systems, The Open Renewable Energy Journal, 4 (2011), pp. 42–46
4. Y. DEMIREL: Energy production, conversion, storage, conservation, and coupling, Springer (2012), p. 503
5. T. SCHMIDT, D. MANGOLD, H. MÜLLER-STEINHAGEN: Seasonal thermal energy storage in Germany, ISES Solar World Congress, Göteborg (2003), p. 7
6. D. LAING: Thermal energy storage for concentrated solar power: state of the art and current cevelopments, ISES Annual Meeting Tel Aviv University (2011), p. 25
7. D. LAING: Solar thermal energy storage technologies, Energy Forum, 10 000 Solar GW, Hannover (2008), p. 25
8. D. LAING, D. LEHMANN: Concrete storage for solar thermal power plants and industrial process heat, IRES III, 3rd International Renewable Energy Storage Conference, Berlin (2008), p. 6
9. I. ÁRPÁD: Investigation of Sensible Heat Storage and Heat Insulation in the Exploitation of Concentrated Solar Energy, Hungarian Journal of Industrial Chemistry, 39, 2 (2011), pp. 163–167
10. K. RAZNJEVIC: Hőtechnikai táblázatok, Műszaki Könyvkiadó, Budapest (1964), p. 336
11. D. KEARNEY, U. HERRMANN, P. NAVA, B. KELLY, R. MAHONEY, J. PACHECO, R. CABLE, D. BLAKE, H. PRICE, N. POTROVITZA: Overview on use of a Molten Salt HTF in a Trough Solar Field, NREL Parabolic Trough Thermal Energy Storage Workshop Golden, CO, USA (2003), p. 27
12. K. A. R. ISMAIL, R. STUGINSKY JR.: A parametric study on possible fixed bed models for pcm and sensible heat storage, Applied Thermal Engineering, 19 (1999), pp. 757–788
13. G. TÓTH: Számítógépes modellezés, ELTE TTK, Atomfizika Tanszék, egyetemi jegyzet, Budapest (2001), p. 118
14. I. FARAGÓ, R. HORVÁTH: Numerikus módszerek, ELTE TTK – BME TTK egyetemi jegyzet, Budapest (2011), pp. 341–391
15. Verein Deutscher Ingenieure VDI-Gesellschaft Verfahrenstechnik und Chemieingenieurwesen (GVC): VDI Heat Atlas, Second Edition, Springer-Verlag Berlin Heidelberg (2010), pp. 743–744, 1423–1433
16. G. FEJES, G.TARJÁN: Vegyipari gépek és műveletek, Tankönyvkiadó, Budapest (1979), pp. 36–45

HUNGARIAN JOURNAL
OF INDUSTRIAL CHEMISTRY
VESZPRÉM
Vol. 40 (2) pp. 101-105 (2012)

STUDY OF THE PROPERTIES OF A PLAIN CATHODE GRIMM-TYPE DC GLOW DISCHARGE SOURCE OPERATED IN A CURRENT-CONTROLLED PULSE REGIME

O. BÁNHIDI

University of Miskolc, Institute of Chemistry, Miskolc-Egyetemváros, Miskolc, H-3515 HUNGARY
E-mail: akmbo@uni-miskolc.hu

Glow discharge sources have been used for analytical purpose for several years. Recently the pulsed operation mode has gained an increasing importance. Operating the source in current-controlled mode instead of the traditional voltage-feed method may have the advantage of precise control of the source's state and it provides a convenient way to study the relationship among the emitted line intensity and the key parameters of the plasma such as the pressure of the filling gas, the voltage-drop on the source as well as the current flowing through the device. In the following the brief description of the system, the relationship among the voltage drop on the source, the pressure of the filling gas (Ar), the current of the DC pulses as well as the line intensities are presented and discussed.

Keywords: DC glow discharge, pulsed current-controlled mode, atom-spectrometric source.

Introduction

Glow discharge sources have a great importance in the atom spectrometry. Main fields of their application are the analysis of bulk materials and examination of surface layers, i. e. the depth-profile analysis. Besides that they play an important role in the mass-spectrometry an ion-sources. Beside the devices based upon the direct current glow discharge, radio-frequency operated sources have also been developed, making possible the analysis and study of non-conducting materials [1].

In case of the DC sources a substantial part of the power applied to the device will be dissipated as heat in continuous operating mode, warming up both the equipment and the sample being the cathode. To avoid this warming-up, which may also be harmful to some parts of the source either, a suitable cooling system have to be applied. Another way to avoid harmful effect is to operate the device in pulsed mode. Depending on the pulse parameters, the average power applied to the device in the later case is only a few percentages of value necessary on continuous DC mode. Several studies can be found in the literature dealing with sources operated in pulse regime [2, 3, 4].

In the above-mentioned studies the sources are powered exclusively in the so-called voltage-feed way. It means that the device is connected to the DC power supply directly, - or in order to avoid the damage in case of short-circuited condition, - through a so-called ballast resistor. As a consequence of that any change in the state of the source causes a change both on the voltage dropped on the source and that of the current flowing through the device. If because of nay reason the impedance of the source might change , so will change again the voltage drop and the current. This might cause the the source to leave either the area of abnormal mode of operation and will enter the area of normal mode or vice versa. On the other hand it is rather difficult, - though not at all impossible, - to provide precise high-voltage pulses to feed the system in this voltage-fed mode.

So that the change of the voltage drop and the current could be avoidedat and a better control of the system could be achieved, we suggest applying a constant pulse current to the system. By using constant current pulses, the state of the system can also be controlled. To provide constant current pulses, a current generator is needed. It has a very high internal impedance, and because of that the change of the source impedance will not have any effect to the value of the current flowing through the source as long as the current generator is able to provide constant current pulses. In this way the voltage drop and the current will remain unchanged, therefore better control can be achieved.

To study the current-controlled mode we have developed a high power current-generator power supply and controller, which is able to operate in pulsed regime. The pulsed regime operation does not mean that current flows through the source only in the duty-cycle period. In the course of the development it was targeted that the source should always operate in the so-called abnormal region, or at least it should be at the border of the abnormal mode. Therefore there is a low-current period and a high-current one. The later is eventually the duty-cycle period. E.g. at a frequency value of

200 Hz and 10% duty cycle, the length of the period is 5 ms, and the duration time of the high-current lasts 0.5 ms, while the low-current one is 4.5 ms long.

The use of the pulsed regime may provide two advantages. The first one is that high power resulting in dissipating much heat and warming up the equipment is applied just for a very short time, so the average power is just a few percentages of it. This makes unnecessary to apply a cooling system, as much less heat is dissipated by the source. The other advantage is that the short-time high-current pulses the system provides make possible to study and examine thin layers.

Experimental

Main components of the system

Main parts of the system can be seen in *Figure 1*. The light emitted by the discharge is detected and measured by a spedctrometer. The output signal of the detector is processed by a special computer programmed card, USB 4716 manufactured by the Advantech Co.. The electric DC voltage and current pulses necessary for the operation of the discharge is provided by the power supply and current generator unit.

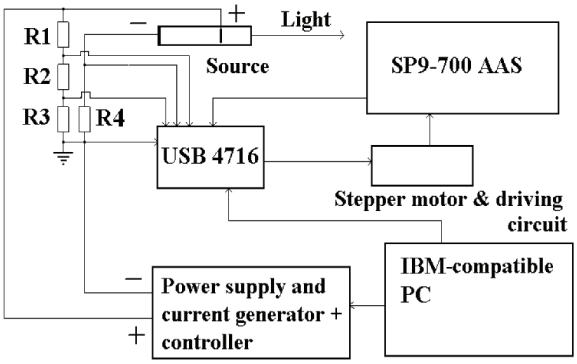

Figure 1: Main components of the system

The source

In the course of the experiemnts a Grimm-type source (presented in *Figure 2*) was used, it is based upon the design made by Wagatsuma and co-workers [5]. The anode is made of brass, its internal diameter is 7 mm.

The power supply and current generator

This unit was designed and built in our laboratory. It is able to provide a DC voltage as high as 1000 V. It can be operated in the frequency range of 122 Hz–5000 Hz. The duty cycle can be chosen between 32 μs – 4.1 ms, resulting values ranging from 0.4% up to 50%, depending on the pulse period and frequency. In the experiments reported here the pulse frequency was

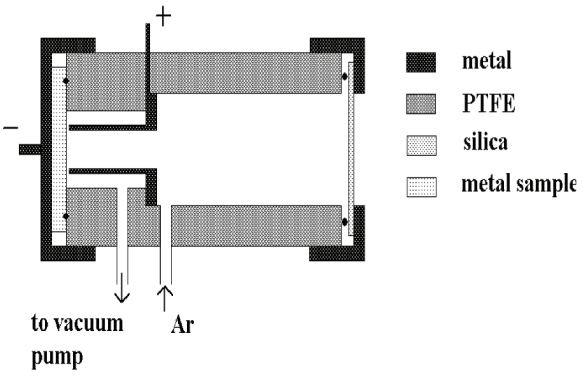

Figure 2: The source used in the experiments.

122 Hz and the duty cycle was 2.3%.

The value of the low current is 1.5 mA, while 5 preadjusted values (32, 72, 115, 135 and 160 mA) can be selected for the high current pulses. The device has its own microcontroller unit, which has a serial (RS 232C) link to the IBM compatible computer controlling the system. This build-up makes possible to choose all the important parameters (value of the frequency, duty cycle and that of the high current) using a special computer programme. The same programme is responsible to controll the measuring system and store the measured data.

The spectrometer

To convert the light of the source into an emission spectrum and to convert the light intensity of the selected spectral line to an electric signal an atomic absorption spectrometer (Pye Unicam SP9-700) was used. Only the spectrometer (monochromator) and the detector (PMT) was used during the experiments. The electric signal processed by the external measuring system was taken from the loading resistor of the photomultiplier tube of the instrument. The narrowest slit width (0.2 nm) was choosen for the experimental work. So that spectras could also be recorded, the device was equipped with a wavelength driving circuitry (consisting of a stepper motor and of a control circuit).

The signal measuring system

The measuring system must be capable to measure signals both in the high-current and in the low-current period. To fulfill this requirement a multifunction module capable to provide fast analogue to digital conversion has been chosen. It is the USB 4716 multifunction module manufactured by Advantech Co Ltd. It has a 16-bit AD converter with a 16-channel

multiplexer and its minimum conversion time is 5 μs. It can operate both in an externally triggered mode and in a so-called software triggered mode. The signal taken from the loading resistor of the photo-multiplier tube (PMT) of the spectrometer is led into the first measuring channel of the device. The electric connection betwen the loading resistor of the PMT and the signal input of the spectrometer own measuring electronic system was eliminated so that these circuits could not have any influence on the measurements.

So that not only the emitted signal of the source, but the current flowing through on that and the voltage drop could be measured, there is a resistor network in the system. R3 is a resistor of 15 Ohm. It is for measuring of the lamp current. Resistors R1 and R2 (20,000,000 and 120,000 Ohms respectively) form a voltage drivider, making possible the measurement of the voltage drop on the source.

The USB 4716 has digital inputs and outputs, therefore it is able to control the stepping motor of the wavelength drive. The unit is controlled by a programme running on an IBM compatible computer.

Other important details of the experiments

In the course of the experiments high purity argon (99,996%) was used as filling gas. A pressure regulator and a vacuum pump made possible to adjust the required value for the pressure of the filling gas. In all the experiments expect for the demonstation of sputtering ability a brass (copper – zinc alloy) probe was applied as the cathode of the source.

Results

As the device operates in pulsed mode, all the signals are eventually pulses. *Figure 3* shows the relative signals of emitted light, discharge current and that of the voltage-drop on the source as the function of time..The different signals are shifted in time so that they could be better observed.

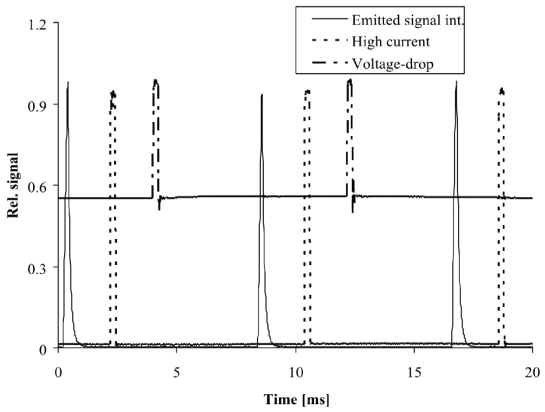

Figure 3: Signals of the emitted light, current and voltage-drop pulses as the function of time

Stability of the current generator

From the view-point of the operation it is important to know how much the changes in the pressure of the filling gas affect the value of the high current, in other words how stable the current generator is. As it can be seen in *Figure 4*, the value of the high current is eventually not affected in the pressure range of 300–950 Pa, but under 300 Pa it is no longer constant, i.e. under the above-written range the current generatror no longer works.

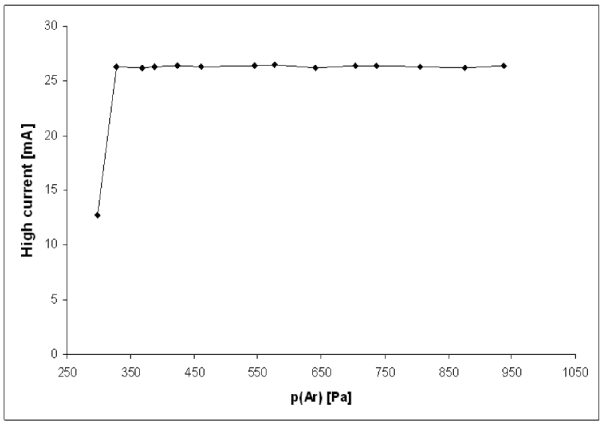

Figure 4: The high-current pulses as the function of the filling gas pressure

The relation among the voltage-drop, the current and that of the filling gas pressure

As the device operates in the abnormal working range, it can be expected that the voltage-drop on the source will increase with increasing current. The relation measured is presented in *Figure 5,* where the voltage-drop on the source can be seen as the function of the current at three argon pressure values. It can be stated that according to the expectations the voltage-drop is greater at higher current, but the increasement is higher at lower argon pressure.

The relation of the voltage-drop to the filling gas pressure measured at 72 mA high current is shown in *Figure 6*. It can be observed that there is only a moderate increasement in the voltage-drop with decreasing argon pressure in the range of 400–900 Pa, while the voltage-drop increases sharply below that range.

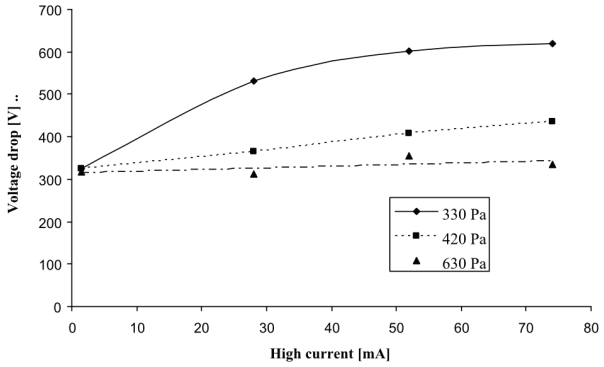

Figure 5: The voltage-drop as the function of the current at 3 different filling gas pressure.

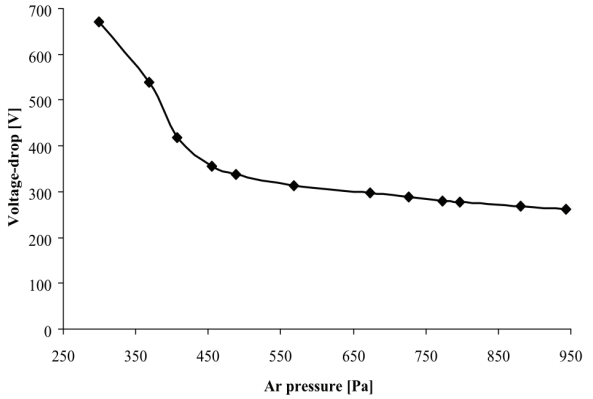

Figure 6: The voltage-drop as the function of the filling gas pressure at 72 mA.

The light intensity emitted by the cathode material

From the viewpoint of the possible practical analytical application the emission by the elements building up the cathode sample has the greatest importance. This emission, i. e. the intensity of the emitted light is also the function of the current and the pressure of the filling gas. In the course of the experiments the emission on the strongest atomic line of Cu (324.8 nm) was measured. The results are presented in *Figure 7* and *Figure 8*. Looking at these figures it can be stated that the emitted line intensity sharply increases with increasing pulse current and decreases with increasing filling gas pressure.

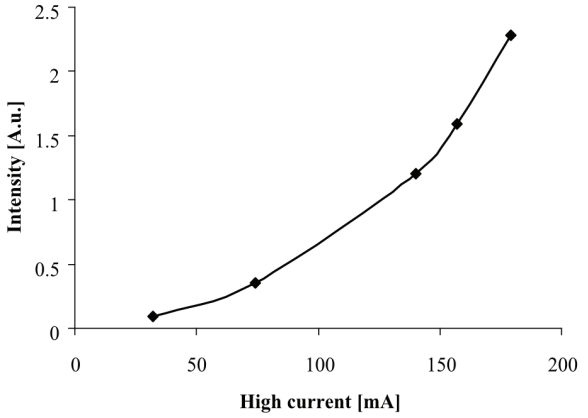

Figure 7: The emitted light intensity measured on the 324.8 nm Cu I. line as the function of the current at 350 Pa.

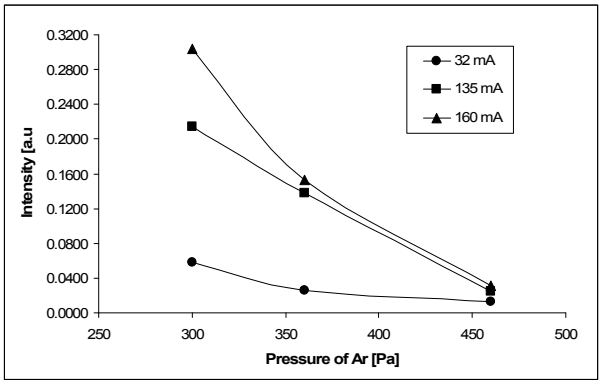

Figure 8: The emitted light intensity measured on the 324.8 nm Cu I. line as the function of the pressure of the filling gas.

The sputtering ability

The atoms of the bulk cathode material can get to the plasma by the mean of sputtering, so this process has a key-importance in the proper operation of the source. Beside that it makes possible the depths profile analysis. In order to get information on the sputtering efficiency the sputtering speed has to be determined, which will be performed in the future. In these experiments only the demonstration of the sputtering ability is presented.

As this source is operated in pulse mode, high power is applied to the source just a few percentages of the pulse duration, therefore rather low sputtering speed can be expected if it is averaged for the whole period. On the other hand it might advantageous in case of thin layers.

To present the sputtering ability a steel plate, which had a 2,0 ± 0,2 µm thick zinc coating on its surface was taken as cathode sample and the zinc emission was measured on the 213.85 nm Zn I line at 350 Pa argon pressure as the function of time. The value of the high current was 72 mA, the pulse frequency was 122 Hz and the duty cycle was 2.3%. The measured data are presented in *Figure 9*. It can be observed that after 3000 s time interval, no zinc emission can be measured.

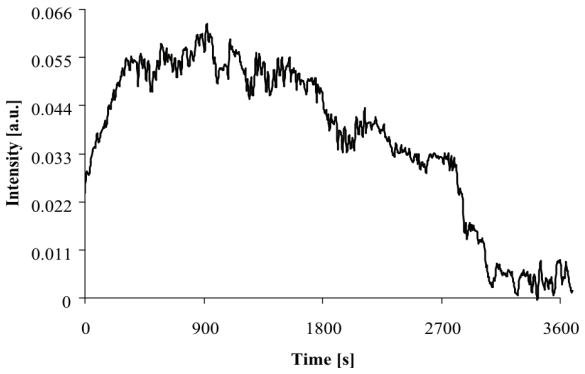

Figure 9: The line intensity measure on the 213.85 nm Zn I. line as the function of time.

Discussion of the results

In the experiments a DC glow discharge source was studied, which was operated in pulse regime, at constant high and low current values. It could be seen that the current generator can be used in a wide range of Ar pressure and the constant current makes possible an easier control of the device. From the viewpoint of the operation of the device the voltage-drop has a key importance, namely as long as it does not exceed the capabilities of the current generator, the constant current mode works. When the current generator runs out of the voltage, it stops working, therefore care must always be taken of the voltage-drop, and careful examination is needed to reveal the relation among the high current, the voltage-drop and that of the filling gas pressure. In *Figure 6* it can be seen that at 72 mA the source can be used in current regulated mode at the range of 300–950 Pa. Below 300 Pa the voltage-drop sharply increases with decreasing pressure, so it probably will not work at pressure values lower than 260–270 Pa.

In *Figure 5* the relationship between the voltage-drop and that of the current is shown. It must be noticed that the first point in the figure is the voltage-drop at the low current value. This also suggests that the device operates in the abnormal operating region within the whole current range.

The emission data measured on the 324.8 nm Cu I line are presented in *Figure 7* and *Figure 8*. It is worth mentioning that the emitted light intensity sharply increases with increasing current, it seems to be an exponential function rather than a linear one. The reason for that sharp increasement may be the better sputtering efficiency. On the other hand, the emitted light intensity decreases with increasing filling gas pressure. In *Figure 9* the sputtering ability is demonstrated. It took about 3000 s to eliminate the 2 μm thick Zn layer. If the duty cycle (2.3%) is taken into account, this would mean a sputtering speed of 1.74 μm /minute at continuous DC current. It must be mentioned that the duty cycle the speed depends also on the current and that of the argon pressure beside the duty cycle of the pulses.

It also could be seen that the behaviour of the source is similar to the ones operated in voltage-feed mode, except for the fact that its state can always be charactised precisely bevause of the constant-current mode.

Acknowledgement

The described work was carried out as part of the TÁMOP-4.2.1.B-10/2/KONV-2010-0001 project in the framework of the New Hungarian Development Plan. The realization of this project is supported by the European Union, co-financed by the European Social Fund.

REFERENCES

1. A. BOAGERTS, E. NEXTS, R. GIJBELS, J. VAN DER MULLEN: Gas Discharge Plasmas and their Applicaion, Spectrochimica Acta Part B, 57 (2002), pp. 609–658
2. CH. YOUNG, K. INGENERI, W. W. HARRISON: A Pulsed Grimm Glow Discharge as an Atomic Emission Source, Journal of Analytical Atomic Spectrometry, 14 (1999), pp. 693–698
3. L. N. MISHRA, K. SHIBATA, H. ITO, N. YUGAMI, Y. NISHIDA: Charatcterization of Pulsed Discharge Plasma at Atmospheric Pressure, Surface & Coating Technology, 201 (2007), pp. 6101–6104
4. CH. YOUNG. W. W. HARRISON: Investigation of a Novel Hollow Cathode Configuration for Grimm-type Glow Discharge Emission, Spectrochimica Acta, Part B, 56 (2001), pp. 1195–1208
5. K. WAGATSUMA, K. HIROKAWA: Observation of Cu-Ni alloy Surfaces by Low Wattage Glow Discharge Emission Spectrometry, Surface and Interface Analysis, 6 (1984), pp. 167–170

HUNGARIAN JOURNAL
OF INDUSTRIAL CHEMISTRY
VESZPRÉM
Vol. 40 (2) pp. 107–111 (2012)

EFFECTS OF PAN BREAD MAKING ON ZEARALENONE LEVELS IN ARTIFICIAL CONTAMINATED WHEAT FLOUR

T.A. EL-DESOUKY✉, M. MAY AMER, K. NAGUIB

Food Toxicology & Contaminants Dept. National Research Center, Dokki, Cairo, EGYPT
✉E-mail: eldesoukyt@yahoo.com

The ability of *Saccharomyces cerevisiae* (Baker's yeast) in reduces of zearalenone during fermenting dough at 25°C and 30°C for 30 and 45 min was studied. The results indicate that content of zearalenone was reduced to 9.44, 19.22, 37.6 and 63.16µg/kg in dough made from flour artificially contaminated with 25, 50, 75 and 100 µg/kg, respectively when the fermentation process at 25°C for 45 min. On the other hand, during fermentation at 30°C the decrease in the content of zearalenone is greater than ever, particularly with increasing duration or time of fermentation to 45 min. The content of zearalenone after fermentation at 30°C for 45 min was 7.52, 17.14, 34.19 and 60.38µg/kg in dough made from flour artificially contaminated with 25, 50, 75 and 100µg/kg, respectively. The reduction percentage of zearalenone after baking pan bread at 180°C for 25 min was 55.98, 62.78, 62.5 and 60.52%.These results indicate that fermentation and baking are effective in reducing zearalenone.

Key words: Zearalenone, *Saccharomyces cerevisiae*, fermentation and baking

Introduction

Zearalenone (ZEA) is a mycotoxin mainly produced by *Fusarium graminearum* and *Fusarium culmorum*, which are common soil fungi in temperate and warm countries, and are regular contaminants of cereal crops worldwide [1, 2]. ZEA is mainly with corn and wheat but it occurs also in barley and sorghum amongst other commodities frequently used in human and animal diets. The International Agency for Research on Cancer (IARC) has categorized ZEA as a class 2A carcinogen [3]. ZEA produces estrogenic effects in humans and animals leading hyperestrogenism. Hyperestrogenism may be manifested enlargement of the reproductive organs. ZEA can cause severe reproductive and infertility problems in farm animals, particularly in swine [4]. Specifically, ZEA can act as an estrogen analog and cause alterations in the uterus of the reproductive tract of swine and affect follicular and embryo development [5]. The function of ZEA as an estrogen analog is important because swine are monogastric animals with responses similar to humans in many respects [6]. Even though most African countries have a climate characterized by high humidity and high temperature which favor growth of moulds, little information is available on the occurrence of *Fusarium* toxins particularly ZEA in foods and feeds. High contaminations of the raw materials are an ongoing problem. Regulatory issues are not available in the field of food exhibition and retailing, and mycotoxin problems have already been associated with some food contamination in some areas in Africa [2]. In Egypt, several commodities were reported to contain ZEA especially corn, wheat and rice and walnut [7, 8]. Corn from Egypt was also found contaminated with high levels of ZEA that ranged from 9.8 to 38.4 mg/kg [9]. According to FAO [10], ZEA was regulated in 1996 by 6 countries, but by the year 2003 the toxin ZEA was regulated in foods and animal feeds by 16 countries. Limits for ZEA in maize and other cereals, currently vary from 50 to 1000 µg/kg. Although various prevention strategies have been implemented in many countries, they were not enough to manage the problem efficiently in the developing world. In the recent years, many dietary strategies involving microorganisms have been under investigation. Many species of bacteria and fungi have been shown to enzymatically degrade mycotoxins [11]. However, the question still remains on the toxicity of the degradation products. *Saccharomyces cerevisiae* has been utilized in food fermentation for several centuries. In the African and Asian countries, fermentation is used as a predominant mode of food processing and preservation. Many yeast species, especially *Saccharomyces cerevisiae*, play a predominant role in food fermentation along with lactic acid bacteria [12]. In the African fermented foods such as fermented maize dough (Kenkey) as well as sorghum beer (Pito), *Saccharomyces cerevisiae* constitutes a predominant component of fermentation microflora and the biodiversity of yeast microflora in these foods has been well documented [13]. Mycotoxin binding by *Saccharomyces cerevisiae* and lactic acid bacteria have been reviewed recently [14]. The aim of this work was to study the ability of *Saccharomyces cerevisiae* in reduce of ZEA during fermenting dough at 25°C and 30°C for 30 and 45 min, also study effect of baking Pan bread at 180°C on content of ZEA.

Materials and method:

Materials

Wheat flours (72% extraction) were obtained from the North Cairo Mills Company, Egypt. *Saccharomyces cerevisiae* (Baker's yeast) was obtained from Al-Hawamdia Company fresh comprised yeast according to the Egyptian standard (191/2005).

Methods

Preparation of artificial contaminated wheat flour

One milligram of ZEA was purchased from Sigma, chemical Co. (St. Louis, MO, U.S.A). ZEA was dissolved in 1 ml methanol. Then taken appropriate size of focus and complemented the larger size makes it easier to control added to wheat flour. Four wheat flour samples (1kg each) were aged in various concentrations (25, 50, 75 and 100µg/kg). Each of the contaminated wheat flour samples was used for preparation of Pan Bread. This mixture was stirred until the solvent had evaporated.

Pan bread making

Pan bread was prepared by mixing 100g of wheat flour (72% extraction) with 5 g of Baker's yeast, 1.5 g of sodium chloride and 75–80 ml of water and hand blended for about 6 min to form the dough. The dough was lift to rest for 30 min at 25°C & 30°C and 85% relative humidity and was then divided into 150g pieces. The pieces were booted in metal pans that had been left to ferment for about 45 min at the same temperatures and relative humidity according to AACC [15]. And then were baked at 180°C for 25 min the resulted pan bread was allowed to cool at room temperature for 2 h before being packed in polyethylene bags and stored at room temperature for determination of ZEA.

Extraction procedure

Twenty grams of sample was weighted into a 250mL blender jar with 2 g NaCl and extracted with 50mL of extraction solution (acetonitrile: water 90:10 v/v). The mixture was blended for 2 min and centrifuged for 3 min at 3,000 rpm.

The extract was filtered through filter paper (Whatman No.1). 10 ml filtrate was mixed with 40 ml water, followed by filtration through a glass microfibre filter.

Immunoaffinity Clean-up

Ten milliliter of filtrate was passed through Zeara-latest™ immunoaffinity columns at about 1-2 drops/s. 10ml water was used to wash the loaded immunoaffinity column at a steady flow rate. ZEA was eluted with 1 ml of methanol. The methanol elute was filtered through a 0.45µm micro filter and collected in a clean vial for the following HPLC.

HPLC/fluorescence Analysis

The HPLC system consisted of Waters Binary Pump Model 1525, a Model Waters 1500 Rheodyne manual injector, a Watres 2475 Multi- Wavelength Fluorescence Detector. The fluorescence detector was operated at wavelength of 274 nm for excision and 440 nm for emission, and a data workstation with software Breeze 2. A phenomenex C_{18} (250 X 4.6 mm i.d.), 5 µm from waters corporation (USA). The mobile phase consisted of a mixture of acetonitrile: water: methanol (48:50:3, v/v/v). A 20 µl of the reconstituted extract was injected onto the column at a flow rate of 1.0 ml/min. ZEA content in samples was calculated from chromatographic peak areas using the standard curve.

Statistical analysis

The statistical analysis was performed using the SPSS software program (SPSS Institute, 2011, version 19.0) and the differences in ZEN concentrations between time and temperatures dough fermentation were analyzed by ANOVA test. $P \leq 0.05$ was considered to be statistically significant.

Results and discussion

Influence of manufacture process of Pan Bread on content of ZEA:

Effect of dough fermentation

The effect of using *Saccharomyces cerevisiae* (Baker's yeast)on content of ZEA during fermentation of artificially contaminated wheat flour dough at 25°C and 30°C for 30 and 45 min was presented in *Table 1 and 2*. The content of ZEA was reduced to 13.71, 24.18, 43.88 and 71.43µg/kg in dough made from flour artificially contaminated with 25, 50, 75 and 100 µg/kg, respectively when the fermentation process at 25°C for 30 min. While decreased the content of ZEA more with more time fermenting dough to 45 min. On the other hand, during fermentation at 30°C the decrease in the content of ZEA is greater than ever, particularly with increasing duration or time of fermentation to 45 min. The content of ZEA after fermentation at 30°C for 45 min was 7.52, 17.14, 34.19 and 60.38µg/kg in dough made from flour artificially contaminated with 25, 50, 75 and 100µg/kg, respectively.

Low incubation temperature (25°C) during the growth of the cells seems to adversely affect the binding and the optimal and above-optimal growth temperature did not affect the binding. Temperature is known to affect the cell wall composition with lower temperature resulting in reduced cell growth, cell wall dry mass, mannan and β-glucan levels [16]. Culture conditions including pH, temperature, oxygenation rate, nature of the medium, and concentration or nature of the carbon

source strongly modulate the quantity and structural properties of β-D-glucans, mannans and chitin in cell walls. Moreover, the cell cycle stage also interacts with the cell wall composition. For example, budding induces strong changes in the distribution of the structural components of the cell wall such as chitin. Changes in the cell wall components at low growth temperatures might have resulted in reduced binding molecules on the cell surface.

Cell wall of *Saccharomyces cerevisiae* consists of network of β-1,3 glucan back bone with β-1,6 glucan side chains, which is in turn attached to highly glycosylated mannoproteins which make the external layer [17].

The proteins and glucans provide numerous easily accessible binding sites with different binding mechanisms such as hydrogen bonding, ionic or hydrophobic interactions [18]. Binding of different mycotoxins such as aflatoxin, ochratoxin and ZEA to yeast cell surface has been reported earlier and the binding has been attributed to cell wall glucans in case of ochratoxin and ZEA [19]. β-D-glucans are the yeast component responsible for the complexation of ZEA, and that the reticular organization of β-D-glucans and the distribution between β-(1, 3)-D-glucans and β-(1, 6)-D-glucans play a major role in the efficacy and add at weak hydrogen and van der Waals bonds are involved in the chemical complex formation between ZEN and β-D-glucans. Thus, the chemical interaction is more of "adsorption type" than "binding type". Molecular modeling was performed to validate the concept on other mycotoxins such as aflatoxin B_1, deoxynivalenol and patulin [20].

The reduction percentage of ZEA after fermentation dough at 30°C for 30 min was only 58.8, 55.1, 46.98 and 34.42%, while it was 69.9, 65.72, 54.41 and 39.62% after fermentation dough for 45 min from flour artificially contaminated with 25, 50, 75 and 100µg/g, respectively. The percentage of ZEA reduction increased with time of fermentation dough shown in *(Figure 1)*. There was observed relationship between the degree of reduction and the initial level of ZEA contamination during fermentation dough . And, as it was expected, a positive relationship was observed between the increase of fermentation time and that of the percentage of reduction on ZEA-contaminated wheat flour

Table 1: Concentrations of ZEA determine in artificially contaminated wheat flour after dough fermentation at 25°C (n=3)

Time of fermentation dough (min)	Spiking level of ZEA (µg/kg)			
	25	50	75	100
After mixed directly	23.26 ±0.34	46.98 ±0.4	73.71 ±0.12	96.45 ±0.17
30	13.71 ±0.46	24.18 ±0.25	43.88 ±0.52	71.43 ±0.39
45	9.44 ±0.18	19.22 ±0.44	37.6 ±0.41	63.16 ±0.51

Table 2: Concentrations of ZEA determine in artificially contaminated wheat flour after dough fermentation at 30°C (n=3)

Time of fermentation dough(min)	Spiking level of ZEA (µg/kg)			
	25	50	75	100
After mixed directly	23.26 ±0.34	46.98± 0.4	73.71 ±0.12	96.45± 0.17
30	10.3 ±0.26	22.45± 0.28	39.76 ±0.71	65.58± 0.73
45	7.52 ±0.1	17.14± 0.19	34.19 ±0.38	60.38± 0.92

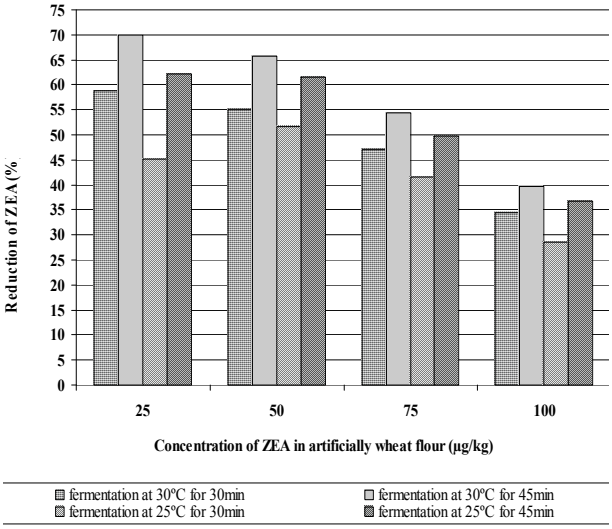

Figure 1: The percentages of ZEA reduction during fermented dough

Effect of baking

ZEA concentration as affected by baking of artificially contaminated flour dough during Pan bread making is shown in *Table 3* and *Figure 2*. The residual amount of ZEA was 3.31, 6.38, 12.82 and 23.84µg/kg after baking dough artificially contaminated with different concentration of ZEA i,e 25, 50,75 and 100µg/g, respectively. The reduction percentage of ZEA after baking pan bread at 180°C for 25 min was 55.98, 62.78, 62.5 and 60.52%.The results showed a positive correlation between the initial contamination level and the reduction of ZEA after baking. The levels of ZEA in cereal-based foods were reduced significantly by extrusion processing, and reduction of 83% of ZEA in corn-based foods was obtained with this process [21]. However, there remains a need to demonstrate that the toxicity or biological activity of ZEA has been reduced or completely eliminated in cereal-based foods using extrusion processing [22]. *Figure 3a* showed the HPLC chromatogram of ZEA standard where *Fig. 3b* showed the sample with zearalenone level of 25µg/kg after fermentation at 30 °C for 30 min. while *Fig. 3c* HPLC chromatogram of zearalenone in sample pan bread.

Table 3: Concentrations of ZEA in Pan Bread after baking at 180 °C for 25 min. (n=3)

Treatment	Spiking level of ZEA (µg/kg)			
	25	50	75	100
Fermentation dough at 30°C for 45 min	7.52 ±0.1	17.14 ±0.19	34.19 ±0.38	60.38 ±0.92
Baking at 180 °C for 25 min	3.3.1 ±0.15	6.38 ±0.29	12.82 ±0.76	23.84 ±1.6
Reduction (%)	55.98	62.78	62.5	60.52

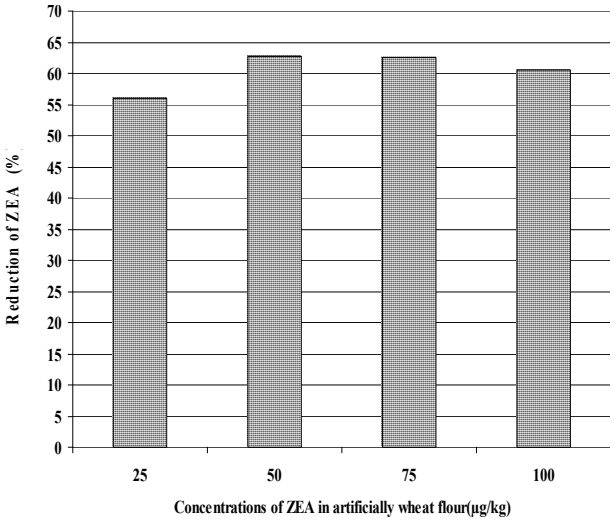

Figure 2: Effect of baking at 180 °C for 25 min on content of ZEA in dough after fermentation at 30°C for 45 min

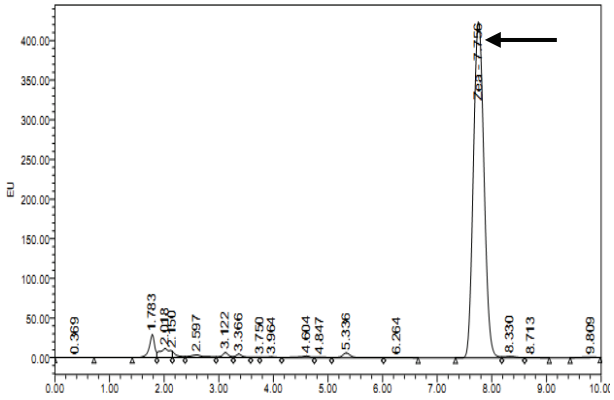

Figure 3 a: HPLC chromatogram of zearalenone standard

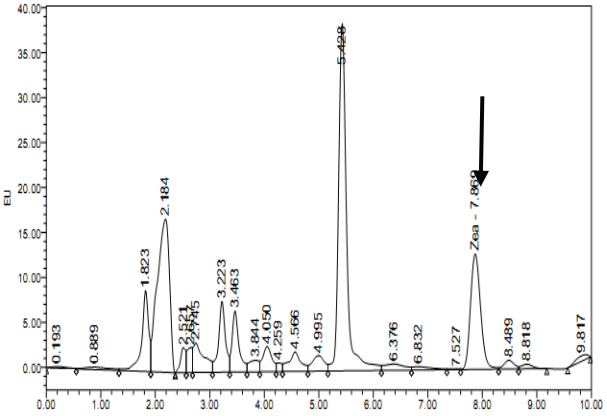

Figure 3 b: HPLC chromatogram of sample with 30°C for 45min

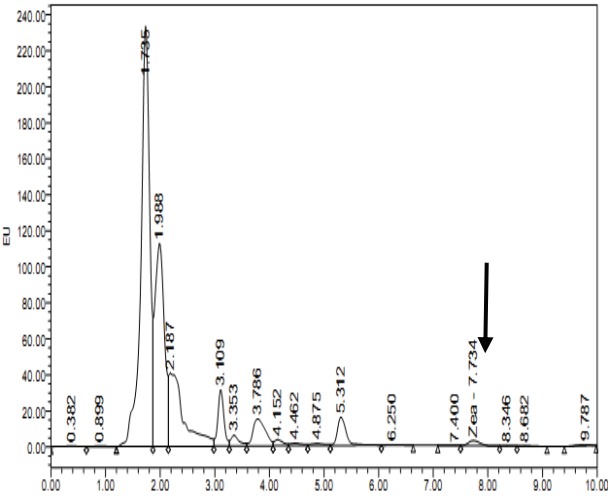

Figure 3c: HPLC chromatogram of zearalenone in sample pan bread

Conclusion

It could be concluded that the fermentation of dough at 30°C for 45 min was best into reduce the content of ZEA, Because this could be a good growth of yeast cells in the dough and is doing and its perfect. So attention must be paid to the process of fermentation and conditions of particular temperature that would influence the activity of yeast cells used. It also shows the importance of yeast cells to reduce the levels of ZEA**.** Also the results of the study show that the residual of the ZEA in the bread was within allowable limits internationally.

REFERENCES

1. J. P. F. D'MELLO, C. M .PLACINTA, A. M. C. MACDONALD: Fusarium mycotoxins: a review of global implications for animal health, welfare and productivity, Anim Feed Sci Technol., 80 (1999), pp. 183–205
2. A. ZINEDINEA, J. M .SORIANOB, J. C. MOLTO, J. MANES: review on the toxicity, occurrence,

metabolism, detoxification, regulations and intake of zearalenone: an oestrogenic mycotoxin, Food Chem Toxicol., 45 (2007), pp. 1–18

3. INTERNATIONAL AGENCY FOR RESEARCH ON CANCER (IARC): In. IARC monographs on the evaluation of carcinogenic risks to humans: Heterocyclic amines and mycotoxins, 56 (1993), pp. 397
4. COUNCIL FOR AGRICULTURAL SCIENCE AND TECHNOLOGY (CAST): Task force report, 139, Council for Agricultural Science and Technology (2003)
5. U. TIEMANN, S. DANICKE: In vivo and in vitro effects of the mycotoxins zearalenone and deoxynivalenol on different non-reproductive and reproductive organs in female pigs: a review, Food Additives and Contaminants, 24 (3) (2007) 306–314
6. H. TAKEMURA, J. Y.SHIM, K. SAYAMA, A. TSUBURA, B. T. ZHU, K. SHIMOI: Characterization of the estrogenic activities of zearalenone and zeranol in vivo and in vitro. Journal of Steroid Biochemistry and Molecular Biology, 103 (2007), pp. 170–177
7. E. S. ABD ALLA: Zearalenone: toxigenic fungi and chemical decontamination in Egyptian cereals, Nahrung, 41 (1997), pp. 362–365
8. A. I. ABDEL-HAFEZ, S. M. SABER: Mycoflora and mycotoxin ofhazelnut (Corylus avellana L.) and walnut (Juglans regia L.) seeds in Egypt, Zentralbl Mikrobiol., 148 (1993), pp. 137–147
9. O. M. EL-MAGHRABY, I. A. EL-KADY, S. SOLIMAN: Mycoflora and *Fusarium* toxins of three types of corn grains in Egypt with special reference to production of trichothecene-toxins, Microbiol. Res., 150 (1995), pp. 225–232
10. FAO: Worldwide regulations for mycotoxins in food and feed in 2003, FAO Food and Nutrition paper, 81, Food and Agriculture Organization of the United Nations, Rome, Italy
11. A. BATA, R. LASZTITY: Detoxification of mycotoxin contaminated food and feed by microorganisms, Trends in Food Science and Technology, 10 (1999), pp. 223–228
12. L. JESPERSEN: Occurrence and taxonomic characteristics of strains of *Saccharomyces cerevisiae* predominant in African indigenous fermented foods and beverages, FEMS Yeast Research, 3 (2003), pp. 191–200
13. R. L. K. GLOVER, R.C. ABAIDOO, M. JAKOBSEN, L. JESPERSEN: Biodiversity of *Saccharomyces cerevisiae* isolated from a survey of pito production sites in various parts of Ghana, Systematic and Applied Microbiology, 28 (2005), pp. 755–761
14. P. H. SHETTY, L. JESPERSEN: *Saccharomyces cerevisiae* and lactic acid bacteria as potential mycotoxin decontaminating agents. Trends in Food Science and Technology, 17 (2006), pp. 48–55.
15. AACC: Approved Method of the American Association of Cereal Chemists, 11th ed (2005), INC. St. PaulMinnesota, USA
16. B. AGUILAR-USCANGA, J. M. FRANCOIS: A study of the yeast cell wall composition and structure in response to growth conditions and mode of cultivation, Letters in Applied Microbiology, 37 (2003), pp. 268–274
17. R. KOLLAR, B. B. REINHOLD, E. PETRAKOVA, H. J, YEH, G. ASHWELL, J. DRGONOVA, J. C. KAPTEYN, F. M. KLIS, E. CABIB: Architecture of the yeast cell wall Beta 1,6-glucan interconnects mannoprotein, beta 1,3-glucan, and chitin Journal of Biological Chemistry, 272 (1997), pp. 17762–17775.
18. A. HUWIG, S. FREIMUND, O. KAPPELI, H. DUTLER: Mycotoxin detoxication of animal feed by different adsorbents, Toxicology Letters, 122 (2001), pp. 179–188
19. A. YIANNIKOURIS, J. FRANÇOIS, L. POUGHON, C. G. DUSSAP, G. BERTIN, G. JEMINET, J. P. JOUANY: Adsorption of zearalenone by b-D-glucans in the *Saccharomyces cerevisiae* cell wall, J. Food Prot. 67 (2004), pp. 1195–1200
20. J. P. JOUANY, A. YIANNIKOURIS, G. BERTIN: The chemical bonds between mycotoxins and cell wall components of Saccharomyces cerevisiae have been identified Archiva Zootechnica, 8 (2005), pp. 26–50
21. D. RYU, M. A. HANNA, L. B. BULLERMAN: Stability of zearalenone during extrusion of corn grins, J. Food. Prot, 62 (1999), pp. 1482–1484
22. Y. CETIN, L.B. BULLERMAN: Evaluation of reduced toxicity of zearalenone by extrusion processing as measured by the MTT cell proliferation assay, J. Agric. Food Chem., 16 (2005), pp. 6558–6563

HUNGARIAN JOURNAL
OF INDUSTRY AND CHEMISTRY
VESZPRÉM
Vol. 40 (2) pp. 113-119 (2012)

MAGNETORHEOLOGICAL FLUID BRAKE – BASIC PERFORMANCES TESTING WITH MAGNETIC FIELD EFFICIENCY IMPROVEMENT PROPOSAL

A. POZNIĆ[1]✉, A. ZELIĆ[1], L. SZABÓ[2]

[1]University of Novi Sad, 6 Trg Dositeja Obradovića, 21 000 Novi Sad, SERBIA
✉E-mail: alpoznic@uns.ac.rs
[2]University of Pannonia, 18 Zrínyi Str., 8800 Nagykanizsa, HUNGARY

A review of all magnetorheological brake types was presented. Based on overall braking torque analytical comparison for all magnetorheological brake types and other relevant parameters, the most promising design was selected. A test rig, utilizing selected brake type filled with magnetorheological fluid – Basonetic 5030 was manufactured and then tested. To analyze the effect produced by magnetic field on magnetorheological fluid and hence at overall braking torque, the authors used amplification factor. Results were discussed and the magnetic field efficiency improvements were proposed.

Keywords: magnetorheological brake, Basonetic 5030, test rig, amplification factor, efficiency improvements

Introduction

The convectional friction brake (FB) is the most commonly used brake type in almost any mechanical system today. However, it is characterized by drawbacks such as periodic replacement due to wear, large mechanical time-delay, bulky size etc. [13, 29], partially altered. Electromechanical brakes (EMBs) have potential to overcome some of these drawbacks and are a suitable FB replacement. Today EMBs are applicable in almost any mechanical system. Application of intelligent materials is the next step in the development of EMB.

Magnetorheological (MR) fluids belong to a class of intelligent materials that respond to applied magnetic field with fast, continuous, and reversible change in its rheological behaviour [3, 7, 28], partially altered. MR fluids are a type of suspensions, with carrier fluid usually mineral or synthetic oil, water, kerosene and micro size magnetizable particles dispersed in it. When exposed to external magnetic field particles form a chain-like structures thus changing the viscosity of the fluid. In this study, authors used BASF's magnetorheological fluid, Basonetic 5030.

MR fluids have attracted extensive research interest in recent years since they can provide simple, quiet and fast response interface between electronic control and mechanical system [11, 20, 22]. A lot of work was done on MR fluid brakes modelling, properties investigation and control [3, 6, 11]. A wide range of MR fluid devices have also been investigated for their potential applications in different systems, such as: clutch system, vibration control, seismic response reduction, etc. [9, 10, 26].

MR fluid brakes have also been used in actuators due to their distinguished force control and power transmission features [5, 15]. By applying a proper control effort, viscosity with large varying range is achievable with the MR fluid brake. Currently, there are many solutions for MR fluid brake design. Some MR fluid brakes with attractive properties, such as high yield stress and stable behavior, have been developed and commercialized [4, 16].

The objective of this work was to compare overall braking torque analytical expressions and design complexity for all MR fluid brake types. Based on results obtained from these comparisons, MR fluid brake type with the most promising properties was manufactured and tested on a specially designed test rig. Results were discussed and a proposal for new MR brake design with higher magnetic efficiency was presented.

Magnetorheological effect

MR fluids are suspensions composed out of three major components: carrier fluid - usually mineral or synthetic oil, magnetizable particles - carbonyl iron powder and set of additives [2, 17], partially altered. When exposed to an external magnetic field (ON state), change in MR fluid's viscosity occurs. In the absence of an external magnetic field (OFF state), MR fluid acts as Newtonian fluid [7, 11] and can be described as:

$$\tau = \eta \cdot \dot{\gamma} \tag{1}$$

In (1) τ represents shear stress, η the viscosity of the fluid and $\dot{\gamma}$ shear rate. Often, for MR fluid brakes,

denoted as $\dot{\gamma} = r \cdot \omega / g$, where r is rotor radius, ω and g are angular speed and MR fluid gap length, respectively.

When in ON state, MR the rheological properties of MR fluid change. Magnetizable particles induce polarization and form chain-like structures in magnetic flux path direction, thus changing apparent viscosity of the fluid. ON state behavior of MR fluid is often represented as a non-Newtonian [1, 3, 5], having a variable yield strength. The usage of Bingham's model (2), in this situation, gives reasonably good results, [1, 11, 20, 22]:

$$\tau = \tau_{\mathrm{B}} + \eta \cdot \dot{\gamma}\,, \tag{2}$$

where τ_B is the yield stress, developed in response to the applied magnetic field. Its value is a function of the magnetic field induction B.

When used in a device, MR fluid can be in one of four modes: shear, flow (pressure), squeeze and pinch, [8, 18, 28]. In brake i.e. torque transfer applications, MR fluid operates in shear mode [1]. Braking torque values are adjusted continuously by changing the external magnetic field strength.

Magnetorheological brakes

MR brake consists out of four main parts: rotor, housing i.e. stator, coil and MR fluid, *Figure 1*. The shape of the rotor is what differentiates MR brake types from each other. One needs the quantitative parameters of MR brake, to be able to determine its specific application suitability.

MR brake types, mechanical model, quantitative parameters comparison for all MR brake types are presented in next section.

Magnetorheological brake types

Through literature research [9, 14, 22, 23, 24], authors of this paper have identified five major MR fluid brake designs: drum brake, inverted drum brake, disk brake, T-shape rotor brake and multiple disks brake, *Fig. 1*.

Drum brake along with the disk brake is the easiest designs to manufacture. However, large inertia is its major drawback compared to disk brake design [1].

The disk brake design is the most common MR brake design found in literature today and was the first one to be investigated [25]. It is the easiest one to manufacture and gives reasonably good results in terms of weight and compactness [14]. There are some variations in MR disk brake design such as: the use of two coils instead of one in order to increase the magnetic pole area and/or relocation of the coil on top of the disk in order to reduce its external diameter [22], but the basics remain the same. It is also interesting to note that the MR disk brake design is currently the only one commercially available as a standard product, manufactured by Lord Corporation [16] and that it was used in several studies [7, 19, 21].

In order to increase compactness of the MR disk brake design, several disk-shape rotors can be used instead of one, with segments of stator located in between each rotor disk, *Fig. 1.d*. This multiple disk design is very popular in literature and was used in several applications that required high torque in limited space and weight [13, 22, 23]. The equations describing this particular design are very similar to those of the single disk brake, presented paper's sequel.

The T-shape rotor brake design *(Fig. 1.e)*, is more compact than all other designs but is also more complex to manufacture. Despite its advantages, this design is not so common in literature [22].

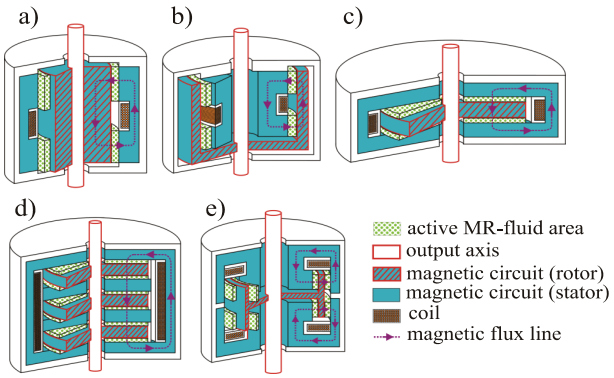

Figure 1: Types of MR brakes: a) drum, b) inverted drum, c) disk, d) multiple disks, e) T-shaped rotor, [28]

For all aforementioned MR brake types, the rotor has a cylindrical shape and the magnetic flux lines run in the radial direction, *Fig. 1*.

To author's knowledge, an in-depth comparison of all these architectures is not yet available.

Mechanical model

The key objective in MR fluid brake design is to establish the relationship between the overall braking torque, magnetic field strength and design parameters. Interaction of MR fluid and inner surfaces of the brake will generate the braking torque. Based on *Eq. (2)* and the specific geometrical configuration of MR brake, for all MR brake types, it applies:

$$\mathrm{d}T = 2\pi N \tau r^2 \mathrm{d}r\,, \tag{3}$$

where:

N – number of surfaces of the rotor, perpendicular to the magnetic flux lines and in contact with MR fluid,

r – the radius of the rotor.

The overall braking torque $T_{Overall}$, consists of three components:

- the magnetic field induced component T_B, due to the field-dependent yield stress,
- the fluid viscosity dependent component T_{vis} and
- the friction induced component $T_{fric.}$.

Thus, the overall brake torque:

$$T_{Overall} = T_B + T_{vis} + T_{fric} \quad (4)$$

The sum of the first two components T_B and T_{vis} i.e. the braking torque can be obtained by the following integral:

$$T_B + T_{vis} = 2\pi N \int_{R_i}^{R_O} \tau r^2 \mathrm{d}r\,, \quad (5)$$

where R_O and R_i are the brake's rotor outer and inner radii respectively. Considering practical conditions, for all MR brake types, the value of the R_i can be ignored because the R_O is several order of magnitude of the R_i *(Figure 2)*.

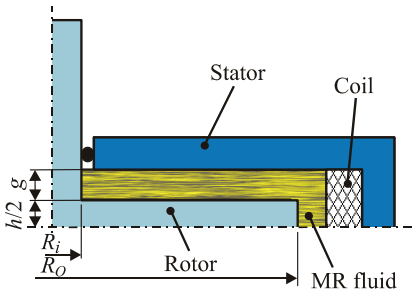

Figure 2: MR fluid disk brake simplified representation

Based on *Eq. (5)*, the authors formed the final analytical expressions for all five MR brake designs. Expressions were adopted from several different literature sources [1, 6, 12, 13, 21, 27, 29] and were partially altered in order to make the comparison easier. The last part of torque, T_{fric} can be precisely obtained only by torque gauge.

$$T_{Overall} = \pi\left(\frac{4}{3}\tau R_O^3 + \eta\frac{\omega}{g}R_O^4\right) + T_{fric}\,, \quad (6)$$

$$T_{Overall} = \pi N\left(\frac{4}{3}\tau R_O^3 + \eta\frac{\omega}{g}R_O^4\right) + T_{fric}\,, \quad (7)$$

$$T_{Overall} = 4\pi h\left(\tau R_O^2 + \eta\frac{\omega}{g}R_O^3\right) + T_{fric}\,, \quad (8)$$

$$T_{Overall} = 8\pi h\left(\tau R_O^2 + \eta\frac{\omega}{g}R_O^3\right) + T_{fric}\,. \quad (9)$$

Variable h is the height of the rotor.

It is now easy to distinguish components of overall braking torque in *Eq. (6–9)*, for disk, multiple disks, drums and T-shaped rotor, respectively. The yield stress τ_B given in *Eq. (2)*, varies with magnetic induction, but can reasonably be fitted with the third-order polynomial [12], as follows:

$$\tau_B = K_1 B + K_2 B^2 + K_3 B^3\,, \quad (10)$$

where K_i represents coefficients of regression.

Performances comparison

MR brakes can be compared on several different aspects e.g. overall braking torque, dynamic range, mechanical simplicity, inertia, electric power consumption, torque to volume ratio, compactness, etc. Authors of this paper compared level of mechanical simplicity for all five MR brake types and the overall braking torque based on analytical expressions, given in *Eq. (6–9)*, *Table 1*. In addition, the dynamic range and inertia were consider and presented in the same table.

Table 1: Characteristics of various MR brake designs

Brake type	$T_{Overall}$	Level of mechanical simplicity	Dynamic range T_B/T_{vis}	Inertia
(1)	M	H	$\frac{\tau_B}{\eta\dot{\gamma}}\cdot\frac{g}{R_i}$	$\frac{1}{2}mR_O^2$ *
(2)	M	L	$\frac{4}{3}\cdot\frac{\tau_B}{\eta\dot{\gamma}}\cdot\frac{g}{R_O}$	$\frac{1}{2}mR_O^2$
(3)	H	L	$\frac{4}{3}\cdot\frac{\tau_B}{\eta\dot{\gamma}}\cdot\frac{g}{R_O}$	$\frac{1}{2}mR_O^2 N_D$
(4)	H	H	$\frac{\tau_B}{\eta\dot{\gamma}}\cdot\frac{g}{R_O}$	$mR_O^2 - \frac{m_i R_i^2}{2}$

Explanations:
Brake types: (1)drum and inverted drum, (2) disk, (3) multiple disks, (4) T-shaped rotor.
Level of mech. simplicity: H – high, M - medium, L – low.
* For inverted drum brake design, expression is the same as for the T-shape rotor design.
N_D – the number of rotor disks, m_i – missing inner mass of the disk.

Dynamic range represents ratio of field induced component T_B and viscous component T_{vis} (friction torque component not considered).

T-shaped rotor brake performs best dynamic and can offer biggest overall braking torque, however it has a large inertia, and is considered difficult to manufacture. The other four designs are globally less compact than the T-shaped rotor design. The two drum based designs have comparable performances but are burdened with even larger inertia for same rotor radius. Finally, the disk and multiple disks designs offer a good alternative, being mechanically the simplest, with smaller inertia and giving reasonable dynamic range and the overall braking torque.

Test rig

Based on test rigs literature research [10, 15, 20, 27] and MR brake properties comparison *(Eq. (6–9)* and *Tab. 1)*,

the authors of this paper selected the most promising MR brake design and manufactured it. With lowest inertia, good dynamic range and the highest mechanical simplicity, the disk type promised the biggest potential.

For performance evaluating of the selected MR brake type a rig was set up. The test rig was designed and manufactured at Faculty of technical sciences, Novi Sad – Serbia, and is presently at its Laboratory for engines and vehicles. The test rig with its parts is depict in *Figure 3 and 4*, and consists of four main parts:

- drive,
- power supply,
- MR brake and
- measuring and data acquisition equipment.

An 8-pole AC squirrel cage motor with 0.75 kW and nominal speed of 700 rpm, model 5 AZ 100 LA – 8 (*Končar*) was placed at one end of the support-frame, of the test rig. The inverter - Micro Master (*Siemens*), *Fig. 4*, position 2, controls the direction and variable-speed of the AC motor. Speed range was from 150 rpm to 750 rpm with 50 rpm increment. These two elements form a drive part of the test rig. The flexible coupling connects AC motor and the shaft of the MR brake. MR brake rests on two self-aligning ball bearings into housings P203 (*FK Bearing group*). To avoid leakage of MR fluid, Nitrile Rubber lip seals, suitable for MR type application, have been used.

Torque transfer from the MR brake to a measurement device was done indirectly. A load arm, connected to the MR brake housing at one end, rests on top of the load cell on the other end, *Fig. 3*. Thus, by measuring the force on the load cell, the value of transmitted torque was obtained. Load cell was internally calibrated by calibration weights. The capacity of the load cell, 1030 (*Tedea*), was 15 kg.

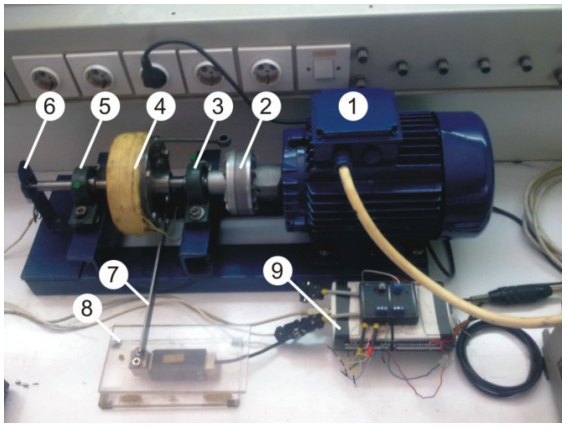

Figure 3: Demonstrating the test rig for MR brake 1. drive, 2. coupling, 3. self-aligning ball bearing, 4. MR fluid brake, 5. self-aligning ball bearing, 6. optical encoder, 7. load arm, 8. load cell, 9. data acquisition card

The optical encoder, model AMT102-V-REV-C (*CUI Inc.*), was connected to the shaft of the MR brake, at the opposite side of the AC motor and rotated at the same speed sample rate was 2048 per rotation. The signals were processed by universal amplifier, KWS 673.A2 (*HBM*), *Fig. 4*, position 3. The DC power supply, EA PS 2016-100 (*Elektro-automatik*), was connected to the leads of the coil to provide flux generation. This was the control current, with range of 0 A to 2 A and 0.2 A increment. The coil, made of copper wire with diameter of 1 mm (18 gauges) has been coiled on outer radius of the MR brake housing.

The MR fluid used in this experiment was Basonetic® 5030, from BASF® [17]. It is a carbonyl iron powder based MR fluid.

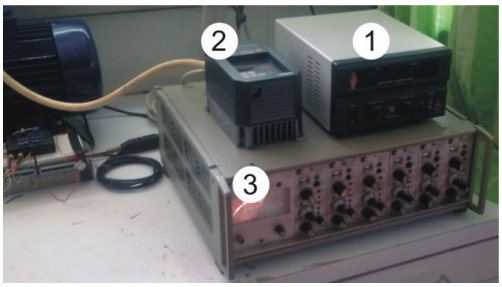

Figure 4: Measurement and data acquisition equipment: 1. stabilized power supply, 2. inverter, 3. universal amplifier

A typical testing procedure was as follows. First, the MR brakes shaft was set to a certain speed for 1 min as an initial condition, which stirred the MR fluid in the brake to distribute it uniformly. The desired magnetic field was then applied by setting the coil current i.e. control current and waiting for 1 min. This ensured stable structure forming of the MR fluid. The load cell detected transmitted torque. Finally, the signal from the load cell was processed and recorded.

Experimental results and improvement proposal

The goal of this experiment was to determine overall braking torque capabilities of selected MR brake design. The experiment was conducted on a specially designed test rig, with different control currents and speed sets. To eliminate the effects of previous observations, different combinations of control current and rotational speed were set for each reading. To bring repeatability in the reading, every speed set was carried out twice at different instance of time. For every reading, approximately 1 min time, before torque data recording, has been allotted to distribute the carbonyl iron particles uniformly in the MR fluid and form a stable structure.

Experimental results

The experiment itself consisted out of tree parts. The first part was to determine the influence of the supporting ball bearings and seals, without MR fluid inside the brake and no control current applied. This was a friction braking torque component. Second part of the experiment had the same setup but it included MR fluid inside the brake. Viscous torque data was then

recorded, assuming that bearings and seals did not change their friction characteristics in time.

Aforementioned recordings were needed in order to get clear and precise information about field induced component. This was the third part of the experiment and it included MR fluid inside the brake and application of the control current.

The same speed sets were used for the friction and the viscous torque component measurements were repeated. For each speed set, a 2 minute recording time was used. Some field induced component results are depict in *Figure 5*. Magnetic field influence is apparent.

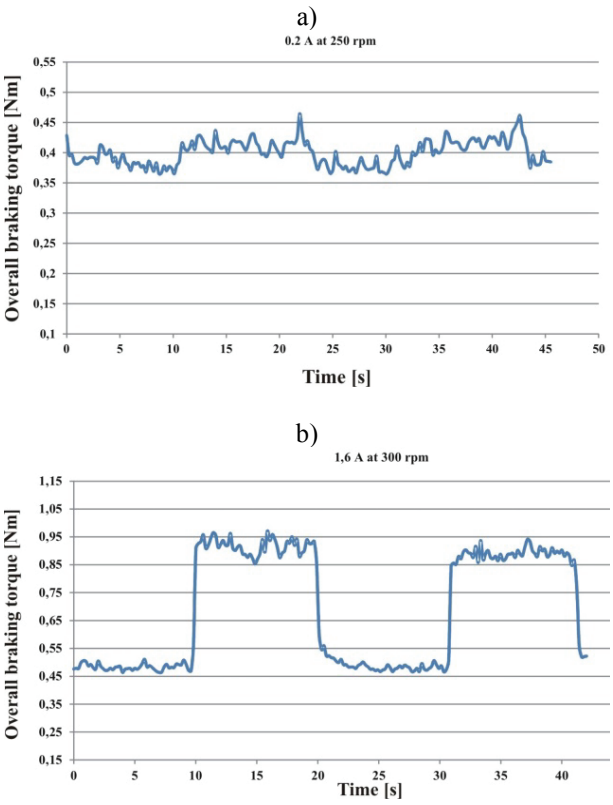

Figure 5: Samples of overall braking torque results: a) 0,2 A at 150 rpm, b) 1,6 A at 300 rpm

Because of the large number of data obtained in this experiment, authors decided to use amplification factor to determine the effect produced by magnetic field. Amplification factor (AF) represents relation between overall braking torque and sum of friction and viscous torque, i.e. relation between the ON and OFF state of the MR fluid.

$$AF = \frac{T_{Overall} \text{ at current } I}{T_{Overall} \text{ at zero current}} \qquad (11)$$

Amplification factor curves for all 13 speed sets are plotted in *Figure 6*. This figure shows linearity in amplification factor with increase in control current. This was expected, since the higher the current, the higher the field induced torque should be. Results are presented with rotational speed variation as well.

Figure 6 indicates that the amplification factors for speeds 150, 200, 250, 300 and 350 were much larger than the ones for 450, 500, 550, 600, 650, 700 and 750 rpm.

Transition rpm value for this MR brake was 400 rpm. This was somewhat opposite to the torque predicted by *Eq. (6)* where the $T_{Overall}$ should increase with angular speed. This was not the case here. However, other authors have also reported the same trend – reduction of amplification factor with increment of speed [20, 27]. This may be due to the possible shear thinning effect of the MR fluid at high shear rates. This reduces the effectiveness of MR brake at higher speeds. Therefore, to make MR brake effective at higher speed operation, one needs to think of „Shear stable MR fluid".

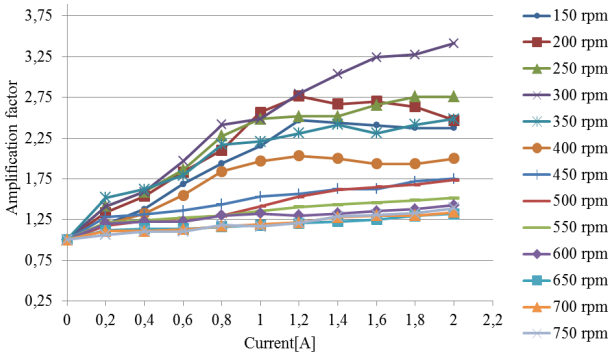

Figure 6: Variation in amplification factor with control current

MR brake improvement proposal

In order to increase the overall braking torque of any MR brake type its geometry needs to be optimized [14]. State of the art MR brake designs base their torque generation on the inner section of the coil [4, 10, 13]. These designs are rather inefficient, because the magnetic field is not used to its full potential and active MR area is small. Flux mostly travels through the housing of the MR brake. In this configuration, magnetic field is concentrated on small area of the MR fluid.

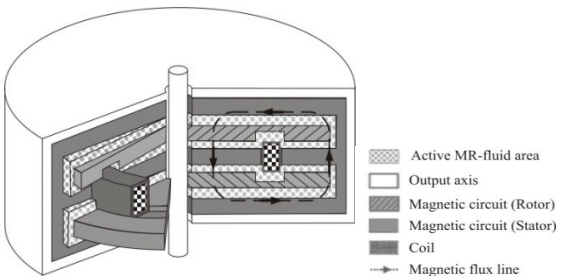

Figure 7: Novel MR brake design with enhanced magnetic field efficiency

By altering earlier MR brake designs, it is possible to concentrate magnetic field effect. One such design has been presented in *Figure 7*.

Compared to the dimensions of the tested MR disk brake, radius of the coil was reduced so that it could be placed in a more suitable position inside new MR brake design. New coil position allows for magnetic flux to be

used more efficiently. Now, the magnetic flux inside MR brake passes through MR fluid several times.

Based on analytical comparison, presented in *Eq. (6–9)* and *Tab. 1*, new design features two disks in order to create more MR fluid active area. Greater number of disks creates more MR fluid gaps thus the volume of MR fluid can be increased.

Conclusion

Authors compared all MR brake types on several different aspects. Based on this information, the most promising MR brake type was selected, manufactured and tested on a specially designed test rig.

The MR brake produced desirable results, which coincide with literature sources. Approximately linear relation between the overall braking torque and the control current intensity was observed. To present results in more readable manner, the amplification factor was introduced.

The experiment showed that the tested MR brake has potential for practical applications due to easiness and accuracy of control. However, the value of the overall braking torque is still small. To increase it, better utilization of the existing magnetic field is needed. The authors suggested different approach in comparison to the conventional MR brake design that would increase the overall braking torque by increasing the magnetic field efficiency and the contact area of the MR brake fluid. By multiplying the number of the disks in contact with MR fluid, value of the overall braking torque will multiply as well, *Eq. (7)*.

In order to maximize the potential of the proposed MR brake, further investigations on magnetic field propagation is needed as well as design optimization. Finite element method model of the novel MR brake is the next step in this process.

Acknowledgments

This research was done as a part of project TR31046 “Improvement of the quality of tractors and mobile systems with the aim of increasing competitiveness and preserving soil and environment”, supported by Serbian Ministry of Science and Technological Development.

MR fluid used in this experiment was provided by BASF® company, under commercial name Basonetic® 5030. The authors of this paper would like to express their sincere gratitude to BASF Company as well as to the project manager Dr. Christoffer Kieburg for all the supports.

REFERENCES

1. T. M. AVRAAM: MR-fluid brake design and its application to a portable muscular rehabilitation device, PhD thesis, Active Structures Laboratory, Department of Mechanical Engineering and Robotics, Universit´e Libre de Bruxelles, Bruxelles (2009)
2. G. BOSSIS, S. LACIS, A. MEUNIER, O. VOLKOVA: Magnetorheological fluids, Journal of magnetism and magnetic materials, 252 (2002), pp. 224–228
3. J. D. CARLSON, M. R. JOLLY: MR fluid, foam and elastomer devices, Mechatronics, 10 (2000), pp. 555–569
4. J. D. CARLSON, D. M. CATANZARITE, K. A. CLAIR: Commercial magnetorheological fluid devices, In Proceedings of the 5th International Conference on ER Fluids, MR Suspensions and Associated Technology (Ed. W. A. Bullogh), Singapore (1996), pp. 20–28
5. E. D. ERICKSEN, F. GORDANINEJAD: A magneto-rheological fluid shock absorber for an off-road motorcycle, International J. Vehicle Design, 33 No 1-3 (2003), pp. 139–152
6. A. FARJOUD, N. VAHDATI, Y. F. FAH: Mathematical model of drum-type MR brake using Hershel-Bulkley shear model, Journal of Intelligent Material Systems and Structures (2007), pp. 1–8
7. D. G. FERNANDO: Characterizing the behavior of magnetorheological fluids at high velocities and high shear rates, PhD thesis, Faculty of the Virginia Polytechnic Institute and state University, Blacksburg,Virginia (2005)
8. F. D. GONCALVES, J. D. CARLSON: An alternate operation mode for MR fluids – Magnetic Gradient Pinch, Journal of Physics: Conference Series, 149 (2009), pp. 1–4
9. K. H. GUDNUNDSSON, F. JONSDOTTIR, F. THORSTEINSSON: A geometrical optimization of a magneto-rheological rotary brake in a prosthetic knee, Smart Materials and Structures, 19 (2010) pp. 1–11
10. Z. HEROLD, D. LIBL, J. DEUR: Design and testing of an experimental magnetorheological fluid clutch, Strojarstvo, 52 No. 3 (2010), pp. 601–614
11. J. HUANG, J. Q. YHANG, Y. YANG, Y. Q. WEI: Analysis and design of a cylindrical magneto-rheological fluid brake, Journal of Material Processing Technology, 129 (2002) pp. 559–562
12. A. JINUNG, K. DONG-SOO: Modelling of mag-netorheological actuator including magnetic hysteresis, Journal of Intelligent Material Systems and Structures, 14 (2003) pp. 541–550
13. K. KARAKOC, J. E. PARK, A. SULEMAN: Design considerations for an automotive magnetorheo-logical brake, Mechatronics, 18, No. 8 (2008), pp. 434–447
14. K. KARAKOC: Design of a Magnetorheological Brake System Based on Magnetic Circuit Optimization, PhD Thesis, Department of Mechanical Engineering, University of Victoria, Victoria, Canada (2007)
15. B. M. KAVLICOGLU, F. GORDANINEJAD, C. A. EVRENSEL, N. COBANOGLU, Y. LUI, A. FUCHS, G. KOROL: A high-torque magneto-rheological fluid clutch, Proceedings of SPIE Conference on smart

materials and structures, March 2002, San Diego, pp. 1–8

16. K. KAYLER: Lord corporation expands production of steer-by-wire TFD brakes to meet demand, available from: http://www.lord.com/news-center/press-releases/lord-corporation-expands-production-of-steer-by-wire-tfd-brakes-to-meet-demand-.xml. (Accessed on 6. 20. 2013.)
17. C. KIEBURG: MR-fluid Basonetic 5030, Technical Information, BASF SE Metall Systems, Ludwingshafen, Germany (2010)
18. U. LANGE, L. RICHTER, L. ZIPSER: Flow of magnetorheological fluids, Journal of Intelligent Material Systems and Structures, 12 (2001), pp. 161–164
19. D. LAMPE, R. GRUNDMANN: Transitional and solid state behaviour of a magnetorheological clutch. In Proceedings of Actuator 2000, Bremen (2000)
20. W. H. LI, H. DU: Design and experimental evaluation of a magnetorheological brake, The International Journal of Advanced Manufacturing Technology, 21 (2003), pp. 508–515
21. B. LIU, W. H. LI, P.B. KOSASIH, X. Z. ZHANG: Development of an MR-brake-based haptic device, Smart Materials and Structures, 15 (2003), pp. 1960–1966
22. Q. N. NGUYEN, S. B. CHOI: Selection of magnetorheological brake types via optimal design considering maximum torque and constrained volume, Smart Materials and Structures, 21 (2012), pp. 1–12
23. E. J. PARK, D. STOIKOV, L. F. DA LUZ, A. SULEMAN: A performance evaluation of an automotive magnetorheological brake design with a sliding mode controller, Mechatronics, 16 (2006), pp. 405–416
24. N. PHUONG-BAC, C. SEUNG-BOK: A new approach to magnetic circuit analysis and its application to the optimal design of a bi-directional magnetorheological brake, Smart Materials and Structures, 20 (2011), pp. 1–12
25. J. RABINOW: Magnetic fluid torque and force transmitting device, US patent 2,575,360, 1951.
26. B. F. SPENCER, S. J. DYKE, M. K. SAIN, J. D. CARLSON: Phenomenological model of a magnetorheological damper, ASCE Journal of Engineering Mechanics, 123, No. 3 (1996), pp. 1–23
27. V. K. SUKHWANI, H. HIRANI: Design, development, and performance evaluation of high-speed magnetorheological brakes, Proceedings of the Institution of Mechanical Engineers, Part L: Journal of Materials Design and Applications, 222 (2008), pp. 73–82
28. J. WANG, G. MENG: Magnetorheological fluid devices: principles, characteristics and applications in mechanical engineering, Proceedings of Institution of Mechanical Engineers – Part L – Journal of Materials: Design and Application, 215 (2001), pp. 165-174
29. Z. A. ZAINORDIN, A. M. ABDULLAH, K. HUDHA: Experimental evaluations on braking responses of magnetorheological brake, International journal of mining, metallurgy & mechanical engineering, 1, No. 3 (2013), pp. 195–199